Colloidal Hard Sphere Crystals and their Interfaces in Density Functional Theory

Dissertation
der Mathematisch–Naturwissenschaftlichen Fakultät
der Eberhard Karls Universität Tübingen
zur Erlangung des Grades eines
Doktors der Naturwissenschaften
(Dr. rer. nat.)

vorgelegt von
Mohammad Hossein Yamani
aus Zanjan/Iran

Tübingen
2014

Tag der mündlichen Qualifikation:	15.07.2014
Dekan:	Prof. Dr. Wolfgang Rosenstiel
1. Berichterstatter:	Prof. Dr. Martin Oettel
2. Berichterstatter:	Prof. Dr. Roland Roth

Abstract

The research reported in this thesis addresses necessary equilibrium information for understanding of homogeneous and heterogeneous nucleation in the hard sphere system. Colloidal hard spheres are an intensely studied model system for addressing the nucleation problem. Understanding nucleation requires a precise knowledge about equilibrium crystal structures and free energies. We use classical density functional theory (DFT) of fundamental measure type (FMT) to evaluate the fully minimized crystal density profiles and their interfaces. Results are compared with simulation data and complemented by a cluster expansion approach due to Stillinger which is based on expanding the crystal partition function in terms of the number n of free particles while the remaining particles are pinned at their ideal lattice positions. Finally, dynamical density functional theory (DDFT) as a time dependent extension of static DFT is implemented.

Face–centered cubic (fcc), hexagonally close–packed (hcp) and body–centered cubic (bcc) crystals are investigated using fundamental measure theory and results are complemented by results from Stillinger's approach. Two branches of solutions have been observed for bcc structure corresponding to different width parameters of the density distribution around lattice sites. The free energy of one branch of bcc agrees well with FMT and Stillinger's approximation truncated at $n = 2$. A second branch of the bcc solution features rather spread–out density distributions around lattice sites and a large equilibrium vacancy concentration and it is presumably linked to the shear instability of the bcc phase. Within fundamental measure theory and Stillinger approach ($n = 2$), hcp is more stable than fcc by a free energy per particle of about $10^{-3}k_BT$. In previous simulation work, the reverse situation has been found which can be rationalized in terms of an effect due to correlated motion of at least 5 particles in the Stillinger picture.

At a hard, flat and unstructured substrate, the crystalline phase completely wets the substrate when the fluid density approaches the freezing point. The formed crystal is oriented with close–packed planes parallel to the substrate. Heterogeneous nucleation for the hard sphere fluid at unstructured hard walls has not been found neither in simulation methods nor in DFT approaches. In collaboration with a simulation group, the

hard sphere fluid confined between parallel soft plated is studied in search of a variable nonzero contact angle which could allow studying heterogeneous nucleation. The Week–Chandler–Andersen (WCA) potential is used as a wall potential with variable wall strength. Two variants of FMT are implemented to evaluate the density distributions and surface tensions of the hard sphere fluid at the wall with different strengths. DFT is found to be quantitatively very accurate over a wide range of packing fraction in comparison with Monte Carlo simulation. For the surface tension, only small deviations between DFT and MC near the fluid–crystal transition are observed.

Finally, dynamical density functional theory (DDFT) is implemented for equilibrating the fcc hard sphere crystal and the crystal–liquid interface density profile. DDFT results for fcc are in an excellent agreement with DFT and simulation data. For the crystal–liquid interface tension there is about 4% discrepancy between DDFT and direct minimizations of DFT. This difference is due to the stiffness of the DDFT equation which does not allow us to fully equilibrate the interface density profile.

Zusammenfassung

Diese Arbeit addressiert Informationen über das thermische Gleichgewicht in Hartkugelsystemen, die für das Verständnis von homogener und heterogener Keimbildung notwendig sind. Kolloidale harte Kugeln sind ein oft untersuchtes Modellsystem für die Frage der Keimbildung. Das Verständnis der Keimbildung erfordert präzises Wissen der Kristallstrukturen im Gleichgewicht und deren freie Energien. In dieser Arbeit wird klassische Dichtefunktionaltheorie (DFT) in der Form der Fundamentalmaßtheorie (FMT) benutzt, um Dichteprofile im Kristall und an der Grenzfläche durch volle Minimierung zu bestimmen. Die erhaltenen Resultate werden mit Simulationsdaten verglichen und mit Resultaten aus einem Clusterentwicklungszugang nach Stillinger ergänzt. Dieser basiert auf einer Entwicklung der Zustandssumme des Kristalls in der Zahl n von freien Teilchen, während die anderen Teilchen an ihren idealen Gitterpositionen fixiert bleiben. Abschließend wird eine Implementierung von dynamischer Dichtefunktionaltheorie als eine zeitabhängige Erweiterung von DFT diskutiert.

Kubisch–flächenzentrierte (fcc), hexagonal–dichtgepackte (hcp) und kubisch–raumzentrierte (bcc) Kristalle werden mit FMT untersucht und mit Resultaten aus Stillingers Zugang ergänzt. Für bcc wurden zwei Lösungszweige gefunden mit entsprechend unterschiedlichen Breiten der Dichteverteilung um einen Gitterplatz. Die freie Energie eines Zweigs stimmt gut mit dem Resultat aus dem Stillinger–Zugang für $n = 2$ überein. Der zweite Lösungszweig zeigt eine verhältnismäßig breite Dichteverteilung um einen Gitterplatz, eine relativ große Leerstellendichte und hat vermutlich eine enge Beziehung mit der bekannten Scherinstabilität der bcc–Phase. Weiterhin ist in FMT und dem Stillinger–Zugang ($n = 2$) hcp stabiler als fcc um eine freie Energie pro Teilchen von etwa $10^{-3} k_B T$. In Simulationen wurde die umgekehrte Situation gefunden, dies kann innerhalb des Stillinger–Zugangs mit der korrellierten Bewegung von mindestens 5 Teilchen erklärt werden.

Für Anlagerung an einem harten, flachen und unstrukturierten Substrat ist bekannt, dass die kristalline Phase das Substrat vollständig benetzt, wenn die Dichte der Flüssigkeit der Koexistenzdichte zustrebt. Heterogene Keimbildung im Hartkugel–Fluid an glatten

harten Wänden wurde weder in Simulationen oder DFT–Studien gefunden. In Zusammenarbeit mit einer Simulationsgruppe wurde das Hartkugel–Fluid zwischen parallelen weichen Wänden in Hinsicht auf einen von Null verschiedenen Kontaktwinkel untersucht. Dieser würde die Untersuchung von heterogener Keimbildung zulassen. Hierbei wurde das Weeks–Chandler–Anderson–(WCA–)Potential mit variabler Stärke benutzt. Dichteverteilungen an den Wänden und Grenzflächenspannungen wurden mit zwei verschiedenen FMT–Funktionalen berechnet. Die DFT–Resultate stimmen quantitativ sehr gut mit Monte–Carlo–Resultaten in einem großen Dichtebereich überein. Für die Oberflächenspannung wurden nur kleine Abweichungen in der Nähe des Flüssig–Kristall–Übergangs gefunden.

Abschießend wird eine Implementierung von DDFT für die Equilibrierung von fcc–Kristall– und Grenzflächendichteprofilen diskutiert. Die DDFT–Resultate für fcc stimmen gut mit denen aus DFT und Simulationen gewonnenen überein. Für die Grenzflächenspannung ist eine eta vierprozentige Differenz zwischen DDFT und direkter Minimierung von DFT zu sehen. Diese Differenz ist eine Folge der Steifheit der DDFT–Gleichung, die es nicht erlaubte, das Grenzflächenprofil vollständig zu equilibrieren.

List of Publications

I started my PhD at the *Institute of Physics: Condensed Matter Theory Group* at *Johannes Gutenberg–Universität Mainz* in April 2010 and graduated from the *Institute of Applied Physics, Eberhard Karls Universität Tübingen* in July 2014. During this period, most of my work has been published in academic journals in collaboration with other scientists. The resulting publications are listed in the following. The major results in this thesis have already been published.

Solid phase properties and crystallization in simple model systems
F. Turci, T. Schilling, M. H. Yamani and M. Oettel, Eur. Phys. J. Special Topics **223**, 421 (2014).

Abstract: We review theoretical and simulational approaches to the description of equilibrium bulk crystal and interface properties as well as to the nonequilibrium processes of homogeneous and heterogeneous crystal nucleation for the simple model systems of hard spheres and Lennard–Jones particles. For the equilibrium properties of bulk and interfaces, density functional theories employing fundamental measure functionals prove to be a precise and versatile tool, as exemplified with a closer analysis of the hard sphere crystal–liquid interface. A detailed understanding of the dynamic process of nucleation in these model systems nevertheless still relies on simulational approaches. We review bulk nucleation and nucleation at structured walls and examine in closer detail the influence of walls with variable strength on nucleation in the Lennard–Jones fluid. We find that a planar crystalline substrate induces the growth of a crystalline film for a large range of lattice spacings and interaction potentials. Only a strongly incommensurate substrate and a very weakly attractive substrate potential lead to crystal growth with a nonzero contact angle.

Statement of the author: This work is a review which uses theoretical and simulational approaches to study the hard–sphere system in equilibrium and out of equilibrium. Density functional theory has performed by M. Oettel and simulation data were obtained by F. Turci and T. Schilling. My personal contribution to this article is essentially calculating the Turnbull coefficients of fcc and bcc crystals. Besides, this article reviews my results about the description of the metastability of bcc and hcp using comparison of the free energy between these metastable structures and the stable fcc crystal.

Stable and metastable hard sphere crystals in Fundamental Measure Theory
M. H. Yamani and M. Oettel, Phys. Rev. E **88**, 022301 (2013).

Abstract: Using fully minimized fundamental measure functionals, we investigate free energies, vacancy concentrations and density distributions for bcc, fcc and hcp hard–sphere crystals. Results are complemented by an approach due to Stillinger which is based on expanding the crystal partition function in terms of the number n of free particles while the remaining particles are frozen at their ideal lattice positions. The free energies of fcc/hcp and one branch of bcc agree well with Stillinger's approach truncated at $n = 2$. A second branch of bcc solutions features rather spread–out density distributions around lattice sites and large equilibrium vacancy concentrations and is presumably linked to the shear instability of the bcc phase. Within fundamental measure theory and the Stillinger approach ($n = 2$), hcp is more stable than fcc by a free energy per particle of about 0.001 $k_{\mathrm{B}}T$. In previous simulation work, the reverse situation has been found which can be rationalized in terms of effects due to a correlated motion of at least 5 particles in the Stillinger picture.

Statement of the author: This work is a combined study using density functional theory and Stillinger's approach. The motivation came from the question why fcc is more stable than hcp in the hard–sphere system and for the completeness of the study, the bcc structure was investigated as well. All the DFT calculations have been performed by myself. DFT results were complemented by Stillinger's approach which has been implement by M. Oettel. I have almost written half of the article and generated all the figures but Fig. 6.

Hard sphere fluids at a soft repulsive wall: A comparative study using Monte Carlo and density functional methods

D. Deb, A. Winkler, M. H. Yamani, M. Oettel, P. Virnau and K. Binder, J. Chem. Phys. **134**, 214706 (2011).

Abstract: Hard-sphere fluids confined between parallel plates at a distance D apart are studied for a wide range of packing fractions including also the onset of crystallization, applying Monte Carlo simulation techniques and density functional theory. The walls repel the hard spheres (of diameter σ) with a Weeks–Chandler–Andersen (WCA) potential $V_{WCA}(z) = 4\epsilon[(\sigma_w/z)^{12} - (\sigma_w/z)^6 + 1/4]$, with range $\sigma_w = \sigma/2$. We vary the strength ϵ over a wide range and the case of simple hard walls is also treated for comparison. By the variation of ϵ one can change both the surface excess packing fraction and the wall–fluid γ_{wf} and wall–crystal γ_{wc} surface free energies. Several different methods to extract γ_{wf} and γ_{wc} from Monte Carlo (MC) simulations are implemented, and their accuracy and efficiency is comparatively discussed. The density functional theory (DFT) using fundamental measure functionals is found to be quantitatively accurate over a wide range of packing fractions; small deviations between DFT and MC near the fluid to crystal transition need to be studied further. Our results on density profiles near soft walls could be useful to interpret corresponding experiments with suitable colloidal dispersions.

Statement of the author: This work is a comparative study using Monte Carlo simulation and density functional theory. The idea originated from the simulation group who was interested to search for a variable nonzero contact angle which could allow studying heterogeneous nucleation. All the DFT calculations have been performed by myself. Simulation data were generated by D. Deb and A. Winkler and the comparison between the MC simulation data and the DFT results were done by other co–authors.

Contents

List of Figures

List of Tables

Abbreviations

BCC	**B**ody–**C**entered **C**ubic
CF	**C**omplex **F**luid
DDFT	**D**ynamical **D**ensity **F**unctional **T**heory
DF	**D**ensity **F**unctional
DFT	**D**ensity **F**unctional **T**heory
DIIS	**D**irect **I**nversion in **I**terative **S**ubspace
EOS	**E**quation **O**f **S**tate
FCC	**F**ace–**C**entered **C**ubic
FMT	**F**undamental **M**easure **T**heory
HC	**H**ard **C**ore
HCP	**H**exagonal **C**lose–**P**acked
HD	**H**ard **D**isk
HR	**H**ard **R**od
HS	**H**ard **S**phere
HW	**H**ard **W**all
LDA	**L**ocal **D**ensity **A**pproximation
MC	**M**onte **C**arlo
MFA	**M**ean **F**ield **A**pproximation
ODE	**O**rdinary **D**ifferential **E**quation
OZ	**O**rnstein–**Z**ernike
PFC	**P**hase **F**ield **C**rystal
RLV	**R**eciprocal **L**attice **V**ector
SCF	**S**elf–**C**onsistent **F**ield
SOC	**S**ingle **O**ccupancy **C**ell
SPT	**S**caled **P**article **T**heory

WB **W**hite **B**ear

WCA **W**eeks–**C**handler–**A**ndersen

WDA **W**eighted **D**ensity **A**pproximation

YBG **Y**von–**B**orn–**G**reen

Symbols

$c^{(n)}$	direct correlation function
F	Helmholtz free energy
f_0	equilibrium probability density function
$\mathcal{F}$	free energy functional
G	Gibbs free energy
$g^{(n)}$	n–particle distribution function
H	enthalpy
ΔH_m	melting latent heat
$h(r)$	total correlation function
$\mathcal{H}$	Hamiltonian
K_N	kinetic energy
$\mathbf{k}$	reciprocal lattice vector
n_{vac}	vacancy concentration
n_α	weighted density
P, p	pressure
$P(\mathbf{k})$	form factor
Q	canonical partition function
R	hard sphere radius
S	entropy
$S(\mathbf{k})$	structure factor
T	temperature
V	volume
V_N	interatomic potential
V_{ext}	external potential
Z_N	configuration integral

z	activity
Γ	number of microstates / mobility
η	packing fraction
γ	surface tension
Λ	De Broglie wavelength
μ	chemical potential
Ξ	grand canonical partition function
ρ	density / one–particle density
$\rho^{(n)}$	n–particle density
$\hat{\rho}$	density operator
σ	hard sphere diameter
Φ	free energy density function
Ω	grand potential energy
ω	phase space volume
$\omega^{\alpha}(\tilde{\omega}^{\alpha})$	FMT weight function (Fourier transformed weight function)
ω_{WDA}	WDA weight function

Chapter 1

Introduction

Crystallization touches every aspect of our lives from the foods we eat and the medicines we take, to the solar cells which are used to produce electricity. The majority of pharmaceutical products go through at least one crystallization step during their manufacture [1]. It is also a central topic of tremendous importance in industry ranging from semiconductors, piezo sensors, ferroelectric memories, optical elements to nano–structures, quantum dots and organic systems [2].

Scientists and engineers working in many industries around the world are required to understand, optimize and control crystallization processes every day. The prevalence of crystallization processes in industry can probably be attributed to the fact that crystallization acts as both a separation and purification step. In one fell swoop, crystal product of the desired purity can be created and then isolated. Despite this obvious advantage, crystallization processes still need to be understood and controlled to ensure that the desired crystal product quality is achieved and to ensure an efficient and cost-effective crystallization process.

The starting point for most crystallization processes is a saturated solution. Crystallization is generally achieved by reducing the solubility of the product in this solution by cooling, antisolvent addition, evaporation or some combination of these methods. Another common method used to drive crystallization is via a chemical reaction where two or more reactants are mixed to form a solid product insoluble in the reaction mixture. The method chosen can vary depending on a number of factors.

Having recognized the existence of atoms and molecules, it seems natural to use a system of hard bodies perturbed by intermolecular potentials for the modeling of the thermodynamic properties of fluids. In crystallization molecules or particles form an ordered structure. It is a formidable problem in statistical mechanics and quantum chemistry to predict the stable crystal structure and its free energy for a given substance. Approximating the particle interactions in this substance by classical two–body potentials makes the problem amenable to a treatment using methods of classical statistical mechanics, most notably Monte Carlo (MC) simulations and (classical) density functional theory (DFT). While the approximation using two–body potentials may not be very accurate for truly atomic substances, the advance in colloid synthesis allows to realize systems with simple two–body potentials to a good degree of approximation, thus hard colloidal suspensions are a perfect model system for investigating crystallization in classical statistical mechanics.

Hard spheres (HS) are a paradigmatic system. Despite the simplicity of that system, and that it only exists in computers, it has served as the basis for the advance of science in the fields of general liquids, amorphous solids, liquid crystals, colloids, granular matter, etc. HS systems exhibit a surprisingly rich structural and thermodynamic behavior (phase transitions, metastable states, demixing, etc.) that call for careful study. Also surprisingly, this behavior is not completely understood and is an object of current research. The hard sphere system is not temperature–dependent and the only control parameter for crystallization is density. The interest for the study of these systems is due to the fact that the structure of real fluids is mainly determined by repulsive forces and it is commonly used as a reference system for perturbation approach.

Understanding the crystallization requires a precise knowledge about crystal structures, free energies and interfacial properties. Density functional theory (DFT) is one of the core theoretical approaches in statistical physics. DFT was developed by P.Hohenberg and W. Kohn [3] in the context of quantum chemistry and led to the 1998 Nobel prize in chemistry. Later on, it has been generalized to finite temperature [4] and classical systems [5, 6]. The density functional theory for classical particles was developed to find out the equilibrium density distribution of inhomogeneous systems at interfaces or in the presence of an external potential. The applicability of DFT is related to its functional approximation. Over the last decades, there has been an impressive improvement in the quality of functionals with the development of fundamental measure theory (FMT)

in the 1990s as a milestone. Dynamic density functional theory (DDFT) is a time dependent (dynamic) extension of the static DFT is able to describe the time evolution of the density of Brownian particles.

In this thesis, first an introduction to the phase transition and statistical mechanics is given in Chapter 2. In Chapter 3, density functional theory as the main theoretical approach of this thesis is introduced and different functional approximations as well as the FMT as the most natural approximate scheme are presented. Besides, Stillinger's approach which approximates the crystal free energy by an expansion of the crystal partition function in terms of the number n of correlated, contiguous particles which are free to move and dynamical density functional theory are recapitulated. The hard sphere crystals are studied in detail in Chapter 4 in the framework of density functional theory of FMT and results are complemented by the Stillinger's approach. The main goal of this chapter is to study the stability of the hard sphere crystals. Chapter 5 deals with the hard sphere fluid confined between two parallel soft walls. Density distribution and interfacial properties are obtained by DFT and results are compared to Monte Carlo simulation data. The motivation of this study besides the test of the accuracy of FMT functionals was to test whether a variable contact angle can be obtained for hard spheres at repulsive walls. The nonzero contact angle would allow studying the heterogeneous nucleation. Finally, in Chapter 6 dynamical density functional theory (DDFT) is used to investigate the equilibrium structures of the fcc crystal and crystal–liquid interface.

Chapter 2

Phase Transitions and Statistical Mechanics

Condensed matter is held together by intermolecular forces, the strength and range of these forces determine the bulk, macroscopic properties of matter. The basic aim of the condensed matter physics is to understand the collective properties of large assemblies of particles in terms of the interactions between their component parts. This chapter concerns with the phase transition of soft matter systems (Section 2.1) and the tools we will need are those of statistical mechanics (Section 2.2).

2.1 Phase Transitions in Soft Matter

2.1.1 Condensation and Freezing

The most obvious manifestation of the forces between molecules is in the fact that on cooling a collection of molecules, its physical state changes from a gas or vapor to a liquid and on further cooling there is another change of state from a liquid to a solid. The attractive forces between molecules are weak at high temperatures in comparison with the thermal energy; this thermal energy is present almost entirely in the form of kinetic energy. The molecules in the gaseous state are moving with a very little correlation between the positions of different molecules. In this state molecules are in a state of constant motions and interacting with each other only relatively infrequently through

occasional collisions. This is the state that approximates the *ideal* or *perfect* gas. By reducing the temperature, attractive interactions between the molecules start to become more important. On colliding, pairs of molecules stay together longer and longer and correlation between the motion of different molecules starts to appear, with short–lived clusters of molecules forming and breaking up. While the energy of the molecules is still dominated by the kinetic energy in this state, the properties of the gas start to deviate from the ideal gas and at some point the correlation between molecules leads to a new dense phase of the liquid. In the liquid state the attractive energy between molecules is as important a part of total energy as the kinetic energy of the motion. The repulsive part of the interaction energy between the molecules also plays a role; the fact that two molecules cannot be in the same place at once leads to short–ranged correlations in the position of the molecules. The structure of the liquid is determined by the tension between the attractive part of the intermolecular potential, which tries to pack molecules as closely as possible, and the repulsive part of the potential which imposes a minimum separation between molecules. As the temperature is decreased further, another way of resolving this tension manifests itself. By packing the molecules together in regular rather than random way, it is possible to achieve a higher density of molecules, while still satisfying the minimum distance constraint imposed by the repulsive part of the potential. The liquid has frozen. The condition under which solids, liquids, and gases form and coexist are summarized in a *phase diagram*. For a simple liquid, this plots the relationship between temperature, pressure and volume (or equivalently, density). Figure 2.1(a) shows a typical phase diagram of simple molecular material in which the regimes of temperature and pressure in which various phases are stable are plotted. Figure 2.1(b) shows the same information with emphasizing the idea of coexistence; at a given pressure, there is a temperature at which two out of the three phases will coexist [7].

2.1.2 Phase Transitions

Soft matter often has a very rich and complicated morphology and its components can be arranged in a complicated way, involving features at length scales intermediate between the atomic and the macroscopic. The remarkable feature of these structures is that they are self–assembled. It means they put themselves together in a very complicated arrangements without outside assistance. There are two general classes of

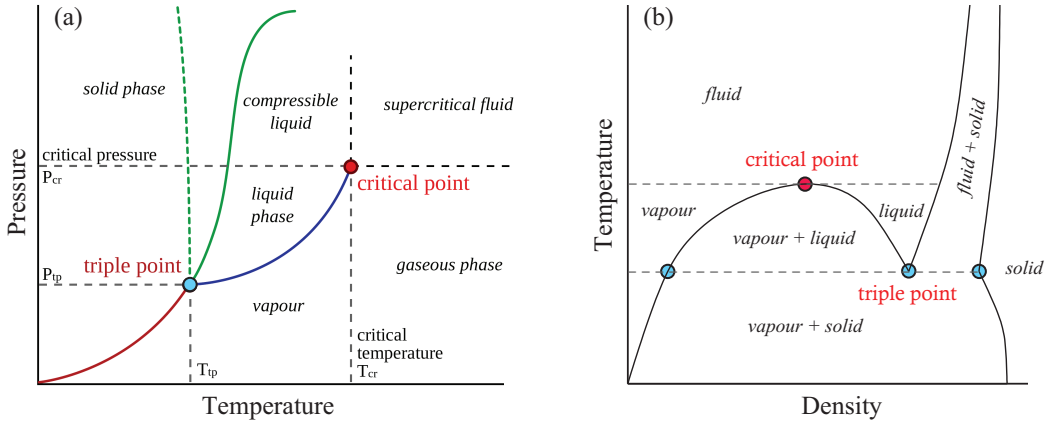

FIGURE 2.1: Schematic phase diagram for a simple elemental or molecular materials. The familiar projection as a function of pressure and temperature is shown in (a)[8], while (b) shows the same information plotted as density as a function of temperature. In triple point all three phases coexist and above the critical point the liquid and the gas merge into a single fluid phase.

self–assembled structure, equilibrium and non–equilibrium structures. Non–equilibrium self–assembled structures often occur following a phase transition. If some external parameters (e.g. temperature) is changed, the structure with the lowest energy may discontinuously change its character. Thus a qualitative change of structure occurs in response to a quantitative change in a control parameter. The balance between entropy and energy is reflected in the free energy; for example, for changes at constant volume the appropriate free energy is the Helmholtz free energy F, defined by $F = U - TS$, where U is internal energy ans S is entropy. For a phase transition one can define an order parameter, which typically takes a zero value in the disordered phase and a finite value in the ordered phase. The way the order parameter varies with temperature tells one about the nature of the transitions. In first–order phase transitions, the order parameter changes discontinuously at the phase transition (e.g. melting of a crystal), and in second–order transitions the order parameter is continuous (e.g. change from a liquid to a gas at a critical point).

Information about which equilibrium phases have the lowest free energy is not sufficient by itself to explain all types of the structures one can obtain in soft matter. In addition, one needs to understand the kinetics of the process by which phase ordering or disordering proceeds.

2.1.2.1 Liquid–Liquid Demixing

The first example of a phase transition describes the situation when two liquids are miscible in all proportions at high temperature, but separate into two distinct phases when the temperature is lowered. In order to understand the phase separation, we need to calculate the free energy of mixing, F_{mix}. If we can predict this quantity as a function of composition and temperature we have everything we need to know about the phase behavior of the system. We are also able to calculate the free energy of the phase–separated system according to the relative composition.

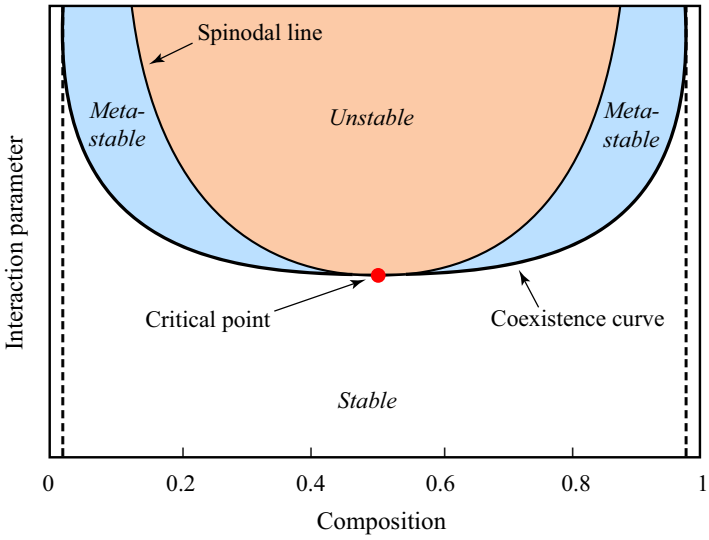

FIGURE 2.2: The phase diagram of a liquid mixture. Interaction parameter characterizes the strength of the energetic interaction between two phases relative to their self interactions and the horizontal axis denote the the volume fraction of one species of the mixture.

Figure 2.2 shows the phase diagram of liquid–liquid mixture. In the unstable part of the phase diagram, phase separation takes place by a continuous change in composition. In this process, the concentration fluctuations that are present in any mixtures at thermal equilibrium are amplified. This process is known as spinodal decompositions. In contrast, when a mixture is in the metastable region of the phase diagram, it is not possible for the mixture to phase–separate by a process in which the composition in a region changes continuously; in a pure mixture a relatively large composition fluctuation must take place, with a corresponding high energy cost. This relatively large nucleus can grow in size [7]. This process is known as homogeneous nucleation. In a real system, it is

usually found that some impurity particles are present on which the new phase may be nucleated with lower activation energy that for homogeneous nucleation. This is known as heterogeneous nucleation.

2.1.2.2 The Liquid–Solid Transition: Freezing and Melting

The transition between liquid and solid is important both for normal and soft matter. When a liquid freezes it goes from a state with short–range order to a state with long–range order. Associated with this long–range order is the rigidity that we associate with a solid. The liquid–solid phase transition is a first–order phase transition; this means that at the transition the order parameter changes discontinuously and the thermodynamic quantities that are derivatives of a free energy with respect to other thermodynamic variables are discontinuous at the transition.

Before studying the thermodynamic behavior of the phase transition it is worth to recapitulate some thermodynamic quantities. Enthalpy is the preferred expression of system energy changes in many chemical, biological, and physical measurements at constant pressure through expansion or heating and it reads

$$H = U + PV. \tag{2.1}$$

The enthalpy change of a system, ΔH, is equal to the sum of non–mechanical work done on it and the heat supplied to it. In phase transition process, the pressure is constant, therefore ΔH is equal to the change in the internal energy of the system, plus the work that the system has done on its surroundings [9]. This means that the change in enthalpy under such conditions is the heat absorbed (or released) by the system through a chemical reaction or by external heat transfer. This change in the enthalpy during a constant–temperature process like melting and freezing transition is known as the latent heat ΔH_m [10, 11]. On the other hand, the Gibbs free energy[1] G is the appropriate thermodynamic potential for constant temperature and pressure which is defined as

$$G = H - TS, \tag{2.2}$$

[1] Also known as free enthalpy [12]

or equivalently

$$G = F + PV, \tag{2.3}$$

where $F = U - TS$ is the Helmholtz free energy. At melting transitions the change in Gibbs free energy is zero

$$\Delta G_m = 0 \quad \longrightarrow \quad \Delta F = -P\Delta V, \tag{2.4}$$

thus the change in enthalpy is given by

$$\begin{aligned} \Delta H_m &= \Delta U + P\Delta V \\ &= \Delta F + T_m \Delta S + P\Delta V. \end{aligned} \tag{2.5}$$

Using Equations (2.4) and (2.5) it is obvious that at the melting temperature a latent heat ΔH_m released is related to the change in the entropy of melting ΔS_m by

$$\Delta S_m = \frac{\Delta H_m}{T_m}. \tag{2.6}$$

Using Figure 2.3 one can argue that a liquid in its melting point, if it is free from impurities and in a large enough container to be unaffected by the walls, will never freeze, because creation of a crystal costs free energy due to the interfacial energy γ_{sl} between solid and liquid. But the change in Gibbs free energy going from liquid to solid is zero exactly at the melting point. Therefore in order to initiate freezing in the absence of impurities, one must undercool a liquid below its melting temperature. Freezing is then initiated by an active process of nucleation.

- **Homogeneous Nucleation**

  The process of crystallization is initiated by the spontaneous appearance of a crystal nucleus. We assume the nucleus to be spherical with radius r. The change in the Gibbs free energy $\Delta G(r)$ due to the formation of nucleus is the sum of a term proportional to the surface area of the crystal with solid–liquid interfacial energy γ_{sl} and a term proportional to the volume, representing the change in Gibbs free

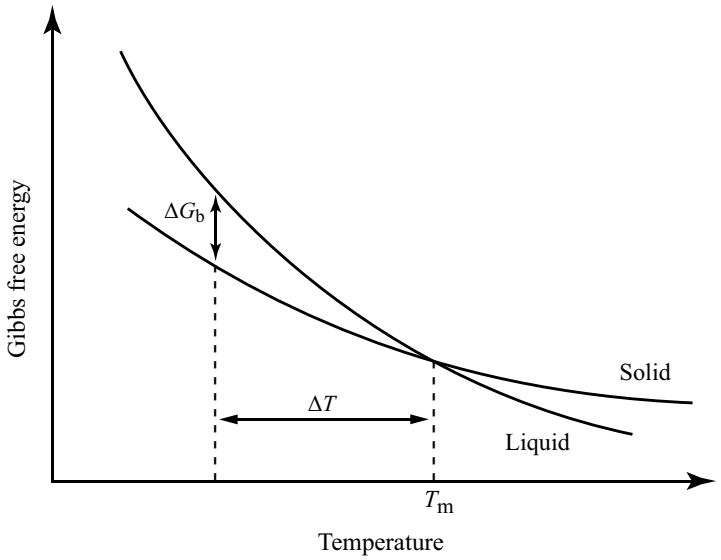

FIGURE 2.3: Schematic diagram of the Gibbs free energy as a function of temperature near a melting temperature T_m. ΔG_b is the change in free energy per particle in a undercooled melt by ΔT.

energy in going from liquid to solid (Figure 2.4)

$$\Delta G(r) = \frac{4}{3}\pi r^3 \Delta G_b + 4\pi r^2 \gamma_{sl}. \tag{2.7}$$

The free energy change has a maximum at a critical radius r^* given by

$$r^* = \frac{-2\gamma_{sl}}{\Delta G_b}. \tag{2.8}$$

Crystals bigger than r^* can continue to grow and smaller crystals are unstable and will remelt [7]. When an undercooled melt freezes, the free energy change per unit volume takes the form[2]

$$\Delta G_b = -\frac{\Delta H_m}{T_m}\Delta T. \tag{2.9}$$

[2]This approximation is reasonable only when the undercooling ΔT is much smaller than the melting temperature ($\Delta T \ll T$). This is because for the entropy change on melting we assume $\Delta S_m = \left(\frac{\partial G_s}{\partial T}\right)_P - \left(\frac{\partial G_l}{\partial T}\right)_P = \frac{\Delta H_m}{T_m}$. When ΔT is small enough, the partial derivatives are approximately constant and we can write the Equation (2.9).

Therefore the free energy barrier ΔG^* associated with the critical nucleus size which must be overcome by thermal fluctuation is given by [7]

$$\Delta G^* = \frac{16\pi}{3}\gamma_{sl}^3 \left(\frac{T_m}{\Delta H_m}\right)^2 \frac{1}{\Delta T^2}. \tag{2.10}$$

Hard–Sphere Case:

The hard–sphere system is independent of temperature and its freezing is driven by entropic forces. The thermal energy k_BT just normalizes the free energy in the HS system. If the HS liquid is compressed (or equivalently density is increased), it freezes into an ordered, solid phase. This transition is accompanied by a discontinuous change in volume ΔV and entropy ΔS. The difference in free energy of the HS solid and fluid phases at a given temperature is equal to $F = -T\Delta S$. One of the most significant finding to emerge from the molecular simulations [13, 14] is that the HS fluid freezes into a stable, face–centered cubic (fcc) crystal and accurate calculations [15, 16] show that the packing fractions at coexistence in the fluid and solid phases are $\eta_f \approx 0.494$ and $\eta_s \approx 0.545$ and the coexistence pressure equals $p_{\text{coex}} = 11.576\, k_BT/\sigma^3$ [16].

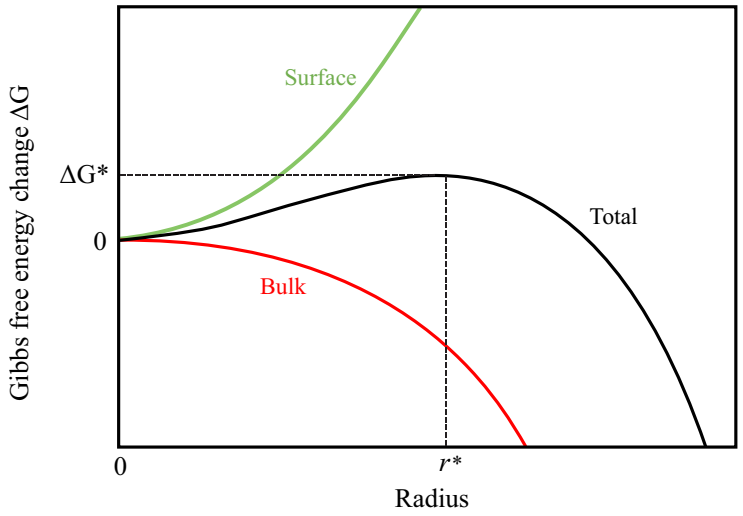

FIGURE 2.4: Schematic diagram of the change in Gibbs free energy when a crystal of radius r is nucleated in a melt cooled below its melting point.

- **Heterogeneous Nucleation**

  Heterogeneous nucleation occurs much more often than homogeneous nucleation. Pre–existing surfaces of different or the same solids in the melt usually lower the activation energy for nucleation of a new crystal and it is typically much faster than homogeneous nucleation because the nucleation barrier is much lower at a surface.

2.2 Statistical Mechanics

2.2.1 Principle of Statistical Physics and Ensembles

Statistical systems are complex systems. The systems are so complex that we cannot obtain all the information to completely characterize them. For example, a liter of gas contains about 10^{22} atoms. To completely characterize such a system (or more precisely, a state of such a system), we need to known the three components of the velocity for each atom and the three components of the position for each atom. It is impossible to obtain 6×10^{22} real numbers to completely characterize the gas. However, not knowing all the information needed to characterize gas does not prevent us from developing a theory of gas. This is because we are only interested in some average properties of gas such as the pressure, volume and temperature. Those properties do not depend on every little details of each atoms. Not knowing every thing about the atoms does not prevent us from calculating those average properties. This is the kind of problems in statistical physics. In statistical physics we try to understand the properties of a complex system without knowing all the information of the systems [17].

2.2.1.1 All Possible States Appear with an Equal Probability

In statistical physics there is only one principle: All possible states appear with an equal probability. Suppose we know certain quantities, such as pressure, total energy, etc, of a complex system. But those quantities do not characterize the system completely. This means that the system has a number of states for which those quantities take the same values. Thus even after knowing the values of those quantities, we still do not know,

among those possible states, which state the system is actually in. Then according to the principle of statistical physics, all the possible states are equally likely.

2.2.1.2 Time Average and Ensemble Average

Statistical physics is a science that deals with ensembles, rather than individual systems. Since the ensembles under study are stationary, the ensemble average of a physical quantity f will be independent of time. It means that taking a time average will not change the results

$$\begin{aligned} \langle f \rangle &\equiv \text{the ensemble average of } f \\ &= \lim_{T\to\infty} \frac{1}{T} \int_0^T \langle f \rangle dt. \end{aligned} \tag{2.11}$$

The process of time averaging and ensemble averaging are completely independent, so changing the order of averaging will not change the value of $\langle f \rangle$

$$\langle f \rangle = \left\langle \lim_{T\to\infty} \frac{1}{T} \int_0^T f\, dt \right\rangle. \tag{2.12}$$

Now the time average of any physical quantity taken over a sufficiently long interval of time, is the same for every member of the ensemble. Therefore taking the ensemble average should be inconsequential. Thus we may write

$$\langle f \rangle = \lim_{T\to\infty} \frac{1}{T} \int_0^T f\, dt. \tag{2.13}$$

Furthermore the long–time average of a physical quantity is the quantity we may obtain by measuring that quantity experimentally [17]

$$\langle f \rangle = f_{\text{exp}}. \tag{2.14}$$

The two (time and ensemble) averaging approaches are equivalent only when the system can visit all the possible states many times during a long period of time. This is the ergodicity hypothesis. Not all systems are ergodic. For a non–ergodic system, statistical physics only apply to its ensemble. For an ergodic system, statistical physics also apply to the time average of the system [18].

2.2.2 Microcanonical Ensemble

Consider an isolated, macroscopic system on N identical, spherical particles of mass m enclosed in a volume V. In classical mechanics the dynamical state of the system is completely specified by $3N$ coordinates $\mathbf{r}^N = \mathbf{r}_1, \ldots, \mathbf{r}_N$ and $3N$ momenta $\mathbf{p}^N = \mathbf{p}_1, \ldots, \mathbf{p}_N$ of the particles. The values of these $6N$ variables define a phase point in a 6N–dimensional phase space. The hamiltonian of the system $\mathcal{H}$ can be written as follows

$$\mathcal{H}(\mathbf{r}^N, \mathbf{p}^N) = K_N(\mathbf{p}^N) + V_N(\mathbf{r}^N) + V_{\text{ext}}(\mathbf{r}^N), \tag{2.15}$$

where

$$K_N = \sum_{i=1}^{N} \frac{|\mathbf{p}_i|^2}{2m}, \tag{2.16}$$

is the kinetic energy, V_N is the interatomic potential energy and V_{ext} is the potential energy due to an external field. A microcanonical ensemble is an ensemble formed by isolated systems with a same particle number N and a same energy E in a same volume V. Here by same energy we really mean that the system has an energy which lies within a small window between E and $E + \Delta E$. By definition, such a system exchanges neither particles nor energy with the surroundings. In thermal equilibrium, the density distribution function $\rho(\mathbf{r})$ is given by

$$\rho(\mathbf{r}) \quad = \quad \begin{cases} \frac{1}{\omega(E,V,N)} & \text{if } E < \mathcal{H}(\mathbf{r}^N, \mathbf{p}^N) < (E + \Delta E) \\ 0 & \text{otherwise} \end{cases} , \tag{2.17}$$

and the volume of the phase space accessible to the representative points of the system ω, is given by

$$\omega(E, V, N) = \int \int_{E < \mathcal{H}(\mathbf{r}^N, \mathbf{p}^N) < E + \Delta E} \mathrm{d}^N\mathbf{r}\, \mathrm{d}^N\mathbf{p}. \tag{2.18}$$

Statistical mechanics is related to thermodynamics by the Boltzmann's equation which relates the entropy, S, to the number of microstates, Γ, corresponding to given macrostate

$$S(E, V, N) = k_B \log(\Gamma(E, V, N)). \tag{2.19}$$

where $\Gamma(E,V,N) = \left(\frac{\omega(E,V,N)}{h^{3N}N!}\right)$ and h is the Plank constant [17].

2.2.3 Canonical Ensemble

Physically, the concept of a fixed energy (or even an energy range) for a system belonging to the real world does not appear satisfactory. For one thing, the total energy E of a system is hardly ever measured; for another, it is hardly possible to keep its value under strict physical control. A far better alternative appears to be to speak of a fixed temperature T of the system – a parameter which is not only directly observable but also controllable. The equilibrium probability density for a system of N identical, spherical particles is

$$f_0(\mathbf{r}^N, \mathbf{p}^N) = \frac{1}{h^{3N}N!}\frac{\exp(-\beta\mathcal{H}(\mathbf{r}^N, \mathbf{p}^N))}{Q_N}. \tag{2.20}$$

The normalization constant Q_N is the canonical partition function

$$Q(T,V,N) = \frac{1}{h^{3N}N!}\int \mathrm{d}^N\mathbf{r}\,\mathrm{d}^N\mathbf{p}\ \exp(-\beta\mathcal{H}(\mathbf{r}^N, \mathbf{p}^N)). \tag{2.21}$$

If the hamiltonian is separated into kinetic and potential energy terms, the integrations over momenta can be carried out analytically. This allows the partition function to be written as

$$Q_N = \frac{Z_N}{\Lambda^{3N}N!}, \tag{2.22}$$

where $\Lambda = h/\sqrt{2\pi m k_B T}$ is the thermal De Broglie wavelength and

$$Z_N = \int \mathrm{d}^N\mathbf{r}\ \exp(-\beta V_N), \tag{2.23}$$

is the *configuration integral*.

The corresponding thermodynamic potential for the canonical ensemble is the Helmholtz free energy $F(T,N,V)$, defined as

$$F = U - TS, \tag{2.24}$$

where U is the internal energy and S is the entropy of the system. The canonical statistical mechanics can be linked to thermodynamics via a relation between the thermodynamic potential and the partition function

$$F(T, N, V) = -k_B T \log Q_N(T, V, N). \tag{2.25}$$

In the absence of any external potential we may write an expression for the internal energy as follow

$$U = TS - PV + \mu N. \tag{2.26}$$

If the free energy of a system is known, all other thermodynamic information of the system can be extracted using differentiation

$$\begin{aligned} S &= -\left(\frac{\partial F}{\partial T}\right)_{V,N}, \\ P &= -\left(\frac{\partial F}{\partial V}\right)_{T,N}, \\ \mu &= \left(\frac{\partial F}{\partial N}\right)_{T,V}. \end{aligned} \tag{2.27}$$

In the rest of this section the ideal gas system of non–interacting classical particles is studied. For the case of an ideal gas $V_N = 0$, thus the configuration integral gives rise to

$$Z_N = \int \dots \int \mathrm{d}\mathbf{r}_1 \dots \mathrm{d}\mathbf{r}_N = V^N. \tag{2.28}$$

Hence the canonical partition function Q_N (Equation (2.22)) of a unifirm ideal gas is

$$Q_N^{\mathrm{id}} = \frac{V^N}{\Lambda^{3N} N!}. \tag{2.29}$$

We can calculate the free energy of the ideal gas system

$$F_{\mathrm{id}}(T, N, V) = N k_B T \left[\log\left(\Lambda^3 \frac{N}{V}\right) - 1\right], \tag{2.30}$$

which is obtained using Stirling's approximation[3]. Other thermodynamic quantities can be obtained. The expression for the energy

$$E = -\frac{\partial}{\partial \beta} \log Q^{\mathrm{id}}(T, V, N), \tag{2.31}$$

and pressure

$$P = k_B T \left(\frac{\partial \log Q^{\mathrm{id}}(T, V, N)}{\partial V} \right), \tag{2.32}$$

gives rise to the results $E = 3Nk_BT/2$ and $PV = NKT$. In addition the chemical potential of the ideal gas is obtained by

$$\mu_{\mathrm{id}} = \frac{\partial F_{\mathrm{id}}(T, N, V)}{\partial N} = k_B T \log \left(\Lambda^3 \frac{N}{V} \right). \tag{2.33}$$

2.2.4 Grand Canonical Ensemble

In the preceding section the canonical ensemble was introduced. The effectiveness of that approach became clear from the ideal gas example discussed there. However for a number of problems the usefulness of the canonical ensemble formalism turns out to be rather limited. It comes from the realization that not only the energy of a system but the number of particles as well is hardly ever measured in a *direct* manner. Therefor we may regard both N and E as *variables* and identify their expectation values, $\langle N \rangle$ and $\langle E \rangle$, with the corresponding thermodynamic quantities. The grand canonical ensemble describes systems that allow energy and particle exchange at a fixed volume V, temperature T and chemical potential μ. The ensemble probability density is a function of $6N$ phase–space variables $\mathbf{r}^N, \mathbf{p}^N$ and has the form

$$f_0(\mathbf{r}^N, \mathbf{p}^N;\, N) = \frac{\exp(-\beta(\mathcal{H}(\mathbf{r}^N, \mathbf{p}^N) - N\mu))}{\Xi}, \tag{2.34}$$

where the grand canonical partition function is

$$\begin{aligned} \Xi(T, V, \mu) &= \sum_{N=0}^{\infty} \frac{1}{h^{3N} N!} \int \mathrm{d}^N \mathbf{r}\, \mathrm{d}^N \mathbf{p}\ \exp(-\beta(\mathcal{H}(\mathbf{r}^N, \mathbf{p}^N) - \mu N)) \\ &= \sum_{N=0}^{\infty} \frac{z^N}{N!} Q_N, \end{aligned} \tag{2.35}$$

[3]Stirling's approximation (or Stirling's formula) for factorials: $\log(N!) = N \log(N) - N + \mathcal{O}(\log(N))$.

here Q_N denotes the canonical partition function of a system with N particles and the *activity* z is

$$z = \frac{\exp(\beta\mu)}{\Lambda^3}. \tag{2.36}$$

The link with thermodynamics is established through the relation

$$\Omega(T, V, \mu) = -k_B T \log(\Xi(T, V, \mu)), \tag{2.37}$$

where Ω denotes the grand (or Landau) potential. The grand potential is defined in terms of the Helmholtz free energy by

$$\Omega = F - N\mu. \tag{2.38}$$

When the internal energy is given by Equation (2.26), the grand potential reduces to

$$\Omega = -PV. \tag{2.39}$$

Using the differential form of Equation (2.38), the thermodynamic functions S, P and N are given as derivatives of Ω by

$$\begin{aligned} S &= -\left(\frac{\partial\Omega}{\partial T}\right)_{V,\mu}, \\ P &= -\left(\frac{\partial\Omega}{\partial V}\right)_{T,\mu}, \\ N &= -\left(\frac{\partial\Omega}{\partial \mu}\right)_{T,V}. \end{aligned} \tag{2.40}$$

Equations (2.33) and (2.36) show that $z = N/V = \rho$ for a uniform ideal gas and in that case Equation (2.35) reduces to

$$\Xi^{\mathrm{id}} = \sum_{N=0}^{\infty} \frac{\rho^N V^N}{N!} = \exp(\rho V), \tag{2.41}$$

which, together with Equation (2.39), yield the equation of state in the form $\beta P = \rho$.

2.3 Particle Densities and Distribution Functions

All the information on the equilibrium properties of a many–body system is encoded, in increasing degree of detail, into the thermodynamic potentials (e.g., its Helmholtz free energy or the grand potential) at given conditions and its n–body correlation functions ($n < N$). The n–body correlation function describes the joint probability of finding n particles in the system in elementary volumes d^3r centered around the points $\mathbf{r}_1, \mathbf{r}_2, \ldots, \mathbf{r}_n$, in space. We very rarely need information of a system in such details and in practice correlation functions up to the pair level ($n \leq 2$) is sufficient [19]. Accordingly, two operators $\hat{\rho}^{(1)}(\mathbf{r})$ and $\hat{\rho}^{(2)}(\mathbf{r}, \mathbf{r}')$, called one– and two–particle density operators are defined respectively as follows

$$\hat{\rho}^{(1)}(\mathbf{r}) = \sum_{i=1}^{N} \delta(\mathbf{r} - \mathbf{r}_i), \tag{2.42}$$

and

$$\hat{\rho}^{(2)}(\mathbf{r}, \mathbf{r}') = \sum_{i=1}^{N} \sum_{j=1}^{N} \delta(\mathbf{r} - \mathbf{r}_i)\delta(\mathbf{r}' - \mathbf{r}_j) - \sum_{i=1}^{N} \delta(\mathbf{r} - \mathbf{r}_i)\delta(\mathbf{r}' - \mathbf{r}_i), \tag{2.43}$$

where $\mathbf{r}_{i,j}$ are the instantaneous particle coordinates and $\mathbf{r}, \mathbf{r}'$ denote arbitrary observation points in space. The one– and two–particle densities $\rho^{(1)}(\mathbf{r})$ and $\rho^{(2)}(\mathbf{r}, \mathbf{r}')$ are the expectation values of the corresponding operators in the chosen ensemble. The one–body density $\rho^{(1)}(\mathbf{r})$ is proportional to the probability density of finding any particle of the system around $\mathbf{r}$, whereas the two–body density $\rho^{(2)}(\mathbf{r}, \mathbf{r}')$ is proportional to the probability density of finding simultaneously any particle of the system around $\mathbf{r}$ and a different particle of the system around $\mathbf{r}'$. For a uniform fluid

$$\rho^{(1)}(\mathbf{r}) = \frac{N}{V} = \rho. \tag{2.44}$$

The two–body density for solids is orientation dependent but for liquids and gases depends only on the magnitude of the difference of its arguments

$$\rho^{(2)}(\mathbf{r}, \mathbf{r}') = \rho^{(2)}(|\mathbf{r} - \mathbf{r}'|). \tag{2.45}$$

In the theory of classical fluids, a quantity of central importance for investigation of the pair structure of the system is the pair (radial) distribution function $g(|\mathbf{r} - \mathbf{r}'|)$ defined

through

$$\rho^{(2)}(|\mathbf{r}-\mathbf{r}'|) = \rho^2 g(|\mathbf{r}-\mathbf{r}'|). \tag{2.46}$$

The pair distribution function is a good measure to distinct between the spatial arrangements of molecules in gases, liquids and solids. Pair distribution function $g(\mathbf{r}, \mathbf{r}')$ is a measure of the probability of finding a particle at position $\mathbf{r}'$ given that another particle is located at position $\mathbf{r}$. Typical shapes of the pair distribution function for gas, liquid and solid phases are shown in Figure 2.5. In general, the n–particle distribution function

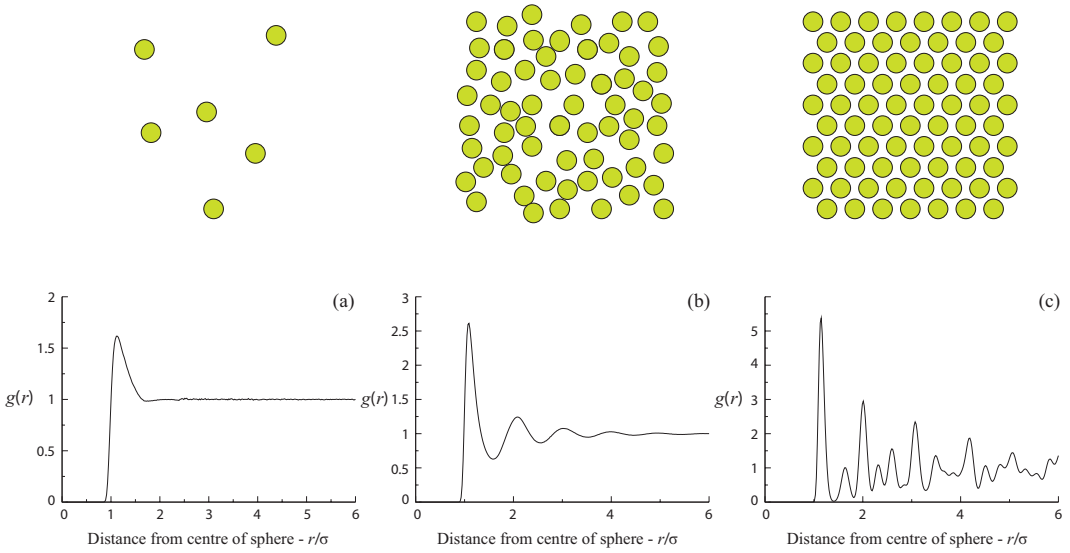

FIGURE 2.5: Typical pair distribution function for (a) a gas, (b) a liquid and (c) a solid [20].

reads as

$$g^{(n)}(\mathbf{r}_1, \ldots, \mathbf{r}_n) = \frac{\rho^{(n)}(\mathbf{r}_1, \ldots, \mathbf{r}_n)}{\prod_{i=1}^{n} \rho^{(1)}(\mathbf{r}_i)}. \tag{2.47}$$

The total correlation function is defined as follows

$$h(r) = g(r) - 1, \tag{2.48}$$

which is a measure of the influence of molecule 1 on molecule 2 at a distance r away with $g(r)$ as the pair distribution function. In 1914 Ornstein ans Zernike proposed to

split the total correlation function into two contributions, direct and indirect parts [21]. The direct contribution is defined to be given the direct correlation function $c(r)$ and the indirect part is due to the influence of molecule 1 on molecule 3 which in turn affects molecule 2 directly and indirectly

$$h(r) = c(r) + \rho \int \mathrm{d}\mathbf{r}' \; c(|\mathbf{r} - \mathbf{r}'|)h(r'). \tag{2.49}$$

The Ornstein–Zernike (OZ) relation is a definition of $c(r)$. Another important quantity is the structure factor $S(k)$ as a three dimensional Fourier transform of the total correlation function $h(r)$

$$S(k) = 1 + \rho \int \mathrm{d}\mathbf{r} \; h(r) \exp(-i\mathbf{k} \cdot \mathbf{r}). \tag{2.50}$$

For the point particles, the scattering intensity is directly proportional to $S(k)$ [22] and for large particles, such as colloids, the form factor $P(k)$ of the particles has to be taken into account and the scattering intensity is proportional to the product $P(k)S(k)$. This makes the structure factor an important tool to test the accuracy of the soft matter theories.

Chapter 3

Theory: From Density Functional Formalism to Stillinger's Approach

In this chapter we introduce the classical Density Functional Theory (DFT) as one of the core theoretical approaches for studying inhomogeneous systems. After a short introduction in Section 3.1, this chapter first introduces DFT and explains the different approaches for approximating various functionals (Section 3.2). Section 3.3 is dedicated to the Fundamental Measure Theory (FMT) as the most natural approximate scheme to approximate the free energy functionals and different versions of FMT will be presented in this section. Section 3.4 presents Stillinger's expansion in correlated, contiguous particles to approximate the free energy of a system and 3.5 recapitulates the dynamical DFT. This chapter is mostly based on references [22–24].

3.1 Introduction

Density functional theory was first invented by Hohenberg and Kohn [6] to find out the equilibrium density distribution $\rho(\mathbf{r})$ of inhomogeneous systems at interfaces between coexistence phases or in the presence of an external potential $V_{\text{ext}}(\mathbf{r})$. In most cases, like layering of fluids against walls or liquids confined in nano–capillaries, the sharpest level of density variation comes from the effects of molecular packing, and hence the development

of density functional theories for hard–core models has been a main objective in this field [25, 26]. In 1976, Percus [27] presented the free energy density functional for one–dimensional (1D) hard–rods (HR). In his work both an exact case to test the internal relation of the density functional formalism and a hint on how to approximate the free energy of two–dimensional (2D) hard disk (HD) and three–dimensional (3D) of hard sphere (HS) systems have been studied. Over the last decades, there has been an impressive improvement in the quality of these approximations, with milestones in the weighted density approximation (WDA) in the middle 1980s and the fundamental measure theory (FMT) over the 1990s [24]. Introducing Fundamental Measure Theory (FMT) for hard–sphere *mixtures* by Rosenfeld [28] and generalization of Percus' *exact* one–dimensional DFT for hard rods [27] by Vanderlick and co–workers [29] both in 1989, made a remarkable year for classical DFT. Later, Tarazona, Rosenfeld, Evans and other people improved the quality of the functional to make FMT successful in describing the properties of the hard–sphere fluid, solid and crystallization.

3.2 Density Functional Theory

In the framework of density functional theory, for any given temperature ($\beta = 1/k_B T$) and form of the pair molecular interaction potential $u(\mathbf{r}_i - \mathbf{r}_j)$ there is a unique free energy functional $\mathcal{F}[\rho]$, which is a functional of the one–body density distribution $\rho(\mathbf{r})$. This free energy functional is independent of the external potential $V_{\text{ext}}(\mathbf{r})$.

The grand potential has temperature and intrinsic chemical potential as its natural variables. However, it turns out to be more profitable to treat one–body density rather than intrinsic chemical potential. Density functional theory profits from the functional of one–body density to determine the free energy of a classical thermodynamic system. All the thermodynamic properties of the system can be extracted using the free energy functional. The key ideal is that $\mathcal{F}[\rho]$ is a *unique* functional of $\rho(\mathbf{r})$; its functional form does not depend on the external potential $V_{\text{ext}}(\mathbf{r})$. For a given interparticle potential function $u(\mathbf{r}_i - \mathbf{r}_j)$ and fixed values of temperature T and chemical potential μ, there is only one external potential that gives rise to a specific density profile. The proof of existence and uniqueness of this functional is given in Appendix A.

In the grand canonical ensemble, the free energy functional can be expressed as a functional of one–bode density ρ

$$\Omega[\rho] \equiv \mathcal{F}[\rho] + \int \mathrm{d}\mathbf{r}\, \rho(\mathbf{r})(V_{\mathrm{ext}}(\mathbf{r}) - \mu), \tag{3.1}$$

where μ denotes the chemical potential and $V_{\mathrm{ext}}(\mathbf{r})$ is the external potential. Here $\rho(\mathbf{r})$ is not necessarily the equilibrium density distribution $\rho_{\mathrm{eq}}(\mathbf{r})$. For the equilibrium density distribution ρ_{eq}, the functional is minimized and reduces to the grand potential of the system $\Omega[\rho_{\mathrm{eq}}] = \Omega$

$$\left.\frac{\delta\Omega[\rho]}{\delta\rho}\right|_{\rho=\rho_{\mathrm{eq}}} \equiv \frac{\delta\mathcal{F}[\rho]}{\delta\rho} + V_{\mathrm{ext}}(\mathbf{r}) - \mu = 0, \tag{3.2}$$

in terms of the functional derivative of the intrinsic Helmholtz free energy $\mathcal{F}[\rho]$. The Helmholtz free energy functional is conventionally split into an ideal gas part (without particle interaction) and excess (over ideal) part

$$\mathcal{F} \equiv \mathcal{F}_{\mathrm{id}} + \mathcal{F}_{\mathrm{ex}}, \tag{3.3}$$

where the excess part includes all the particle interactions.

The explicit knowledge of the (exact or approximation) free energy density functional would reduce the equilibrium statistical mechanics of inhomogeneous systems to a problem of functional minimization with respect to the one–particle distribution $\rho(\mathbf{r})$, and this would represent a huge simplification with respect to the direct evaluation of the grand partition function. DFT has found application to a very wide range of problems, some of which are discussed in later chapters. As in any variational calculation, the success achieved depends on the skill with which the trial functional is constructed. Since $\mathcal{F}$ is a unique functional of ρ, a good approximation would be one that is suitable for widely differing choices of external potential.

3.2.1 The Ideal Gas and the Excess Free Energy Density Functional

The classical ideal (non–interaction) gas, $u(\mathbf{r}_{ij}) = 0$, provides the simplest example of the density functional formalism. For such a system the grand partition function can be expressed as

$$\Xi_{\mathrm{id}} = \sum_{N=0}^{\infty} \frac{(e^{\beta\mu}Q_1)^N}{N!} = \exp(Q_1 e^{\beta\mu}), \tag{3.4}$$

in terms of the one–body partition function

$$Q_1 = \int \mathrm{d}\mathbf{r}\, e^{(-\beta V_{\mathrm{ext}}(\mathbf{r}))}. \tag{3.5}$$

The equilibrium grand potential energy is

$$\Omega_{\mathrm{id}}[V_{\mathrm{ext}}] \equiv -\frac{1}{\beta}\log(\Xi_{\mathrm{id}}) = -\frac{e^{\beta\mu}}{\beta}\int \mathrm{d}\mathbf{r}\, e^{-\beta V_{\mathrm{ext}}(\mathbf{r})}, \tag{3.6}$$

and the equilibrium density distribution follows the simple form

$$\Lambda^3\rho_{\mathrm{id}}(\mathbf{r}) = e^{\beta(\mu - V_{\mathrm{ext}}(\mathbf{r}))}. \tag{3.7}$$

Using these results and Equation (3.1) one can get the explicit functional form of the ideal gas intrinsic free energy,

$$\beta\mathcal{F}_{id}[\rho] = \int \mathrm{d}\mathbf{r}\, \rho(\mathbf{r})[\ln(\Lambda^3\rho(\mathbf{r})) - 1], \tag{3.8}$$

and the functional derivative of $\mathcal{F}_{id}[\rho]$ reads

$$\frac{\delta\mathcal{F}_{\mathrm{id}}[\rho]}{\delta\rho(\mathbf{r})} = \frac{1}{\beta}\ln\left(\Lambda^3\rho(\mathbf{r})\right). \tag{3.9}$$

The free energy of hard core systems is *purely* entropic and it may be split in two parts, the ideal gas contribution, $\mathcal{F}_{\mathrm{id}}[\rho]$, and *excess* free energy, $\mathcal{F}_{\mathrm{ex}}[\rho]$, which contains all the information about interactions between particles. The excess part is responsible for entropy reduction due to the non–overlap of the particle cores in the system. The total free energy is usually written in k_BT units as

$$\beta\mathcal{F}[\rho] = \beta\mathcal{F}_{\mathrm{id}}[\rho] + \beta\mathcal{F}_{\mathrm{ex}}[\rho] \equiv \int \mathrm{d}\mathbf{r}\,\{\Phi_{\mathrm{id}}\left(\rho(\mathbf{r})\right) + \Phi([\rho];\mathbf{r})\}, \tag{3.10}$$

where the ideal free energy density $\Phi_{\mathrm{id}}(\rho)$, as a function is evaluated at the local density, while the excess contribution is expressed as a volume integral of an excess free energy density $\Phi([\rho];r)$, which is a function of $\mathbf{r}$ and a *functional* of $\rho(\mathbf{r})$. In contrast to the ideal gas contributions, the excess free energy functionals $\mathcal{F}_{\mathrm{ex}}[\rho]$ is not known exactly. There are many ways to construct the excess free energy of the system in terms of local contributions. Different approaches to $\mathcal{F}_{\mathrm{ex}}[\rho]$ may give similar results with very different $\Phi([\rho];\mathbf{r})$ and the goal of DFT is to develop and use better approximations for $\Phi([\rho];\mathbf{r})$.

3.2.2 Density Functional Virial Expansion of the Excess Free Energy

The usual virial expansion for thermodynamics and correlation structure of bulk fluids may be extended to get the generic density expansion of $\mathcal{F}_{\rm ex}[\rho]$ in systems with pairwise interactions,

$$\begin{aligned}\beta\mathcal{F}_{\rm ex}[\rho] = &- \frac{1}{2}\int d\mathbf{r}_1\,\rho(\mathbf{r}_1)\int d\mathbf{r}_2\,\rho(\mathbf{r}_2)f(r_{12}) \\ &- \frac{1}{6}\int d\mathbf{r}_1\,\rho(\mathbf{r}_1)\int d\mathbf{r}_2\,\rho(\mathbf{r}_2)\int d\mathbf{r}_3\,\rho(\mathbf{r}_3)f(r_{12})f(r_{13})f(r_{23}) \\ &+ \mathcal{O}(\rho^4),\end{aligned} \tag{3.11}$$

where $r_{ij} = |\mathbf{r}_i - \mathbf{r}_j|$ and the Mayer–f function is given by

$$f(\mathbf{r}) = \exp(\beta u(\mathbf{r})) - 1, \tag{3.12}$$

with the pairwise potential $u(\mathbf{r})$. In the case of hard–sphere interaction, $f(\mathbf{r})$ has a purely geometrical interpretation:

$$u(r) = \begin{cases} \infty & r < 2R \\ 0 & \text{otherwise} \end{cases} \Rightarrow f(r) = \begin{cases} -1 & r < 2R \\ 0 & \text{otherwise} \end{cases},$$

i.e. the Mayer–f function marks the volume that is not accessible to the center of one sphere (with radius R) close to another sphere. This excluded volume is the volume of a sphere of radius $2R$.

The *direct* correlation function for a system with uniform density is generated hierarchy by

$$c^{(n)}(\mathbf{r}_1,\ldots,\mathbf{r}_n;\rho_0) = -\beta\frac{\delta^n\mathcal{F}_{\rm ex}}{\delta\rho(\mathbf{r}_1)\ldots\delta\rho(\mathbf{r}_n)}\bigg|_{\rho=\rho_0(\mathbf{r})}. \tag{3.13}$$

As expected, the lowest order of the excess free energy DF produced by the interactions between the particles is quadratic in $\rho(\mathbf{r})$, while its second functional derivative has a zero density limit $c(r,\,0) = -f(r)$. These exact low density results for $\beta\mathcal{F}_{\rm ex}[\rho]$ provide useful hints for the development of DF approximations.

3.2.3 The Local Density Approximation and the Gradient Expansion

The Local Density Approximation (LDA) is the simplest scheme to build a DF approximation for $\mathcal{F}_{\rm ex}[\rho]$ from the restricted knowledge of the thermodynamics of uniform systems. This DF form approximates the local excess free energy density as a function of the local density, $\Phi_{LDA}([\rho];\,\mathbf{r}) = \Phi(\rho(\mathbf{r}))$, where $\Phi(\rho_0)$ is the excess free energy per unit volume in a system with uniform density ρ_0, directly accessible from its equation of state. The ideal gas free energy DF has exactly the local density form (3.8), but the generic form of the excess part ,$\Phi([\rho];\,\mathbf{r})$, depends on the density distribution at different positions, as already observed in the first term of the virial expansion (Equation (3.11)), so that the LDA can only give acceptable results if $\rho(\mathbf{r})$ changes very smoothly over molecular size distances. The LDA description of the HS excess free energy may also be regarded as a *coarse grained* description of $\rho(\mathbf{r})$, when we are interested in its long–ranged aspects rather than in the molecular layering structure [30].

For systems with attractive interactions, there is a systematic, although limited way to improve the LDA in terms of density gradient expansions [6], assuming that the generic functional $\Phi([\rho];\,\mathbf{r})$ is not just a local function of $\rho(\mathbf{r})$ but also of its local gradient $\nabla\rho(\mathbf{r})$. The van der Waals theory for the structure of the liquid surface may be considered as the precursor of that DF approximation [31], well before the DF formalism was established. However, the approach fails from the beginning when applied to systems with hard–core interactions. The non–local dependence of $\Phi([\rho];\,\mathbf{r})$ implies a sharp finite range of interference between $\rho(\mathbf{r})$ and $\rho(\mathbf{r}')$, associated to the geometry of the molecule, and this cannot.

3.2.4 The Mean Field Approximation

For systems with very soft molecular potentials, the particles may be assumed to be fully uncorrelated, as in the ideal gas, so that $\mathcal{F}_{\rm ex}[\rho]$ has got no entropic contribution and is given by the interaction energy

$$\mathcal{F}_{\rm ex}[\rho] = \frac{1}{2}\int \mathrm{d}\mathbf{r}\,\mathrm{d}\mathbf{r}'\,\rho(\mathbf{r})\rho(\mathbf{r}')u(\mathbf{r}-\mathbf{r}'). \tag{3.14}$$

This is the Mean Field Approximation (MFA) DF [25], since the functional derivative in Equation (3.2) takes the form

$$\frac{\delta \mathcal{F}_{\rm ex}[\rho]}{\delta \rho} = \int \mathrm{d}\mathbf{r}'\, \rho(\mathbf{r}') u(\mathbf{r}-\mathbf{r}'), \tag{3.15}$$

and it is interpreted as the potential created on a particle at $\mathbf{r}$ by the (uncorrelated) mean distribution of particles over the whole system. The MFA may give an accurate description of the full excess free energy for ultra–soft interactions, like those between polymer chains in good solvents [32], but it is obviously out of question for the description of hard–core interactions with an infinite $u(r)$ inside the molecular cores. The relevance of the MFA comes from the usual treatment of simple liquids to split the interaction potential in a repulsive core, $u_{\rm rep}(r)$, often described as a reference HS with temperature–dependent diameter and the soft attractive part $u_{\rm att}(r)$, which may be included through the MFA [25]. Such a simple addition of the molecular packing and the attractive interaction effects is sometimes referred to as a generalized van der Waals approximation, and it is the simplest and very successful approach to the DFT of realistic model interactions.

The excess free energy functional $\mathcal{F}_{\rm ex}$ can be expanded around the background density profiles ρ_0

$$\begin{aligned} \beta \mathcal{F}_{\rm ex}[\rho] &= \beta \mathcal{F}_{\rm ex}[\rho_0] - \int \mathrm{d}\mathbf{r}\, c^{(1)}(\mathbf{r};\rho_0)\Delta\rho(\mathbf{r}) \\ &\quad -\frac{1}{2}\int \mathrm{d}\mathbf{r}\,\mathrm{d}\mathbf{r}'\, c^{(2)}(\mathbf{r},\mathbf{r}';\rho_0)\Delta\rho(\mathbf{r})\Delta\rho(\mathbf{r}'), \end{aligned} \tag{3.16}$$

where $\mathcal{F}_{\rm ex}[\rho_0]$ is the excess free energy pertaining to the background profile $\Delta\rho(\mathbf{r}) = \rho(\mathbf{r}) - \rho_0$. In general the background density $\rho_0(\mathbf{r})$ can depend on the position. $c^{(1)}$ and $c^{(2)}$ are the first two members in the hierarchy of the direct correlation function (3.13). In most practical applications the reference density is taken to be a reference bulk density, $\rho_0 \equiv$ const.. Therefore $c^{(1)} = \beta\mu_{\rm ex} = \beta\mu - \ln(\Lambda^3\rho_0)$ and $c^{(2)}(\mathbf{r}-\mathbf{r}';\rho_0)$ depends only on the coordinate difference of two positions $\mathbf{r}$ and $\mathbf{r}'$. To evaluate the functional in Equation (3.16), the correlation function $c^{(2)}$ has to be determined as an external input, provided e.g., by integral equation theory or by simple approximations of the reciprocal lattice vectors (RLV) type [6]. The Taylor–expanded functional appears to be merely a suitable qualitative tool to explore basic features of dense liquids in the

vicinity of the solid or glass transition (see, e.g., Refs. [33, 34]) and should hold only for modest departure from the reference density [35].

The Taylor expanded functional in Equation (3.16) is nonlocal in densities. Through an additional expansion, so–called gradient expansion, it can be transformed into a local form. By expansion of the Fourier transform of the direct correlation function around a constant reference density ρ_0

$$\tilde{c}^{(2)}(k;\rho) = -c_0 + c_2 k^2 - c_4 k^4 \ldots, \tag{3.17}$$

Equation (3.16) takes the form

$$\begin{aligned} \beta\mathcal{F}_{\mathrm{ex}}[\rho] &= \beta\mathcal{F}_{\mathrm{ex}}[\rho_0] + \beta\mu_{\mathrm{ex}} \int \mathrm{d}\mathbf{r}\, \Delta\rho(\mathbf{r}) \\ &\quad + \frac{1}{2} \int \mathrm{d}\mathbf{r}\, \Delta\rho(\mathbf{r})(c_0 + c_2\nabla^2 + c_4\nabla^4 \ldots)\Delta\rho(\mathbf{r}) + \ldots. \end{aligned} \tag{3.18}$$

On sees that the excess free energy density contains local terms up to order 2 in $\Delta\rho$ and up to order 4 in $\nabla(\Delta\rho.)$. We can define the dimensionless density difference as an order parameter

$$\phi(\mathbf{r}) = \frac{\rho(\mathbf{r}) - \rho_0}{\rho_0}, \tag{3.19}$$

thus the power–expanded excess free energy up to order 4 in ϕ and $\nabla\phi$ reads

$$\begin{aligned} \beta\mathcal{F}_{\mathrm{ex}}[\rho] &= \beta\mathcal{F}_{\mathrm{ex}}[\rho_0] + \beta\mu_{\mathrm{ex}}\rho_0 \int \mathrm{d}\mathbf{r}\, \phi(\mathbf{r}) \\ &\quad + \frac{\rho_0^2}{2} \int \mathrm{d}\mathbf{r}\, \phi(\mathbf{r})(c_0 + c_2\nabla^2 + c_4\nabla^4)\phi(\mathbf{r}). \end{aligned} \tag{3.20}$$

The model defined in Equation (3.20) looks like the square–gradient Ginzburg–Landau models [36] and the usefulness of this model to describe the transition between a homogeneous and a periodically ordered system [37, 38] and phase transitions in amphiphilic [39] systems has been known. The functional in Equation (3.20) has some important characteristics:

1. For $c_2, c_4 > 0$, the term $\propto \phi\nabla^2\phi$ favors a periodically varying ϕ and the term $\propto \phi\nabla^4\phi$ punishes a spatially varying ϕ.

2. Depending on the parameters, it may have as equilibrium states periodically ordered phases in one dimension (stripes), two dimensions (rods) and three dimensions (bcc, fcc, hcp).

3. The characteristic wave number of the order parameter field is $q_0 = \sqrt{c_2/(2c_4)}$ which follow from

$$\phi(\mathbf{r})(c_2\nabla^2 + c_4\nabla^4)\phi(\mathbf{r}) = \phi(\mathbf{r})[-c_4 q_0^4 + c_4(q_0^2 + \nabla^2)^2)]\phi(\mathbf{r}). \tag{3.21}$$

The total free energy contains in addition the ideal gas term, $\mathcal{F}_{\mathrm{id}}[\rho]$ from 3.8. It turns out that the phase diagram of the above model is equivalent to the formulation of a reduced model with the free energy according to [40]

$$\begin{aligned} F_{\mathrm{PFC}} &= \int \mathrm{d}\mathbf{x}\, f_{\mathrm{PFC}} \\ &= \int \mathrm{d}\mathbf{x} \left\{ \frac{1}{2}\Phi(\mathbf{x})[-\epsilon + (1+\nabla^2)^2]\Phi(\mathbf{x}) + \frac{\Phi(\mathbf{x})^4}{4} \right\}, \end{aligned} \tag{3.22}$$

which is called the phase–field crystal (PFC) model.

3.2.5 The Weighted Density Approximation

The theory was presented for the free energy of an inhomogeneous HS fluid by Nordholm *et al.* in 1980 [41], which inspired a whole family of DF approximations. The most successful members of that family had come to share the name of WDA, originally applied in the context of DF theory for the exchange and correlation energy of electronic systems [42]. The common feature of the WDAs for classical fluids is to approximate the local free energy DF by $\Phi_{\mathrm{WDA}}[\rho, \mathbf{r}] = \rho(\mathbf{r})\psi(\bar{\rho}(\mathbf{r}))$, where $\psi(\bar{\rho}(\mathbf{r})) = \Psi(\bar{\rho}_0)/\rho_0$ is the excess free energy per particle of a bulk system with uniform density ρ_0 and $\bar{\rho}(\mathbf{r})$ is a *weighted density* to represent a sampling of the density around point $\mathbf{r}$ through the convolution

$$\bar{\rho}(\mathbf{r}) = \int \mathrm{d}\mathbf{r}'\, \rho(\mathbf{r}+\mathbf{r}')\omega_{\mathrm{WDA}}(r', \bar{\rho}(\mathbf{r})), \tag{3.23}$$

with a normalized weight function $\omega_{\mathrm{WDA}}(r, \rho)$, which may be assumed to depend on the local value of $\bar{\rho}(\mathbf{r})$. The choice of that weight function is the key element of the WDA, because it determines the non–local dependence of $\mathcal{F}_{\mathrm{ex}}[\rho]$. Notice that the LDA is

recovered with a delta–function weight, $\omega_{\rm WDA}(r) = \delta(\mathbf{r})$. The MFA may also be cast into the WDA form by taking the weight function $\omega_{\rm WDA}(r) = u(r)/u_0$, with the pair potential normalized by its total volume integral, u_0, and the linear function $\psi(\rho_0) = u_0\rho_0/2$ for the excess free energy per particle. The use of non–local weights and non–linear functions $\psi(\rho_0)$ made the WDA a very successful DF scheme for HS and other hard–core particles.

The use of more accurate equations of state and the exploration of other analytical forms for $\omega_{\rm WDA}(r)$ paved the road [43] to the crucial element of the WDA: the (density dependent) weight function $\omega_{\rm WDA}(\rho_0, r)$ may be tailored to, through the relation (3.13) to reproduce any given approximation for the direct correlation function of the bulk liquid, so that DF approximations for $\mathcal{F}_{\rm ex}$ may be systematically built, using as ingredients the equation of state and the correlation structure of the HS liquid. The resulting functionals are much more effective than the plain functional Taylor expansion (3.11) built with the same ingredients:

$$\omega_{\rm WDA}(\rho_o, r) = \omega_0(r) + \rho\omega_1(r) + \rho^2\omega_2(r) + \dots . \tag{3.24}$$

3.3 Fundamental Measure Theory of Hard Spheres

In 1989, a new DF approximation for the HS fluid was proposed by Rosenfeld [28, 44] under the name of Fundamental Measure Theory (FMT), and it represented a breaking point in the theory of inhomogeneous hard body systems. FMT is a generalized form of weighted density approximation for fluids consisting of hard particles. In contrast to similar approximations discussed in Section 3.2, the free energy density is taken to be a function not just of one but several different weighted densities, defined by weight functions that emphasis the geometrical characteristics of the particles. The Rosenfeld's original theory was formulated for hard–sphere mixtures [28], but for the sake of simplicity we only consider the one–component case in detail. By the end of the century, it was clear that the generic FMT scheme is quantitatively superior to any WDA although it requires a much more careful design of the functional form and it also has some technical complexities, like the use of vector and tensor weighting functions. This section gives a brief account of the main concepts of the FMT and the most advanced versions, based on the idea of *dimensional crossover*.

3.3.1 Rosenfeld's Original Fundamental Measure Theory

The Rosenfeld theory was motivated in part by the form of the *exact* excess free energy functional for a hard–rod mixture in D = 1 (note that in this section we use capital D for dimensionality rather than lower case d). The other key ingredient to formulate the FMT is the exact low density limit free energy ($\rho \to 0$):

$$\beta\mathcal{F}_{\rm ex}[\rho] = -\frac{1}{2}\int \mathrm{d}\mathbf{r} \int \mathrm{d}\mathbf{r}'\rho(\mathbf{r})\rho(\mathbf{r}')f(r). \tag{3.25}$$

Equation (3.25) retains only the lowest–order term in a virial expansion of the functional (3.11). The next term in the virial expansion contains the product of three Mayer–f bonds. For the particular case of hard spheres

$$\begin{aligned} f(r) &= \begin{cases} -1 & r < 2R \\ 0 & \text{otherwise} \end{cases} \\ &= -\theta(2R - r), \end{aligned} \tag{3.26}$$

where R is the radius of particles, and θ is the Heaviside step function. Rosenfeld showed that the Mayer–f function for hard spheres in 3D can be decomposed as follows [28]

$$f(r) = \omega^3 \otimes \omega^0 + \omega^0 \otimes \omega^3 + \omega^2 \otimes \omega^1 + \omega^1 \otimes \omega^2 - \boldsymbol{\omega}^2 \otimes \boldsymbol{\omega}^1 - \boldsymbol{\omega}^1 \otimes \boldsymbol{\omega}^2, \tag{3.27}$$

where the six weight functions are given by

$$\begin{aligned} \omega^3(\mathbf{r}) &= \theta(R - r)\ , \\ \omega^2(\mathbf{r}) &= \delta(R - r)\ , \\ \omega^1(\mathbf{r}) &= \omega^2(\mathbf{r})/(4\pi R)\ , \\ \omega^0(\mathbf{r}) &= \omega^2(\mathbf{r})/(4\pi R^2)\ , \\ \boldsymbol{\omega}^2(\mathbf{r}) &= \mathbf{r}/r\ \delta(R - r)\ , \\ \boldsymbol{\omega}^1(\mathbf{r}) &= \boldsymbol{\omega}^2/(4\pi R)\ , \end{aligned} \tag{3.28}$$

and the symbol $\otimes$ denots the 3–dimensional convolution of weight functions

$$\omega^\alpha \otimes \omega^\beta(\mathbf{r} = \mathbf{r}_i - \mathbf{r}_j) = \int \mathrm{d}\mathbf{r}'\, \omega^\alpha(\mathbf{r}' - \mathbf{r}_i)\omega^\beta(\mathbf{r}' - \mathbf{r}_j). \tag{3.29}$$

For vector weights, a scalar product is also implied. The convolution can be easily calculated in Fourier space. The deconvolution of the Mayer–f function derived by Rosenfeld is not unique (e.g. see [45]). The ω^α are characteristic functions of a sphere of radius R. This becomes clear on integrating each weight ω^α over space. For $\alpha = 3$ one obtains the Volume $V = 4\pi R^3/3$, for $\alpha = 2$ the surface area $S = 4\pi R^2$, for $\alpha = 1$ the mean radius of curvature R and for $\alpha = 0$ the Euler characteristic which is simply 1. These are the *fundamental* geometric *measures* of the sphere in three dimensions.

Rosenfeld made the following ansatz for the excess free energy functional of the hard spheres

$$\beta\mathcal{F}_{\text{ex}}[\rho] = \int \mathrm{d}\mathbf{r}\, \Phi(n_\alpha(\mathbf{r})), \tag{3.30}$$

where $\beta^{-1}\Phi$, the excess free energy density is a *function* of a set of the weighted densities $n_\alpha(\mathbf{r})$

$$n_\alpha(\mathbf{r}) = \int \mathrm{d}\mathbf{r}'\, \rho(\mathbf{r}')\omega^\alpha(\mathbf{r} - \mathbf{r}'). \tag{3.31}$$

Using dimensional analysis, Rosenfeld assumed that

$$\Phi(n_\alpha) = f_1(n_3)n_0 + f_2(n_3)n_1n_2 + f_3(n_3)\mathbf{n}_1 \cdot \mathbf{n}_2 + f_4(n_3)n_2^3 + f_5(n_3)n_2\mathbf{n}_2 \cdot \mathbf{n}_2, \tag{3.32}$$

where the coefficients f_α depends only on n_3 and each term has dimension $[\text{length}]^{-3}$.

Equations (3.30) and (3.31) must recover the exact low density limit and pair direct correlation function up to first order in density, and this demands that to lowest order in n_3 the f_α must have expansions

$$\begin{aligned} f_1 &= n_3 + \mathcal{O}(n_3^2), \\ f_2 &= 1 + \mathcal{O}(n_3), \\ f_3 &= -1 + \mathcal{O}(n_3), \\ f_4 &= 1/(24\pi) + \mathcal{O}(n_3^2), \\ f_5 &= -3/(24\pi) + \mathcal{O}(n_3^2). \end{aligned}$$

Since $f_3(n_3) = -f_2(n_3)$ and $f_5(n_3) = -3f_4(n_3)$, the free energy density (Equation (3.32)) simplifies to

$$\Phi(n_\alpha) = f_1(n_3)n_0 + f_2(n_3)(n_1 n_2 - \mathbf{n}_1 \cdot \mathbf{n}_2) + f_4(n_3)(n_2^3 - 3n_2 \mathbf{n}_2 \cdot \mathbf{n}_2). \tag{3.33}$$

For intermediate and high densities it is necessary to extrapolate the excess free energy to higher densities. The extrapolation can be performed in various ways. Using Scaled Particle Theory (SPT), Rosenfeld derived FMT for higher densities which resulting functional was not able to predict the freezing transition of hard sphere fluid into a crystalline state. The dimensional crossover approach constructs a functional with new tensorial weighted densities which successfully describes the freezing transition. A third way of extrapolation uses a known equation of state as input and leads to the White Bear (WB) version of FMT [46].

Rosenfeld imposed additional physical requirements (scaled particle theory) in order to determine the coefficients f_α

$$\lim_{R\to\infty} \left(\frac{\mu_{\text{ex}}}{V}\right) = p, \tag{3.34}$$

where $V = 4\pi R^3/3$ is the volume of sphere and p is pressure. This result simply states that the excess chemical potential for inserting a hard–sphere into a uniform fluid at pressure p is pV plus the contribution proportional to the surface area [23]. μ_{ex} can be determined in terms of weighted densities from Equation (3.30)

$$\beta\mu_{\text{ex}} = \frac{\partial\Phi}{\partial\rho} = \sum_\alpha \frac{\partial\Phi}{\partial n_\alpha}\frac{\partial n_\alpha}{\partial\rho}, \tag{3.35}$$

and from the definition of the scaled particle variables $\partial n_3/\partial\rho = 4\pi R^3/3$, $\partial n_2/\partial\rho = 4\pi R^2$, $\partial n_1/\partial\rho = R$ and $\partial n_0/\partial\rho = 1$. Thus

$$\lim_{R\to\infty} \left(\frac{\mu_{\text{ex}}}{V}\right) = \frac{\partial\Phi}{\partial n_3}. \tag{3.36}$$

The pressure is obtained from the thermodynamic relation $\Omega_{\text{bulk}} = -pV$, which is valid for a bulk fluid with the grand potential density given by $\Omega_{\text{bulk}}/V = \beta^{-1}\Phi + f_{\text{id}} - \rho_{\text{bulk}}\mu$. Combining these results and using Equation (3.34) one obtains the scaled particle

differential equation,

$$\frac{\partial \Phi}{\partial n_3} = -\Phi + \sum_\alpha \frac{\partial \Phi}{\partial n_\alpha} n_\alpha + n_0. \tag{3.37}$$

By solving this equation, five coefficients f_α can be determined; integration constants are chosen so that the correct low density limits are recovered. The solution is

$$\begin{aligned} f_1(n_3) &= -\ln(1-n_3), \\ f_2(n_3) &= (1-n_3)^{-1}, \\ f_3(n_3) &= -f_2(n_3), \\ f_4(n_3) &= \left(24\pi(1-n_3)^3\right)^{-1}, \\ f_5(n_3) &= -3f_4(n_3). \end{aligned}$$

The resulting functional is usually written as

$$\Phi = \Phi_1 + \Phi_2 + \Phi_3, \tag{3.38}$$

with

$$\Phi_1 = -n_0 \ln(1-n_3), \qquad \Phi_2 = \frac{n_1 n_2 - \mathbf{n}_1 \cdot \mathbf{n}_2}{1-n_3}, \tag{3.39}$$

$$\Phi_3 = \frac{n_2^3 - 3n_2 \mathbf{n}_2 \cdot \mathbf{n}_2}{24\pi(1-n_3)^2}. \tag{3.40}$$

3.3.2 Dimensional Crossover and the Cavity Theory

The concept of dimensional crossover is a strong test for DF approximations which was first applied [47] to the WDA for HS. The idea is that any DF approximation for the 3D excess free energy of HS, $\mathcal{F}_{\rm ex}$, also contains predictions for any 2D distribution of hard–disks , $\rho_{2D}(x,y)$, because the latter should be fully equivalent to a 3D distribution with a delta function along the z–axis: $\rho_{\rm 3D}(x,y,z) = \rho_{\rm 2D}(x,y)\delta(z)$; see Figure 3.1. The dimensional crossover may be extended to represent 1D distributions of hard–rods as 3D distributions, with $\rho_{\rm 3D}(x,y,z) = \rho_{\rm 1D}(x)\delta(y)\delta(z)$, and the equivalent reduction from 2D to 1D can also be defined. It has been shown that the DF reduction of the FMT

from 3D to 2D is very accurate; however, the reduction from 3D to 1D was a complete failure, since the third term Φ_3 in Equation (3.40) diverges [24].

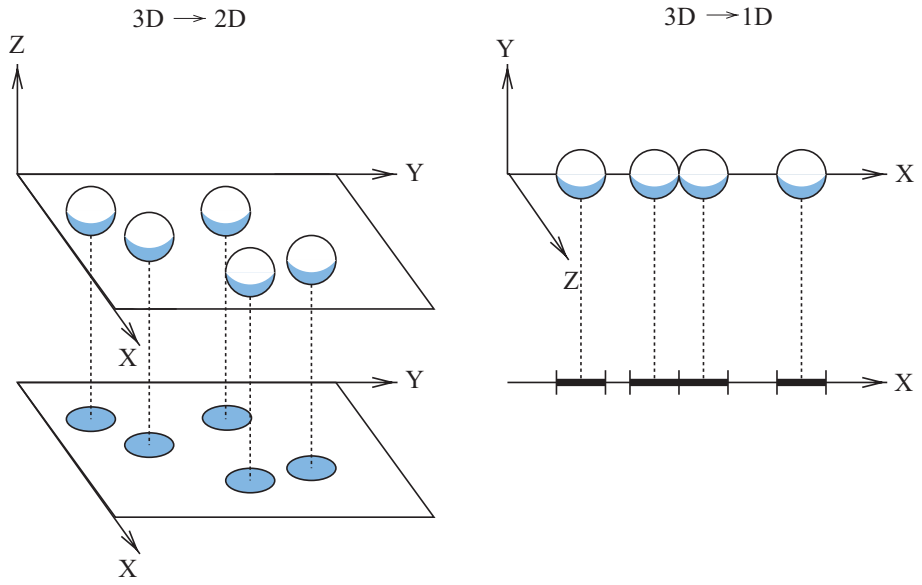

FIGURE 3.1: Dimensional crossover within the DF formalism. On the left, a 3D distribution with the hard sphere centers located on the $z = 0$ plane $\rho_{3D}(x, y, z) = \rho_{2D}(x, y)\delta(z)$ is fully equivalent to a 2D distribution of hard disks $\rho_{3D}(x, y, z) = \rho_{1D}(x)\delta(y)\delta(z)$. On the right, a 3D distribution with all the HS centers along the x–axis is fully equivalent to a system of 1D hard rods [24].

The concept of the zero–dimensional (0D) limit which leads to the *cavity theory* was proposed by Tarazona and Rosenfeld [48] to treat this failure. Consider a small cavity which can not hold more than one hard–core particle which is connected to a particle reservoir at chemical potential μ. This cavity may be considered as the zero–dimensional (0D) limit of hard sphere fluid. From any free energy functional, $\mathcal{F}[\rho(\mathbf{r})]$, for a 3D system we may get the free energy of a 2D system considering the fluid inside a very narrow slit pore. The one–dimensional free energy may be obtained from a fluid in a very narrow cylindrical capillary, and the very narrow cavity should provide the ultimate dimensional crossover to the 0D excess free energy which is a simple function of the mean occupation number N [49],

$$F_{\text{ex}}^{\text{0D}} = (1 - N)\ln(1 - N) + N. \tag{3.41}$$

The interesting property of the 0D limit is that its free energy does not depend on the shape of the cavity (i.e. the confining potential) (see Figure 3.2).

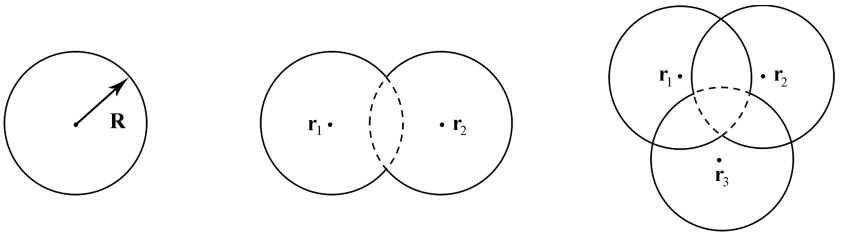

FIGURE 3.2: Three types of cavities which can hold only one particle.

Any of the reduced dimension systems are extremely inhomogeneous, from the 3D point of view, therefore a good description of the dimensional crossover requires a very good density functional approximation, by taking into account the non–local dependence of the free energy on the density distribution. The requirement that $\mathcal{F}[\rho(\mathbf{r})]$ should give the exact 0D limit is strong enough to determine the functional dependence within the FMT class.

Tarazona introduced a new tensorial weight function using arguments presented above [50]

$$\omega_{ij}^{t} = \frac{r_i r_j}{\mathbf{r}^2}\delta(R-r), \tag{3.42}$$

which is added to the third term of the free energy density (3.40). The resulting free energy density term is

$$\Phi_3 = \frac{3(-n_2\mathbf{n}_2\cdot\mathbf{n}_2 + n_{2,i}n_{t,ij}n_{2,j} + n_2 n_{t,ij}n_{t,ji} - n_{t,ij}n_{t,jk}n_{t,ki})}{16\pi(1-n_3)^2}. \tag{3.43}$$

Using Equations (3.39) and (3.43) the excess free energy functional can be written as follows

$$\Phi(\mathbf{n}[\rho(\mathbf{r})]) = \Phi_1 + \varphi_1(n_3)\Phi_2 + \varphi_2(n_3)\Phi_3. \tag{3.44}$$

Here, $\varphi_1(n_3)$ and $\varphi_2(n_3)$ are functions of the local packing density $n_3(\mathbf{r})$. By choosing

$$\varphi_1 = 1 \quad \text{and} \quad \varphi_2 = 1, \tag{3.45}$$

we obtain Tarazona's tensorial functional [50] based on the original Rosenfeld functional [28]. The choice

$$\begin{aligned} \varphi_1 &= 1, \\ \varphi_2 &= 1 - \frac{-2n_3 + 3n_3^2 - 2(1-n_3)^2 \ln(1-n_3)}{3n_3^2}, \end{aligned} \tag{3.46}$$

corresponds to the tensor version of the White Bear I functional [51]. Finally, with

$$\begin{aligned} \varphi_1 &= 1 + \frac{2n_3 - n_3^2 + 2(1-n_3)\ln(1-n_3)}{3n_3^2}, \\ \varphi_2 &= 1 - \frac{2n_3 - 3n_3^2 + 2n_3^3 + 2(1-n_3)^2 \ln(1-n_3)}{3n_3^2}, \end{aligned} \tag{3.47}$$

the tensor version of the white Bear II functional is recovered [52]. This functional is most consistent with respect to restrictions imposed by morphological thermodynamics [53].

3.4 Stillinger's Expansion in Correlated, Contiguous Particles

Classical density functional theory is a theoretical framework, which has been extensively employed to study inhomogeneous complex fluids (CF), solids and solid–liquid phase transition phenomena. On the other hand, computer simulation is one the most useful approaches to the analytical theory of the classical many–body problem which is based on finding the partition function of the system under study. Stillinger's approach is a technique which was developed for estimating the partition function near close packing, by evaluating the free–energy contribution from the correlated motion of larger and larger sets of contiguous particles. Stillinger's expansion provides the analytical theory on the high–density thermodynamic properties which is not very known unlike the low–density limit. Consider the canonical partition function for N hard spheres

$$Q(N,V,T) = \frac{1}{N!\Lambda^{3N}} \int d\mathbf{r}_1 \ldots \int d\mathbf{r}_n \prod_{i,j\,(i<j)}^{N} \phi(ij)\,, \tag{3.48}$$

$$\phi(ij) = \begin{cases} 0 & (r_{ij} \le \sigma) \\ 1 & (r_{ij} > \sigma) \end{cases}. \tag{3.49}$$

Here, $r_{ij} = |\mathbf{r}_i - \mathbf{r}_j|$ is the center distance between particles i and j. We consider a reference lattice of our choice (fcc, hcp or bcc) with $M \geq N$ lattice sites at positions $\mathbf{s}_i$ spanning the volume V. We associate each particle i with a lattice site at site $\mathbf{s}_i$ and that association divides the $3N$ dimensional configuration space into nonoverlapping regions $\Omega_{l,p}$. The precise form of this association is discussed in Ref. [54], but one may think of it loosely in terms of each particle i belonging to the Voronoi cell around site $\mathbf{s}_i$ of the lattice. For a chosen subset of N lattice sites $\{\mathbf{s}_i\}$ and associated cells, the index p runs over the $N!$ permutations of the particles among these cells and this leads to an identical division of the configuration space, $\Omega_{l,p_1} \equiv \Omega_{l,p_2}$. The index l runs over the different associations of N particles with $M > N$ lattice sites and becomes important in the case of finite vacancy concentration. Thus we obtain for the partition function:

$$Q(N,V,T) = \frac{1}{\Lambda^{3N}} \sum_l \int \dots \int_{\Omega_{l,1}} d\mathbf{r}_1 \dots d\mathbf{r}_N \prod_{i<j} \phi(ij) \,. \tag{3.50}$$

For zero vacancy concentration, this decomposition is akin to the SOC method (as e.g. discussed in Ref. [55]) where each particle is confined to its Wigner–Seitz cell. Following Ref. [54], one may write Q in terms of configuration integrals Z_i^l, Z_{ij}^l, ... which describe the correlated motion of one, two, ... particles in a background matrix of $N-1$, $N-2$, ... particles fixed at their associated lattice sites. These configuration integrals are defined as

$$Z_i^l = \int_{\omega_i^l} d\mathbf{r}_i \prod_{j\neq i}^{N} \phi(ij) \qquad \text{with} \tag{3.51}$$
$$\mathbf{r}_j = \mathbf{s}_j \quad (j \neq i) \,,$$
$$Z_{ij}^l = \int_{\omega_{ij}^l} d\mathbf{r}_i d\mathbf{r}_j \prod_{k\neq i,j}^{N} \phi(ik)\phi(jk) \qquad \text{with} \tag{3.52}$$
$$\mathbf{r}_k = \mathbf{s}_k \quad (k \neq i,j) \,,$$
$$\vdots \quad .$$

The integration domains must fulfill $\omega_i^l, \omega_{ij}^l, \dots \in \Omega_{l,1}$, and they depend on the indices of the free particles i, j and also in the index l determining at which lattice sites the

other particles are fixed. The partition function is now expressed as the product

$$Q(N,V,T) = \frac{1}{\Lambda^{3N}} \sum_l \prod_i^N Z_i^l \prod_{i<j}^N \frac{Z_{ij}^l}{Z_i^l Z_j^l} \prod_{i<j<k}^N \frac{Z_{ijk}^l Z_i^l Z_j^l Z_k^l}{Z_{ij}^l Z_{ik}^l Z_{jk}^l} \dots \tag{3.53}$$

$$=: \frac{1}{\Lambda^{3N}} \prod_i^N Y_i^l \prod_{i<j} Y_{ij}^l \prod_{i<j<k}^N Y_{ijk}^l \dots \,. \tag{3.54}$$

The Y's can also be expressed by the recursive relation

$$Y_{1\dots n}^l = \frac{Z_{1\dots n}^l}{\prod_{\text{subsets}} Y_{i_1\dots i_m}^l} \,, \tag{3.55}$$

where $\{i_1 \dots i_m\}$ is any proper subset of $\{1 \dots n\}$. For example, when omitting indices we have $Y_2 = Z_2/(Y_1 Y_2)$ and $Y_3 = Z_3/(Y_1 Y_2 Y_3\, Y_{12} Y_{13} Y_{23})$.

3.5 Dynamical Density Functional Theory

To study fluid dynamical phenomena, it is often sufficient to consider the fluid as a continuum and ignore the fact that it is in reality made up of individual particles. Over the last decade the dynamical density functional theory (DDFT) has been developed. This constitutes a microscopic theory for fluid dynamics of such colloidal fluid. The starting point was work by Marconi and Tarazona [56, 57], in which they assumed that the colloids can be modeled as Brownian particles with stochastic equation of motion, thus neglecting hydrodynamic interactions between the colloids. The Smoluchowski equation for N Brownian particles is

$$\frac{\partial W(\mathbf{r}^N, t)}{\partial t} = \Gamma \sum_{i=1}^N \nabla_i \cdot (k_B T \nabla_i + \nabla_i U_{\text{tot}})\, W(\mathbf{r}^N, t), \tag{3.56}$$

where $\mathbf{r}^N = (\mathbf{r}_1, \dots, \mathbf{r}_N)$ is the particle positions, t denotes the time and Γ is the mobility which is connected to the diffusion coefficient through the Einstein relation, $\Gamma = D/k_B T$. $W(\mathbf{r}^N, t)$ is the time–dependent probability distribution function. ∇_i denotes the nabla operator $\nabla = \hat{\mathbf{e}}_x \frac{\partial}{\partial x} + \hat{\mathbf{e}}_y \frac{\partial}{\partial y} + \hat{\mathbf{e}}_z \frac{\partial}{\partial z}$ which operates on the ith particle. The total potential energy U_{tot} has the form

$$U_{\text{tot}} = \sum_{i=1}^N V_{\text{ext}}(\mathbf{r}^N, t) + \sum_{\substack{i=1 \\ i<j}}^N V_N(|\mathbf{r}_i - \mathbf{r}_j|), \tag{3.57}$$

here, V_{ext} is the external potential and the internal potential V_N, contains all the inter–particle interactions. Now the idea is to integrate out degrees of freedom. Integrating the probability density distribution over all particle positions but one leads to the one–body density

$$\rho^{(1)}(\mathbf{r}_1,\, t) = N \int \mathrm{d}\mathbf{r}_2 \,\ldots \int \mathrm{d}\mathbf{r}_N \, W(\mathbf{r}^N,\, t), \tag{3.58}$$

or more generally, for n–particle density we have

$$\rho^{(n)}(\mathbf{r}_1,\, \ldots,\, \mathbf{r}_n,\, t) = \frac{N!}{(N-n)!} \int \mathrm{d}\mathbf{r}_{n+1} \,\ldots \int \mathrm{d}\mathbf{r}_N \, W(\mathbf{r}^N,\, t). \tag{3.59}$$

Integrating the Smoluchowski equation for one–body density yields

$$\begin{aligned} \frac{1}{\Gamma}\frac{\partial \rho^{(1)}(\mathbf{r}_1,t)}{\partial t} \quad = \quad & N \int \mathrm{d}\mathbf{r}_2 \,\ldots \int \mathrm{d}\mathbf{r}_N \left\{ \sum_{i=1}^{N} \left(k_B T \nabla_i^2 W(\mathbf{r}^N,t) \right.\right. \\ & + \nabla_i \left(\nabla_i V_{\text{ext}}(\mathbf{r}_i,t) W(\mathbf{r}^N,t) \right) \Big) \\ & \left. \left. + \sum_{\substack{i=1 \\ i<j}}^{N} \nabla_i \left(\nabla_i \left(V_N(|\mathbf{r}_i - \mathbf{r}_j|) W(\mathbf{r}^N,t) \right) \right) \right\}. \end{aligned} \tag{3.60}$$

The integral can be split into three terms:

1. **First term:**

$$\begin{aligned} N \int \mathrm{d}\mathbf{r}_2 \,\ldots \int \mathrm{d}\mathbf{r}_N \sum_{i=1}^{N} k_B T \nabla_i^2 W(\mathbf{r}^N,t) &= k_B T \nabla_1^2 \rho^{(1)}(\mathbf{r}_1,t) \\ &+ N \int \mathrm{d}\mathbf{r}_2 \,\ldots \int \mathrm{d}\mathbf{r}_N \, k_B T \sum_{i=2}^{N} \nabla_i^2 W(\mathbf{r}^N,t) \\ &= k_B T \nabla_1^2 \rho^{(1)}(\mathbf{r}_1,t) \\ &+ \sum_{i=2}^{N} N k_B T \int \mathrm{d}\mathbf{r}_i \nabla_i \underbrace{\left(\nabla_i \int \mathrm{d}\mathbf{r}_2 \ldots \int \mathrm{d}\mathbf{r}_N W(\mathbf{r}^N,t) \right)}_{g(\mathbf{r}_1,\mathbf{r}_i,t)} \end{aligned}$$

$$= k_B T \nabla_1^2 \rho^{(1)}(\mathbf{r},t) + \sum_{i=2}^{N} N k_B T \underbrace{\int \mathrm{d}\mathbf{r}_i \nabla_i g(\mathbf{r}_1,\mathbf{r}_i,t)}_{=0}, \tag{3.61}$$

since W decays to zero for large distances.

2. **Second term:**

$$
\begin{aligned}
N \int \mathrm{d}\mathbf{r}_2 \ldots \int \mathrm{d}\mathbf{r}_N \sum_{i=1}^{N} \nabla_i \left(\nabla_i V_{\mathrm{ext}}(\mathbf{r}_i, t) W(\mathbf{r}^N, t) \right) \\
&= N \int \mathrm{d}\mathbf{r}_2 \ldots \int \mathrm{d}\mathbf{r}_N \nabla_1 \left(\nabla_1 V_{\mathrm{ext}}(\mathbf{r}_1, t) \right) W(\mathbf{r}^N, t) + 0 \\
&= \nabla_1 \left(\rho^{(1)}(\mathbf{r}_1, t) \nabla_1 V_{\mathrm{ext}}(\mathbf{r}_1, t) \right). \qquad (3.62)
\end{aligned}
$$

3. **Third term:**

$$
\begin{aligned}
N \int \mathrm{d}\mathbf{r}_2 \ldots \int \mathrm{d}\mathbf{r}_N \sum_{\substack{i=1 \\ i<j}}^{N} \nabla_i \cdot \left(\nabla_i V_N(|\mathbf{r}_i - \mathbf{r}_j|) \right) W(\mathbf{r}^N, t) \\
&= N \int \mathrm{d}\mathbf{r}_2 \ldots \int \mathrm{d}\mathbf{r}_N \nabla_1 \left(\sum_{j=2}^{N} \nabla_1 V_N(|\mathbf{r}_1 - \mathbf{r}_j|) W(\mathbf{r}^N, t) \right) \\
&\qquad \mathbf{r}^N \text{is symmetric in coordinate, set j=2} \\
&= N(N-1) \nabla_1 \int \mathrm{d}\mathbf{r}_2 \nabla_1 V_N(|\mathbf{r}_1 - \mathbf{r}_2|) \int \mathrm{d}\mathbf{r}_3 \ldots \int \mathrm{d}\mathbf{r}_N W(\mathbf{r}^N, t) \\
&= \int \mathrm{d}\mathbf{r}_2 \nabla_1 \left(\nabla_1 V_N(|\mathbf{r}_1 - \mathbf{r}_2|) \right) \rho^{(2)}(\mathbf{r}_1, \mathbf{r}_2, t). \qquad (3.63)
\end{aligned}
$$

Hence in total we have

$$
\begin{aligned}
\frac{1}{\Gamma} \frac{\partial \rho^{(1)}(\mathbf{r}_1, t)}{\partial t} &= k_B T \nabla_1^2 \rho^{(1)}(\mathbf{r}_1, t) + \nabla_1 \left(\rho^{(1)}(\mathbf{r}_1, t) \nabla_1 V_{\mathrm{ext}}(\mathbf{r}_1, t) \right) \\
&\quad + \nabla_1 \int \mathrm{d}\mathbf{r}_2 \, \rho^{(2)}(\mathbf{r}_1, \mathbf{r}_2, t) \nabla_1 V_N(|\mathbf{r}_1 - \mathbf{r}_2|). \qquad (3.64)
\end{aligned}
$$

In equilibrium

$$
\frac{\partial \rho^{(1)}(\mathbf{r}_1, t)}{\partial t} = 0, \qquad (3.65)
$$

which implies

$$
\begin{aligned}
\nabla \left(k_B T \nabla \rho(\mathbf{r}, t) + \rho(\mathbf{r}, t) \nabla V_{\mathrm{ext}}(\mathbf{r}, t) + \int \mathrm{d}\mathbf{r}' \, \rho^{(2)}(\mathbf{r}, \mathbf{r}', t) \nabla V_N(|\mathbf{r} - \mathbf{r}'|) \right) \\
&= \nabla \left(k_B T \nabla \rho(\mathbf{r}) + \rho(\mathbf{r}) \nabla V_{\mathrm{ext}}(\mathbf{r}) + \int \mathrm{d}\mathbf{r}' \, \rho^{(2)}(\mathbf{r}, \mathbf{r}') \nabla V_N(|\mathbf{r} - \mathbf{r}'|) \right) \\
&= 0. \qquad (3.66)
\end{aligned}
$$

The sum of the terms inside the parentheses should be constant and this constant must vanish for $r \longrightarrow \infty$ and is thus identical to zero. Therefore

$$k_B T \nabla \rho(\mathbf{r}) + \rho(\mathbf{r}) \nabla V_{\text{ext}}(\mathbf{r}) + \int \mathrm{d}\mathbf{r}' \; \rho^{(2)}(\mathbf{r}, \mathbf{r}') \nabla V_N(|\mathbf{r} - \mathbf{r}'|) = 0. \tag{3.67}$$

This is also known as Yvon–Born–Green hierarchy (YBG).

In equilibrium, DFT implies

$$\frac{\delta \mathcal{F}_{\text{ex}}}{\delta \rho(\mathbf{r})} + k_B T \ln(\Lambda^3 \rho(\mathbf{r})) - \mu + V_{\text{ext}}(\mathbf{r}) = 0. \tag{3.68}$$

By applying gradient operator to the above Euler–Lagrange equation we obtain

$$\nabla V_{\text{ext}} + k_B T \underbrace{\nabla \ln(\Lambda^3 \rho(\mathbf{r}))}_{\frac{\nabla \rho(\mathbf{r})}{\rho(\mathbf{r})}} + \nabla \frac{\delta \mathcal{F}_{\text{ex}}}{\delta \rho(\mathbf{r})} = 0, \tag{3.69}$$

which in combination with YBG reads

$$\int \mathrm{d}\mathbf{r}' \; \rho^{(2)}(\mathbf{r}, \mathbf{r}') \nabla V_N(|\mathbf{r} - \mathbf{r}'|) = \rho(\mathbf{r}) \nabla \frac{\delta \mathcal{F}_{\text{ex}}}{\delta \rho(\mathbf{r})}. \tag{3.70}$$

Using Equations (3.64), (3.67) and (3.70) we have

$$\begin{aligned} \frac{\partial \rho(\mathbf{r}, t)}{\partial t} = \Gamma \nabla (& k_B T \nabla \rho(\mathbf{r}, t) + \rho(\mathbf{r}, t) \nabla V_{\text{ext}}(\mathbf{r}, t) \\ & + \rho(\mathbf{r}, t) \nabla \frac{\delta \mathcal{F}_{\text{ex}}}{\delta \rho(\mathbf{r})}), \end{aligned} \tag{3.71}$$

or equivalently

$$\frac{\partial \rho(\mathbf{r}, t)}{\partial t} = D \nabla \left(\rho(\mathbf{r}, t) \nabla \frac{\delta \beta \mathcal{F}[\rho]}{\delta \rho(\mathbf{r}, t)} \right), \tag{3.72}$$

which presents the equation of dynamical density functional theory (DDFT). In the case of the ideal gas ($\mathcal{F}_{\text{ex}} = 0$) and in the absence of any external potential ($V_{\text{ext}} = 0$), Equation (3.72) reduces to the diffusion equation (heat equation)

$$\frac{\partial \rho(\mathbf{r}, t)}{\partial t} = D \nabla^2 \rho(\mathbf{r}, t). \tag{3.73}$$

Chapter 4

Stable and Metastable Hard Sphere Crystals

This chapter deals with the applications of the density functional theory (DFT) of fundamental measure type (FMT) to study the most common crystal lattice structures with hard cores of face–centered cubic (fcc), hexagonally close–packed (hcp) and body–centered cubic (bcc). Using DFT, density distributions, free energies and equilibrium vacancy concentrations of these structures are studied and by comparing DFT results with simulation data and Stillinger's approach of correlated movement of free particles, the stability of fcc over hcp is described. Besides, the metastability of hard sphere bcc crystal structure is explained.

4.1 Introduction

The crystal lattices of monatomic substances are very often of face–centered cubic (fcc), hexagonally close–packed (hcp) or body–centered cubic (bcc) type. Still, it is a formidable problem in statistical mechanics and quantum chemistry to predict the stable crystal structure and its free energy for a given substance. Approximating the particle interactions in this substance by classical two–body potentials makes the problem amenable to a treatment using methods of classical statistical mechanics, most notably Monte Carlo (MC) simulations and (classical) density functional theory (DFT). While the approximation using two–body potentials may not be very accurate for truly

atomic substances, the advance in colloid synthesis allows to realize systems with simple two–body potentials to a good degree of approximation, thus colloid suspensions are a perfect model system for investigating freezing in classical statistical mechanics.

For isotropic two–body potentials $u(r)$ (r is the center distance between two particles) a substantial amount of knowledge has been gathered. For potentials with a repulsive core, the steepness of the core mainly determines the stability of fcc over bcc, with fcc being more stable for steeper cores. This has been investigated for power–law potentials $u \propto (1/r)^n$ [58] and screened exponentials $u \propto \exp(-\kappa r)/r$ [59, 60] where the parameters n and κ determine the steepness of the potential. In the hard–sphere limit ($n, \kappa \to \infty$), fcc appears to be the stable, equilibrium structure and a possible bcc structure is unstable against small shear [61] which is reflected in squared phonon frequencies $\omega^2(\mathbf{k})$ being negative for certain wave vectors $\mathbf{k}$.

For hard spheres, it is a much more delicate issue whether fcc is more stable than other close–packing structures, most notably hcp. Early theoretical work by Stillinger *et al.* analyzed the free energy of hard disks and fcc and hcp hard sphere crystals in terms of an expansion in the number n of contiguous particles (free to move) in an otherwise frozen matrix of particles at their ideal lattice positions [62–64]. Stillinger's approach confirms simulation data [55, 65] of the stability of fcc over hcp and it appears to be very hard to contribute the theoretical understanding of the stability of fcc over hcp beyond the Stillinger arguments and in this respect density functional theory (DFT) seems to be the only promising candidate theory.

4.2 Theory

4.2.1 Fundamental Measure Theory

In the framework of density functional theory, the crystal is viewed as a self–sustained inhomogeneous fluid. An inhomogeneous density profile $\rho_{cr}(\mathbf{r})$ minimizes the grand canonical free energy functional of the one–body density profile $\rho(\mathbf{r})$ (3.1)

$$\Omega[\rho(\mathbf{r})] = \mathcal{F}_{\mathrm{id}}[\rho(\mathbf{r})] + \mathcal{F}_{\mathrm{ex}}[\rho(\mathbf{r})] + \int d\mathbf{r}\rho(\mathbf{r})[V_{\mathrm{ext}}(\mathbf{r}) - \mu]\,. \tag{4.1}$$

Fundamental measure theory (FMT) provides the most precise functional for the excess free energy part (Section 3.3). In this thesis we mostly use Tarazona, White Bear I and White Bear II tensorial functionals. The last one is the most consistent with respect to restrictions imposed by morphological thermodynamics [53]. In density functional approach, besides bulk and inhomogeneous fluids, it is possible to study properties of the hard–sphere crystal within the framework of FMT. Using the variational principle, the equilibrium density profile $\rho_{\mathrm{eq}}(\mathbf{r})$ is determined via minimizing the grand canonical free energy functional (Equation (3.2)) which leads to the Euler-Lagrange equation:

$$\beta^{-1} \ln \frac{\rho_{\mathrm{eq}}(\mathbf{r})}{\rho_0} = -\frac{\delta \mathcal{F}_{\mathrm{ex}}[\rho(\mathbf{r})]}{\delta \rho(\mathbf{r})} + \mu_{\mathrm{ex}} - V_{\mathrm{ext}}(\mathbf{r}) \; . \tag{4.2}$$

For the equilibrium crystal, $V^{\mathrm{ext}}(\mathbf{r}) = 0$ and $\rho_{\mathrm{eq}}(\mathbf{r})$ is lattice–periodic, and the homogeneous density (bulk density), ρ_0, is fixed by the excess chemical potential μ^{ex}. Being computationally simpler than a free minimization of the density profile, crystal density profiles are often obtained by a constrained minimization of a model profile with only a few free parameters such as e.g. a Gaussian profile

$$\rho_{\mathrm{cr}}(\mathbf{r}) = \sum_{\text{lattice sites } i} (1 - n_{\mathrm{vac}}) \left(\frac{\alpha}{\pi}\right)^{3/2} \exp\left(-\alpha(\mathbf{r} - \mathbf{r}_i)^2\right) . \tag{4.3}$$

Here, the free parameters are the Gaussian peak width α and the vacancy concentration n_{vac}.

4.2.1.1 Choice of Unit Cells for the Numerical Solution of Euler–Lagrange Equation

Face–centered cubic (fcc) and hexagonal close–packed (hcp) are two regular lattices with the highest possible hard–sphere packing fraction ($\eta \approx 0.74$). The body centered cubic (bcc) structure can attain only packing fractions up to $\eta \approx 0.68$. The fcc and hcp structures differ in how sheets of hexagonally packed hard spheres are stacked upon one another. Relative to a reference layer A (see Fig. 4.1), two other layer types B and C are possible which are laterally shifted with respect to A. In the fcc structure the stacking of the hexagonally–packed planes corresponds to the crystallographic [111] direction and every third layer is the same (ABCABCA) whereas in the hcp lattice ([001] direction), the sequence of A and B repeats (ABABABA) (Fig. 4.1). If the binding energy (or

free energy) were dependent only on the number of nearest–neighbor bonds per atom (bonds have no direction), there would be no energetic difference between the fcc and hcp structures.

The most convenient unit cell for fcc is the cubic unit cell with 8 particles at the corners and 6 face–centered particles (this cell, however, lies oblique in the ABCABCA packing discussed above). For hcp it is the unit cell with hexagonally packed hard spheres on the basal plane. In order to avoid any numerical errors in the comparison between fcc and hcp, we define two extended unit cells of the same size with hexagonally packed spheres as the base plane (see Figure 4.1). The fcc layers cycle among the three identical, but laterally shifted layers, the blue A layer, the red B layer and the green C layer. For hcp, the A and B layers alternate. Positions of the lattice points of the first layers from the bottom are

$$
\begin{aligned}
\text{layer A} \quad &: \quad (0,0,0),\ (a,0,0),\ (0,\sqrt{3}\,a,0),\ (a,\sqrt{3}\,a,0),\ (\frac{1}{2}\,a,\frac{\sqrt{3}}{2}\,a,0),\\
\text{layer B} \quad &: \quad (0,\frac{1}{\sqrt{3}}\,a,\frac{1}{2}\,c),\ (a,\frac{1}{\sqrt{3}}\,a,\frac{1}{2}\,c),\ (\frac{1}{2}\,a,\frac{5}{2\sqrt{3}}\,a,\frac{1}{2}\,c),\\
\text{layer C} \quad &: \quad (\frac{1}{2}\,a,\frac{1}{2\sqrt{3}}\,a,c),\ (0,\frac{2}{\sqrt{3}}\,a,c),\ (a,\frac{2}{\sqrt{3}}\,a,c),
\end{aligned}
$$

here a is the nearest neighbor distance in the basal plane and $c/2$ is the distance between two neighboring layers. Discretization of the extended unit cells by the same number of equal–distant grid–points ensures that the lattice points in layer A are on grid points and for layers B and C the lattice points are equally "off–grid" since there is a mirror reflection symmetry with respect to the x–axis between B and C. In view of the narrow density peaks centered around each lattice point, this choice eliminates numerical differences between fcc and hcp free energies to a large extent. In Fig. 4.1, a is the nearest neighbour distance, and in the close–packed case $a = \sigma$. The fcc cubic symmetry requires $c = \sqrt{8/3}\,a$ which entails that the distance between nearest neighbour within a base plane is the same as between neighbouring planes. For hcp, the hexagonal symmetry group does not enforce this constraint, for a discussion of the implications thereof see Sec. 4.3.3 below.

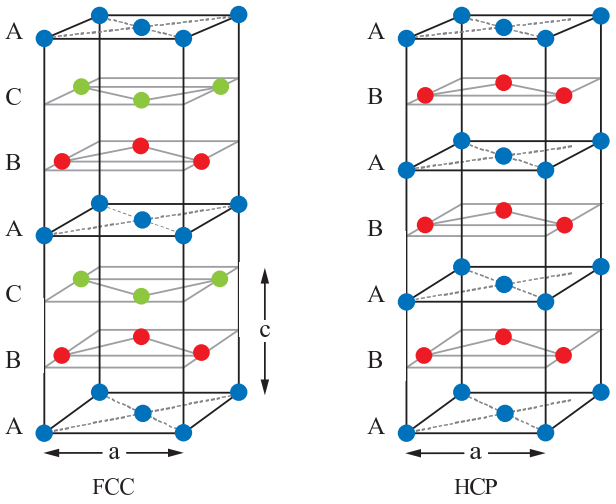

FIGURE 4.1: Extended unit cells for the fcc and hcp crystal structures which are used in DFT calculations to avoid any possible numerical errors due to the discretization. Here a is nearest neighbor distance in the basal plane and $c/2$ is the distance between two neighboring layers.

4.2.1.2 Free Minimization

Equilibrium crystal density profile $\rho_{\text{eq}}(\mathbf{r}; \rho_0, n_{\text{vac}})$ is determined by a full minimization in three–dimensional real space. Finding density profile using numerical methods needs to discretize the density $\rho(\mathbf{r})$ over the cuboid volume with edge lengths $L_x = L_y = L_z = a$ for bcc (using the cubic unit cell) and $L_x = a$, $L_y = \sqrt{3}\,a$ and $L_z = 3c$ for both fcc and hcp (using the extended unit cells of Fig. 4.1) with periodic boundary conditions.

We perform a double step minimization of the free energy. In the first step, the bulk density ρ_0 and the vacancy concentration n_{vac} are fixed and the Euler–Lagrange equation (4.2) is solved iteratively with a start profile given by the Gaussian profile (4.3) with optimal width. The excess chemical potential μ_{ex} in Eq. (4.2) is treated as a Lagrange multiplier to ensure the constraint of fixed n_{vac}. In the next step, this procedure is repeated for different n_{vac} (still keeping ρ_0 fixed), and the equilibrium density profile is determined by minimizing the free energy per particle with respect to the the vacancy concentration, n_{vac}. For a more detailed discussion of this procedure see Ref. [66].

In the program, 11 weighted densities (two scalar densities n_3, n_2, three vector densities, $\mathbf{n}_{2,i}$, $i = x, y, z$, and six tensor densities, n^t_{ij}) as well as the density profile $\rho(\mathbf{r})$ are discretized on a three dimensional grid covering the cuboid boxes. Usually grids for the

bcc unit cell are chosen with $64 \times 64 \times 64$ points in the x, y and z directions, respectively, and $128 \times 128 \times 384$ points for the fcc and hcp extended unit cells. The approach for calculating the weighted densities is discussed in detail in Appendix B.

There are many sophisticated algorithms for minimizing a function and likewise many techniques to increase the speed and efficiency of the process. To have a more efficient algorithm, the iteration of Eq. (4.2) was done using a combination of Picard steps and DIIS steps (Discrete Inversion in Iterative Subspace) (see Appendix C). In order to prevent the procedure from diverging during the Picard iterations, we mix the new density with the old one in each step

$$\rho_{\text{new}} = (1 - \alpha)\rho_{\text{old}} + \alpha\rho_{\text{new}} \; . \tag{4.4}$$

Here, α is a mixing parameter and is usually a small number. For the case of bcc, α can be adapted in the course of the iterations in the range of $\alpha = 10^{-5} \ldots 10^{-3}$. For fcc and hcp, a constant value for α stabilizes the iterations, with values $\alpha = 10^{-5} \ldots 10^{-4}$. A typical FMT run consisted of an initial Picard sequence with about 30 steps. Then we alternated between Picard sequence of 7 steps and a DIIS step (which needs another n_{DIIS} Picard initialization steps), see also Ref. [67].

4.2.2 Stillinger's Expansion up to $n = 2$ for hcp, fcc and bcc Hard Spheres

Early theoretical work work by Stillinger *et al.* analyzed the free energy of hard disks and hard sphere crystals in terms of an expansion in the number n of contiguous particles (free to move) in an otherwise frozen matrix of particles at their ideal lattice positions (Section 3.4). This expansion could be done analytically only for densities in the vicinities of close–packing and, for $n = 2$ and $n = 3$ (by quite a *tour de force*). In the following, we restrict calculations to the case $N = M$ (number of particles equal to number of lattice sites M), i.e. consider a vacancy–free crystal and expand the free energy up to the order $n = 2$. From simulations [68] and FMT [66] we can estimate that the effect of vacancies on the free energy of the crystal is small: for fcc hard spheres we have $n_{\text{vac}} \sim 10^{-4}$ (simulations) and $n_{\text{vac}} \sim 10^{-5}$ (FMT) in equilibrium at coexistence, the corresponding free energy shift compared to $n_{\text{vac}} \to 0$ can be estimated from FMT, $\Delta F/N \sim 10^{-5}\ k_{\text{B}}T$.

Truncated after the first term, the Stillinger series (3.54) is

$$Q_1 = \frac{1}{\Lambda^{3N}}(V_1)^N , \tag{4.5}$$

where Z_1^l has been reduced to V_1, the free volume for one particle in a cage of fixed neighbors at their lattice sites. The shape of the one–particle free volume of hard disks and hard spheres for different crystal structures are sketched in Fig. 4.2. Consequently the free energy is

$$\beta F_1 = -N \ln \frac{V_1}{\Lambda^3} . \tag{4.6}$$

For fcc and hcp, V_1 is equal and has been calculated analytically in Ref. [69], we quote this result in Appendix D. For bcc, we did not find a literature result and therefore give the calculation and result also in Appendix D.

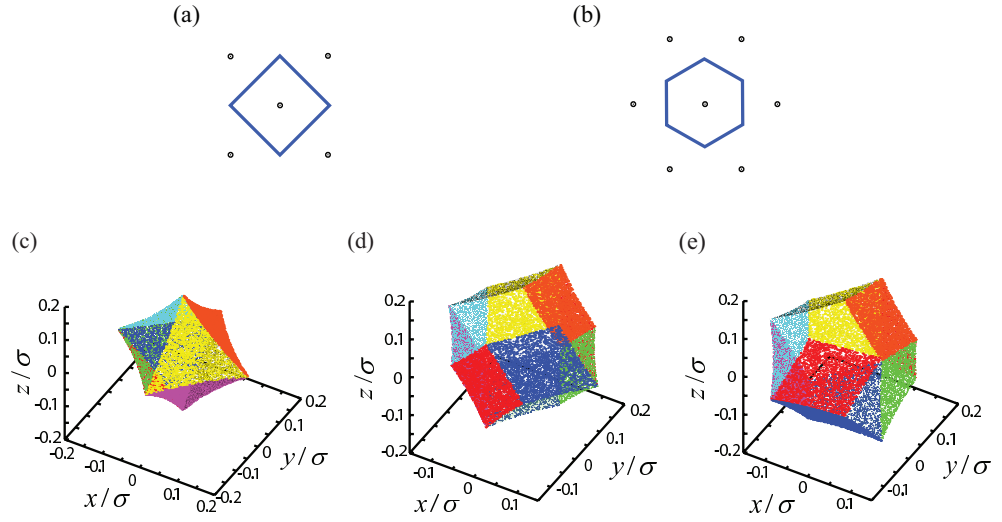

FIGURE 4.2: Shape of one–particle free volumes for (a) square and (b) hexagonally packed hard disk and for bcc, fcc and hcp ((c), (d) and (e) respectively) hard sphere crystals.

The second term in the Stillinger series for Q gives only a contribution different from 1 if the two fixed particles are neighbors. Thus the truncated Stillinger series is

$$Q_2 = \frac{1}{\Lambda^{3N}}(V_1)^N \prod_k \left(\frac{V_{2,k}}{(V_1)^2} \right)^{g_k N} \tag{4.7}$$

lattice	neighbor type	k	g_k
fcc	all neighbors	1	6
hcp	within close-packed plane	1	3
	in adjacent close–packed planes	2	3
bcc	all neighbors	1	4

TABLE 4.1: Neighbor configurations with multiplicities for the different lattices.

Here, $V_{2,k}$ is the correlated free volume of the two neighboring particles (with dimension [length]^6) which may depend on the type of neighbor configuration (index k). The power $g_k N$ reflects the freedom to choose the first of the two particles to be any of the N particles in the system and g_k is the multiplicity of the neighbor configuration. It is half the number of neighbors of type k for a given fixed particle. The associated free energy is

$$\beta F_2 \quad = \quad \beta F_1 - N \sum_k g_k \ln \left(\frac{V_{2,k}}{(V_1)^2} \right) . \tag{4.8}$$

For our considered lattice cases the neighbor types and multiplicities are given in Tab. 4.1. The cubic lattices fcc and bcc have only one neighbor type whereas for hcp there is a difference whether the neighbor is within the same close–packed plane or in an adjacent close–packed plane. See also Ref. [64] for the multiplicities corresponding to the third term in the series (fcc and hcp).

We calculate the two–particle volumes $V_{2,k}$ for different densities by a simple Monte–Carlo computation. For that we specify a suitably large cuboid volume V_c for each of the two free particles from which n sets of random positions (for each of the two particles) are drawn. For each set of random positions overlap is checked with the other particle and the fixed neighboring particle, leading to a total of n' sets of random positions with no overlap. Then $V_{2,k} = (n'/n)V_c^2$. The statistical error $\Delta V_{2,k}/V_{2,k}$ needs to be below 10^{-5} for a reliable assessment of the free energy difference between fcc and hcp, and this is achieved with 1000 subsets, each containing $n = 10^9$ sets of random positions. In the limit $\rho_0 \to \rho_{\mathrm{cp}}$ ($\rho_{\mathrm{cp}} = \sqrt{2}/\sigma^3$ is the close–packing density) agreement was found with the analytical results of Ref. [64], but we had to approach ρ_{cp} very closely to establish that.

4.3 Results

4.3.1 Stillinger Series

For fcc and hcp, the Stillinger series truncated at $n = 2$ gives very good results for the free energy per particle F/N (see Fig. 4.3, to obtain numbers, we put $\Lambda = \sigma$). We have compared the free energy to very precise simulation data obtained in Refs. [66, 70] which have an error of about 0.002 $k_\mathrm{B}T$. The Stillinger series ($n = 2$) results for F/N deviate from these ranging from 0.01 $k_\mathrm{B}T$ (at $\rho_0\sigma^3 = 1.0$) to 0.03 $k_\mathrm{B}T$ (at $\rho_0\sigma^3 = 1.15$), this is less than 0.5% relative deviation. This is about the same accuracy we obtain with FMT (see also Ref. [66]). Note, however, that a deviation of the order of 0.01 $k_\mathrm{B}T$ is about 10 times higher than the fcc–hcp free energy difference obtained from simulations, as discussed before.

For bcc, the situation is very much different. Since the bcc structure for hard sphere is unstable against shear, the crystal can be stabilized in simulations only by constraints such as in the self-occupancy cell (SOC) method. We would expect from the previous derivation that the Stillinger expansion is a reasonable series expansion for the free energy of the SOC method. However, as Fig. 4.3 demonstrates, the first two terms are quite far away from the SOC data and also from the FMT results for the branch with lowest free energy, pointing to the importance of higher correlations. (Ultimately, the shear instability is a collective many–body effect, so perhaps the importance of many–particle correlations also in the constrained crystal is not too surprising.) See, however, the next subsection for a more detailed discussion on bcc solutions within FMT, especially with regard to a solution branch with higher free energy which appears to be linked to the bcc Stillinger solution.

Finally, for fcc/hcp the inclusion of the correlated neighbor term *increases* the free energy, whereas for bcc it leads to a *decrease*.

4.3.2 bcc – FMT Results

As already discussed, a bcc crystal solution can only be stabilized by constraints. In FMT, these are the periodic boundary condition on the cubic unit cell. Within the Gaussian parametrization (see Eq. (4.3)), bcc solutions in FMT (Rosenfeld, Tarazona

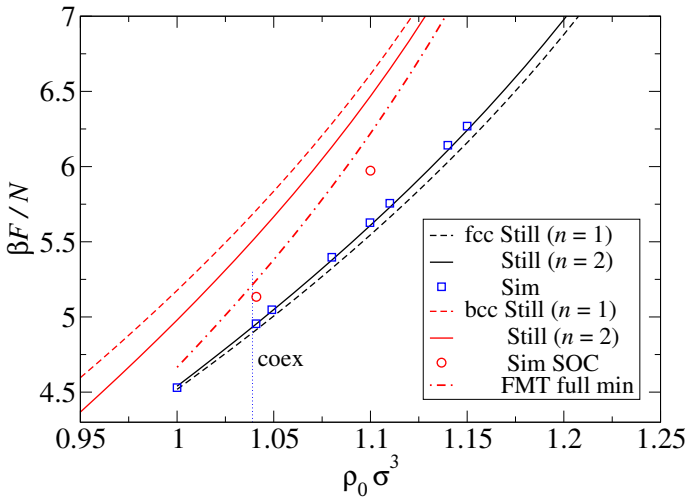

FIGURE 4.3: Crystal free energies $\beta F/N$ for fcc and bcc from the Stillinger series in comparison to simulation data and FMT results (bcc). For fcc, simulation data are taken from Refs. [66, 70], and for bcc, simulation data are obtained using the single–occupancy cell method (SOC) [71]. The FMT data are this work, see Sec. 4.3.2.

and White Bear Tensor, see Sec. 3.3) have been investigated by Lutsko [72] (with the additional constraint $n_{\text{vac}} = 0$, such that in the free energy minimization, the width parameter α is the only variable which is varied at a given bulk density ρ_0). For small bulk densities ($\rho_0\sigma^3 \lesssim 1.16$), Lutsko found a single free energy minimum with a rather small width parameter $\alpha \approx 30 \ldots 40$, indicating a broad Gaussian peak. Interestingly, $\alpha(\rho_0)$ exhibits a maximum at $\rho_0\sigma^3 \approx 1.13$ and then *decreases* again upon increasing the density (i.e. the density peaks become wider upon compressing the crystal!). Moreover, at bulk densities $\rho_0\sigma^3 \gtrsim 1.16$ a second free energy minimum was visible (with higer free energy). In this second branch, the width parameter increased (the peak width decreased) with increasing density as one would naively expect (Fig. 4.4).

We investigate these findings further using full minimization. For the first branch with lowest free energy, we confirm that there is a minimal width of the peaks at $\rho_0\sigma^3 \approx 1.13$. Full minimization reveals a rather strong deviation from the simple Gaussian form in the density peaks: The difference in free energy per particle F/N between Gaussian and full minimization is about 0.1 $k_{\text{B}}T$ (see Fig. 4.5 (a)) and thus about 2 orders of magnitude higher than in the case of fcc [66]. Curiously, this free energy difference increases with increasing density beyond $\rho_0\sigma^3 \approx 1.07$. Secondly, the equilibrium vacancy concentration n_{vac} is of the order of 10^{-2} and thus *several orders of magnitude higher* than found in

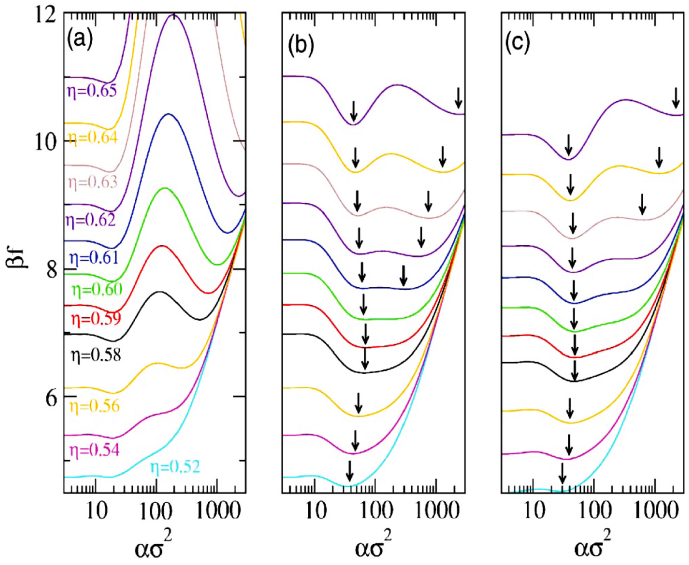

FIGURE 4.4: (a) Free energy per particle, $\beta f = \beta F/N$, as a function of width parameter α, for the bcc hard sphere crystal calculated using (a) the Rosenfeld, (b) Tarazona Tensor and (c) White Bear Tensor functionals for various densities. The arrows indicate the position of the secondary crystal minima [72].

fcc. $n_{\mathrm{vac}}(\rho_0)$ has a minimum at $\rho_0\sigma^3 \approx 1.10$ and then increases again, adding to the peculiarities of this solution branch. We note that in an FMT study of parallel hard squares and cubes similar peculiarities have been found [73].

The second branch found by Lutsko is not an artefact of the constrained Gauss minimization. By a careful iteration procedure, we found corresponding fully minimized solutions whose free energy per particle is very close to the values from the Gaussian approximation (thus very much like the fcc solutions and very much unlike the solutions from the first branch), see Fig. 4.5 (b). For increasing densities, we see a convergence of F/N to the results of the Stillinger series ($n = 2$). Thus the second branch of the bcc solutions has the same character as the fcc solution when compared with the Stillinger approach: only a few correlated particles are sufficient to obtain the free energy.

One could argue that the discussion of these bcc solutions is futile and void of physical significance in view of their overall instability. However, the quality of the FMT functionals and their success in describing the fcc phase leads us to think that these solutions are perhaps not to be discarded altogether. Since around coexistence ($\rho_0\sigma^3 \approx 1.04$) the difference in F/N to the fcc crystal is about 0.3 $k_{\mathrm{B}}T$ and thus very high, it is reasonable that bcc crystallites have not been observed in the nucleation process of a hard sphere

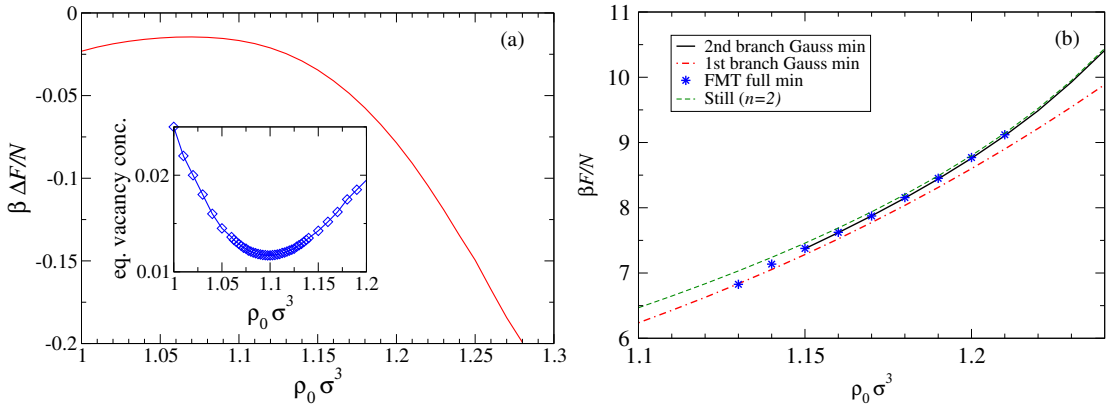

FIGURE 4.5: (a) Difference in free energy per particle between the fully minimized and the Gaussian solution for the first branch of the bcc solutions as a function of bulk density. Inset: Equilibrium vacancy concentration as a function of bulk density for the same first branch. (b) Free energy per particle as a function of bulk density for the bcc solution of the second branch: Full minimization (symbols, $n_{vac} = 6 \times 10^{-4}$ fixed) and Gaussian approximation (full black line). For comparison the Stillinger result ($n = 2$) is given (dashed line) as well as the Gaussian approximation for the first branch (dot–dashed line).

crystal. Nevertheless, the bcc solutions are perhaps a useful reference point for discussing the crossover from fcc to bcc as the most stable crystal structure for other potentials such as of $(\sigma/r)^n$ type. These could be treated by suitable perturbation ansatz in the free energy functional. Also, it could be interesting to further investigate the dispersion relation of phonons for the solutions of the first branch and thus shed further light on the shear instability.

4.3.3 fcc/hcp: Free Energy Differences and Density Anisotropies

For hard spheres, it is a delicate issue whether fcc is more stable than other close–packing structures, most notably hcp. In Stillinger's approach, The free energy of hard sphere crystals can be expanded in terms of the number n of contiguous particles (free to move) in an otherwise frozen matrix of particles at their ideal lattice positions. This expansion could be done analytically only for densities in the vicinity of close–packing and, for $n = 2$ and $n = 3$ (by quite a *tour de force*), resulted in hcp being more stable than fcc by a free energy difference per particle $\Delta F/N \sim 10^{-3}\ k_{\mathrm{B}}T$. However, the individual terms contributing in this series are much larger than this value of $\Delta F/N$. An extension of this method [74] (still only near close–packing) to $n = 5$ shows the reverse situation: fcc

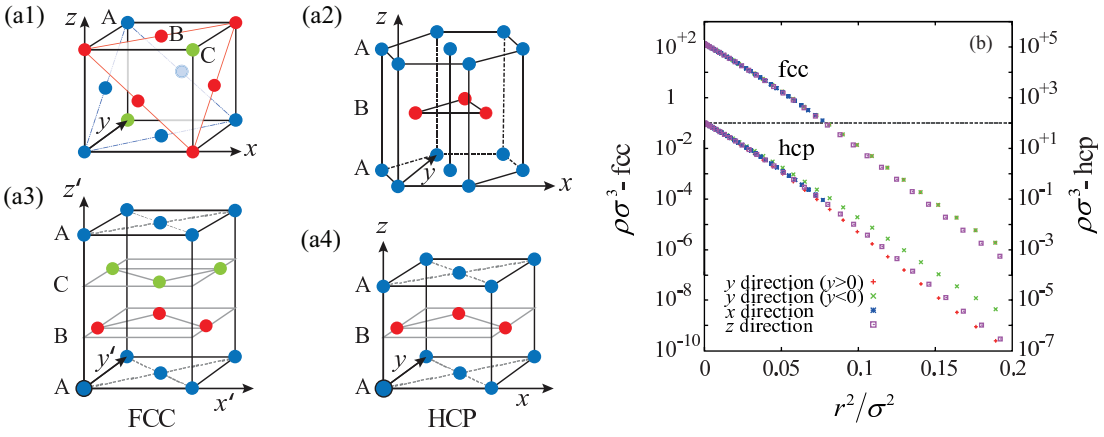

FIGURE 4.6: Unit cells and density anisotropies for fcc and hcp. (a1) and (a2) show the most convenient unit cells (cubic for fcc and hexagonal for hcp) for the mathematical discussion of the density anisotropies (see Eqs. (4.9) and (4.10)). (a3) and (a4) show the unit cells used in the numerical computations. The hexagonally packed planes (marked in different colors) lie oblique in the cubic unit cell (a1). (b) fcc and hcp density distributions around the lattice site at the origin in different directions. Here, we used the bulk density $\rho_0\sigma^3 = 1.04$ and fixed the vacancy concentration to $n_{\mathrm{vac}} = 10^{-4}$.

is more stable than hcp and $\Delta F/N \sim -10^{-3}\ k_{\mathrm{B}}T$, but the last term in the series is still larger in magnitude than $\Delta F/N$ (about 6 times for fcc and 3 times for hcp). Simulation work confirms the stability of fcc over hcp also for smaller densities (around coexistence). Using a single–occupancy cell (SOC) method, Ref. [75] estimates $\Delta F/N = -(5\pm1)\cdot10^{-3}$ $k_{\mathrm{B}}T$ at a density of $\rho_0\sigma^3 = 1.041$ (approximately at coexistence, σ is the hard sphere diameter). In this method, particles are constrained to their Wigner–Seitz cells and the free energy difference is found by integrating the equation of state. The limitations of this method could be overcome by the powerful Monte–Carlo (MC) lattice switch method which allows to compute the free energy difference between two different lattice structures directly [65]. At $\rho_0\sigma^3 = 1.10$ the result is $\Delta F/N = -(0.86 \pm 0.03) \cdot 10^{-3}$ $k_{\mathrm{B}}T$. Thus the result of the high–density Stillinger series for $n = 5$ for the stability of fcc over hcp and the magnitude of the free energy difference is consistent with the MC simulation result at a considerably smaller density. One may tentatively conclude that for all densities the stability of fcc in the hard sphere system is a subtle result of the correlated movement of five and more particles and the effect in the free energy is very small.

FMT gives the same free energy per particle F/N for fcc and hcp when the Gaussian approximation is employed [50, 72]. Free minimization lifts this degeneracy in the free

energy. In order to understand this result qualitatively, it is useful to consider the symmetries in the unit cell of fcc/hcp and the constraints these symmetries place upon the lattice–site density profiles. For fcc, this is best discussed by considering the cubic unit cell in Fig. 4.6 (a1). The non–radial contributions to the density profile around the lattice point in the origin can be expanded in a Taylor series in x, y, z where the terms in this series must respect the 48 point symmetry operations in the cubic unit cell (belonging to point group $\frac{4}{m}\bar{3}\frac{3}{m}$ in Hermann–Mauguin notation) [66]:

$$\rho_{\mathrm{fcc}}(x,y,z) = \rho_{\mathrm{rad}}(r)\,(1 + K_4(x^4 + y^4 + z^4) + \dots)\,. \tag{4.9}$$

Here, $\rho_{\mathrm{rad}}(r)$ is an averaged, radial profile which is more or less of Gaussian shape. The leading anisotropic term is of polynomial order 4 with expansion coefficient K_4. One can also understand this result by resorting to an expansion in the subset of spherical harmonics which respect the cubic point symmetry, this leads to an expansion in the so–called Kubic Harmonics [76]. For hcp, we consider the unit cell in Fig. 4.6 (a2). The corresponding Taylor expansion for the non–radial contributions to the density profile around the lattice point in the origin has to respect only the 24 point symmetry operations appropriate for the hexagonal group $\frac{6}{m}\frac{2}{m}\frac{2}{m}$. According to Ref. [77], this leads to

$$\rho_{\mathrm{hcp}}(x,y,z) = \rho_{\mathrm{rad}}(r)\,(1 + K_2' z^2 + K_3' y(3x^2 - y^2) + \dots)\,, \tag{4.10}$$

where polynomial terms up to order 3 have been taken into account (with expansion coefficients K_i'). The corresponding construction using spherical harmonics leads to the so–called Hexagonal Harmonics. We observe that there is a qualitative difference in the shape of the density profile between hcp and fcc according to these expansions:

(i): To leading order in anisotropy for hcp, the density peak $\rho(r)$ should look different in z–direction (perpendicular to the hexagonally packed planes) than in directions in the x–y plane. To phrase it differently: one would expect different width parameters $\alpha_z, \alpha_{x,y}$ for a Gaussian density peak of the form $\rho_{\mathrm{hcp}}(x,y,z) \propto \exp(-\alpha_{x,y}(x^2 + y^2) - \alpha_z z^2)$. We did not observe this in our numerical solutions but we will return to this point below.

(*ii*): To next–to–leading order in the anisotropy for hcp, we expect a different behavior when comparing $\rho(0, y, 0)$ with $\rho(0, -y, 0)$ due to the antisymmetric term $\propto K_3'$ in Eq. (4.10). Such a symmetry breaking is not present in the fcc peak. To demonstrate this difference, we compare $\rho(0, \pm y, 0)$, $\rho(x, 0, 0)$, and $\rho(z, 0, 0)$ between fcc and hcp, see Fig. 4.6 (b) and (c).[1]

Indeed we observe that the symmetry is broken for the hcp profile, in accordance with the anisotropy expansion, and we conclude that the fcc/hcp free energy difference in FMT results from this symmetry breaking.

The results for the fcc/hcp free energy difference per particle are given in Fig. 4.7(a). In FMT (White Bear II–Tensor), the difference $\beta\Delta F/N$ is larger than zero, implying that hcp has lower free energy. Furthermore, there is only a moderate drop of $\beta\Delta F/N$ with the bulk density ρ_0. At coexistence ($\rho_0\sigma^3 = 1.04$), we have computed $\beta\Delta F/N$ also for other FMT functionals (Tarazona–Tensor, White Bear–Tensor) and found no change in sign but a variation in magnitude by 50% or $5 \cdot 10^{-4}$. In view of the variation of $\beta F/N$ for fcc between the functionals (about $4 \cdot 10^{-2}$, i.e. a factor of 80 larger), the functionals are very consistent with each other with respect to the stability of hcp. The results from the Stillinger series ($n = 2$) for $\beta\Delta F/N$ are approximately constant ($\sim 1 \cdot 10^{-3}$) with increasing density and coincide with the analytical value at close packing obtained in Ref. [64]. It is remarkable that the FMT results seem to converge to this value as well. For comparison, in Fig. 4.7(a) we have also included the analytical value from the Stillinger series ($n = 5$) [74] and the simulation value of Ref. [65]. Although FMT does not agree with the sign of $\beta\Delta F/N$ obtained in the simulation, it is gratifying to note that according to these results FMT is correct on the level of two correlated particles in the Stillinger picture.

Finally, we return to the observation that in the hcp density anisotropy the leading term $\propto z^2$ (see Eq. (4.10)) was missing in our numerical solutions. This is related to our choice of the distance between the hexagonally packed layers ($c/2 = c_0/2 = \sqrt{2/3}a$ where a is the nearest neighbor distance, see Fig. 4.1). With this choice the distance between

[1] Note that in our numerical computations we used the unit cells depicted in Fig. 4.6 (a3) (fcc), and in Fig. 4.6 (a4) (hcp). Thus, the fcc cubic unit cell and the unit cell in Fig. 4.6 (a3) are related by a three–dimensional rotation. Likewise, the anisotropy expansion for the extended unit cell must be obtained from the corresponding expression (4.9) for the cubic unit cell by applying this rotation. Let x, y, z be the coordinates of the cubic unit cell, and x', y', z' the ones in the rotated system. The rotation $(x, y, z) \to (x', y', z')$ is a linear transformation. Thus $(x^4 + y^4 + z^4) = \sum_{ijk} a_{ijk}\, x'^i\, y'^j\, z'^k$ with the condition $i + j + k = 4$. For $x' = z' = 0$ only a term $\sim a_{040}\, y'^4$ can contribute to the sum on the rhs.

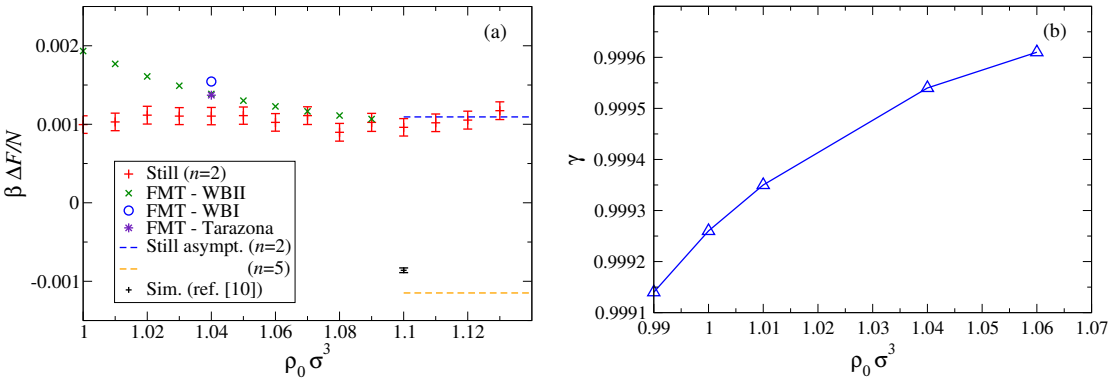

FIGURE 4.7: (a) Free energy difference between fcc and hcp vs. bulk density. The black symbol shows the simulation value from Ref. [65]. Rest of the symbols show the data obtained from FMT and the Stillinger series ($n = 2$) and dashed lines show the asymptotic behavior of the free energy difference near close packing for the Stillinger series (different n) [74]. (b) Distortion parameter $\gamma = c/c_0$ which minimizes the hcp free energy vs. bulk density. In all FMT calculations we put $n_{\mathrm{vac}} = 10^{-4}$.

nearest neighbors is the same for two sites within the same hexagonally packed planes and two sites in two adjacent planes. However, the hcp symmetry group does not require this, and one is free to choose another distance between the planes. With a different choice, also the nearest neighbor distance is different for sites in two different planes and also the width of the lattice site density profiles will be different in the direction normal to the hexagonally packed planes. We have investigated whether also the free energy minimum for hcp shifts to a value different from c_0. In order to keep the bulk density constant we defined a stretching parameter, $\gamma = c/c_0$, which describes the distortion of the crystal in z–direction. In order to keep the bulk density constant, we rescaled the nearest neighbor distance in the planes as follows: $a' = a/\sqrt{\gamma}$. Full minimization was done for a range of γ values. The result for γ which minimizes F/N is shown in Fig. 4.7 and it is seen that the equilibrium distortion is quite small, below 10^{-3}. The corresponding free energy shift per particle compared to the solution with $c = c_0$ is about 10^{-5} $k_{\mathrm{B}}T$. These results are actually similar to the ones in Ref. [78]: There, a similar lattice distortion was calculated for the zero–temperature Lennard–Jones hcp crystal by lattice sums.

4.4 Summary and Conclusions

In this chapter we have performed a study of bcc, fcc and hcp hard sphere crystals using unrestricted minimization in density functional theory (DFT) of Fundamental Measure type (FMT) which is currently the most accurate approach. We have complemented these investigations with an approach which is based on the expanding the crystal partition function in terms of number n of free particles while the remaining particles are frozen at their ideal lattice positions (Stillinger series).

For the metastable bcc crystal, we have found two solutions for bcc crystals whose free energies are well above the free energies of fcc/hcp (see Fig. 4.3 and 4.5(b)). The first solution (with a rather large density peak width at lattice sites) is characterized by a rather large equilibrium vacancy concentration (~ 0.01) and its free energy can not be described by the Stillinger approach. The shear instability of bcc is presumably related to this first solution. The second solution (characterized by a small peak width and small equilibrium vacancy concentrations) agrees well with the solution from the Stillinger approach ($n = 2$) with respect to its free energy.

The free energy degeneracy between fcc and hcp, found in previous approaches using constrained, rotationally–symmetric density peaks around lattice sites, is broken upon full minimization. The density asymmetries are qualitatively different for fcc and hcp and agree with expansions in respective lattice harmonics (see Fig. 4.6). We found that in FMT the free energy per particle is lower for hcp than the one for fcc by about 10^{-3} $k_{\mathrm{B}}T$. This agrees remarkably well with the Stillinger solution for $n = 2$ (see Fig. 4.7). Simulations, however, indicate that fcc has a lower free energy than hcp by about the same figure. Previous investigations of the Stillinger approach in the high–density limit (near close packing) have shown that hcp is more stable than fcc for $n = 2 \ldots 4$ and the situation reverses for $n = 5$. Thus, the stability of fcc seems to be a subtle effect involving the correlated motion of at least 5 particles which currently can not be captured by the FMT functionals.

Upon full minimization, also other density functionals should exhibit a free energy difference between fcc and hcp. For the Taylor expanded Ramakrishnan–Yussouff functional (using the Percus–Yevick direct correlation function and the reference density $\rho_{\mathrm{ref}} = 0.946$) we find a difference $\beta\Delta F/N = 0.06$ which is about 50 times larger than the

FMT (and Stillinger) result. Therefore, it seems that the functional expansion around the liquid state (underlying the Ramakrishnan–Yussouff functional) has no connection to the Stillinger expansion.

Chapter 5

Hard Sphere Fluid at a Soft Repulsive Wall

5.1 Introduction

Crystal growth is a very important branch of condensed matter physics and industry with numerous applications ranging from semiconductors, organic systems, nano–structures, substrates for high temperature superconductors, piezo sensors, ferroelectric memories and quantum dots. There are different facets to crystal growth—homogeneous nucleation, heterogeneous nucleation, epitaxial growth, molecular beam epitaxy, etc [2].

One of the main purposes of this research project is to understand the nucleation process of simple model systems and for this one needs to investigate free energies, density distributions and crystal–liquid and liquid–wall interfacial properties. Free energies and density profiles of hard–sphere crystals have been extensively studied in literatures using various methods like simulation [79, 80], DFT [66, 67, 81] and PFC [67] as well as Chapter 4 of this thesis. The density profile and the interfacial properties of the hard–sphere crystal–fluid interface have been under intense scrutiny using DFT [82] and simulation [82–88] approaches.

In the nucleation process of real systems it is usually found that some impurities are present on which the new phase may be nucleated with lower activation energy than for homogeneous nucleation. The role of impurities and seeds has been investigated in

simple model systems under various conditions, such as microgravity [89], in the presence of large spherical impurities in colloidal suspensions [90] and with variable impurity size through MC simulations [91, 92]. A recent transition path sampling analysis [92] has shown that pre–structure minimal crystalline seeds commensurate with the bulk stable crystal phase enhance the crystallization rate by many orders of magnitude while incommensurate ones have no effect.

Heterogeneous crystallization on planar surface has also been extensively studied due to its simplicity for several model systems [93–96]. In the case of colloidal suspensions of hard spheres against unstructured flat substrate, complete wetting of the wall by the crystal occurs when the fluid packing fraction approaches the freezing point and the formation of oriented crystal with close–packed planes parallel to the substrate is induced [95, 97].

It has been demonstrated that for colloidal suspensions the effective interactions are tunable from hard spheres to soft repulsion [98–100] or weak attraction [101, 102] and at the same time the structure of fluid–crystal [103–106] and fluid–wall interfaces can be analyzed in arbitrary details, e.g., by visualizing the packing of particles in these interfaces [106]. Correspondingly, there is a great interest in model studies pertinent to such systems. However, most work has focused on the hard–sphere colloidal fluid [13–15, 107] confined by hard walls [95, 108–120].

Now it is well known that the interaction between colloidal particles and walls can also be manipulated, by suitable coatings of the latter, e.g., via a grafted polymeric layer (using the grafting density and chain length of these polymers, under good solvent conditions, as control parameters [121, 122]). In this chapter a model is presented where colloidal particles have an effective hard–sphere interaction in the bulk, experience a soft repulsion from confining walls. The actual motivation of the Mainz study[1] was to test if a variable contact angle can be obtained for hard spheres at repulsive walls. This could allow studying heterogeneous nucleation. The main work has been done using simulation(see Ref. [123]) and DFT was performed to check the accuracy of FMT functionals.

[1] This work was done when I was in Johannes Gutenberg University of Mainz with collaboration with simulation people in 2011.

5.2 Confined Hard Colloidal Particles Model

The model is the simple fluid of hard particles of diameter σ, confined between two parallel walls located at $z = 0$ and at $z = D$. In the x and y directions, periodic boundary conditions are applied throughout. The particle–wall interaction contains either a hard wall (HW) type interaction

$$V_{\mathrm{HW}}(z) = \begin{cases} \infty & \text{if } z < \sigma/2 \text{ or } z > D - \sigma/2 \\ 0 & \text{otherwise} \end{cases}, \tag{5.1}$$

or a soft repulsion of the Weeks–Chandler–Andersen (WCA) [124] type

$$V_{\mathrm{WCA}}(z) = \begin{cases} 4\epsilon\left[\left(\frac{\sigma_w}{z}\right)^{12} - \left(\frac{\sigma_w}{z}\right)^{6} + \frac{1}{4}\right] & \text{if } 0 \le z \le \sigma_w 2^{\frac{1}{6}} \\ 4\epsilon\left[\left(\frac{\sigma_w}{D-z}\right)^{12} - \left(\frac{\sigma_w}{D-z}\right)^{6} + \frac{1}{4}\right] & \text{if } (D - \sigma_w 2^{\frac{1}{6}}) \le z \le D \\ 0 & \text{otherwise} \end{cases}, \tag{5.2}$$

In the Equation (5.2), $\sigma_w = \sigma/2$ is chosen, while the parameter ϵ controls the strength the soft repulsion of WCA walls. Note that for $\epsilon = 0$ Equation (5.2) becomes a hard–core (HC) potential $V_{\mathrm{HC}}(z) = \infty$ for $z < 0$ and $z > D$, respectively which is much similar to HW potential defined in (5.1) but with the difference that the position of the walls are at $z = -\sigma/2$ and $z = D + \sigma/2$ for HC potential and are at $z = 0$ and $z = D$ as for HW. The advantage of the choice of Equation (5.2) from the theoretical point of view is that ϵ is a convenient control parameter: varying the wall–fluid interfacial tension γ_{wf} as well as the wall–crystal interfacial tension γ_{wc} can be modified. Note that the direct effect of V_{WCA} is zero in the range $\sigma_w 2^{1/6} < z < D - \sigma_w 2^{1/6}$: thus, when D is very large, we expect that the structure of the hard sphere fluid in the center of the slit (very far from both walls) is identical to a corresponding hard sphere fluid in the absence of confining walls (applying periodic boundary conditions also in the z–direction).

5.3 Density Functional Theory: FMT Toolbox

DFT allows us to study the inhomogeneous structure of a fluid subjected to an external potential (wall potential) and corresponding thermodynamic quantities within the same

framework. It has been shown that FMT is able to predict the density distribution and surface tension of the hard–sphere system at a hard–wall potential with a good accuracy [46]. It is known that the density value at the *hard wall*, so–called contact density, equals to the bulk pressure of the system

$$\rho = \beta p. \tag{5.3}$$

Since FMT type functionals are WDA functionals, the contact theorem as one of the sum–rules[2] should be satisfied in the FMT approach. In general, one can conclude that close to the hard–wall, a version of FMT that is based on the Carnahan–Starling–Boublík equation of state (EOS) [125, 126] should be more accurate than those functionals which are based on the Percus–Yevick EOS. While for low bulk density the difference between these two EOSs is rather small, this difference becomes more important for the densities close to the freezing density [46].

In this study two variants of FMT (White Bear II and White Bear II Tensor) are used to obtain the equilibrium density profile of confined hard–sphere fluid between repulsive walls with different strengths as well as hard–walls. The simplest initial density profile to start the iteration process is a constant density $\rho(\mathbf{r}) = \rho_b$ between walls and no particle ($\rho = 0$) outside the confinement. Iterations are done using the Picard method (Appendix C.1) with variable mixing parameter $\alpha = 10^{-5} \ldots 5 \times 10^{-2}$. This range of α stabilizes the iteration process. For more details on implementing FMT see Appendix B.

It is useful to verify the FMT data using other approaches such as computer simulations. Usually this check is done solely for density profile. However it is important to also verify the accuracy of other thermodynamic quantities such as the wall surface tension. To simulate the confined fluid between walls in the standard canonical ensemble, the standard Monte Carlo algorithm [127] with local single particle moves is implemented. Details of the simulation method have been presented in Ref. [123]. It is also fruitful to check the self–consistency of our DFT code by sum–rules.

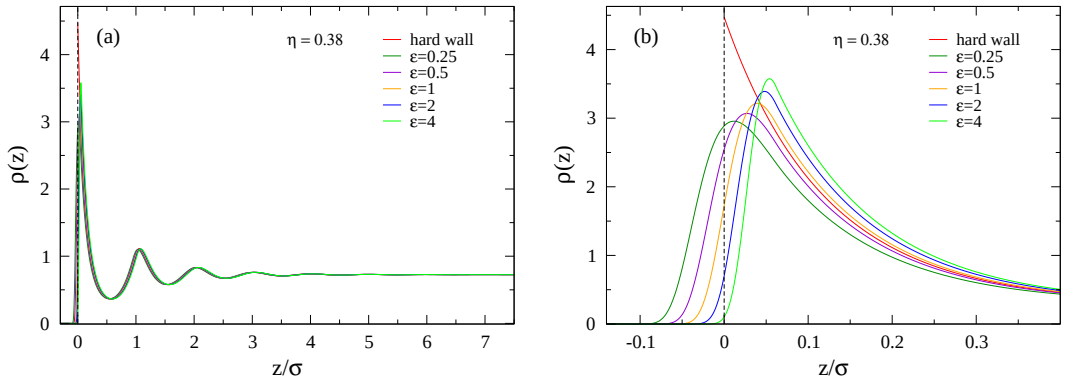

FIGURE 5.1: (a) Density profile $\rho(z)$ of the hard sphere fluid vs. z against the wall for five choices of ϵ and for the hard wall. For different values of ϵ, the same bulk density ρ_b is obtained. (b) shows the first peak of $\rho(z)$ close to the wall, resolved on a much finer abscissa scale.

5.4 Density Profile of the Hard Sphere Fluid at WCA Wall

By fully minimizing the free energy we can obtain the equilibrium density profile. Figures 5.1 and 5.2 show typical data for density profile $\rho(z)$ obtained from FMT for different strengths ϵ as well as different packing fractions η. Although the density profile for the different choices of ϵ looks similar (Figure 5.1 a), but by looking closer to the first peak of $\rho(z)$ adjacent to one of the walls (Figure 5.1 b), one sees the influence of ϵ on the density: the larger ϵ, the more remote from the wall the peak occurs. However for $\sigma_w 2^{1/6} < z < D - \sigma_w 2^{1/6}$, i.e., outside the range where the wall potential acts, the effect of varying ϵ is negligible. One sees that for the packing fraction close to the fluid–solid transition, $\eta = 0.49$, peaks close to the wall growth and "layering" occurs (Figure 5.2). Figure 5.3 shows a plot of surface excess packing fraction η_s, as a function of bulk density η_b. One sees that η_s depends in a nontrivial way on both η_b and ϵ. It can also be seen that for packing fractions higher that $\eta_b = 0.4$ there is a systematic discrepancy between DFT and simulation, while for lower packing fractions both methods are in excellent agreement. Interestingly, for $\epsilon = 1$, the data are rather close to the case where a hard–core potential is used at the wall. The latter case has been studied before by Laird and Davidchack [120] and the DFT calculation is found to be in excellent agreement with recent simulation data [120, 123].

[2]Sum–rules are statistical mechanical connections between microscopic properties of a system and thermodynamic quantities. Besides establishing connections between different quantities, they allow us it allows us to test the internal (self–) consistency of a DFT code. [46].

packing fraction η		0.35	0.43	0.49
contact density	WBII	3.47976643	6.80865140	11.3753570
	WBII-T	3.47976414	6.80863492	11.3752992
pressure		3.47977758	6.80870977	11.3755775

TABLE 5.1: Hard wall contact density for different packing fractions for two variants of FMT, White Bear II and White Bear II Tensor functionals. Excellent agreement between contact densities and pressures verify the success of FMT in satisfying the contact theorem.

FMT functionals accuracy and self–consistency can be verified by sum–rules. For the hard spheres fluid at a hard–wall we can use contact theorem (5.3). Table 5.1 shows the contact density of the hard sphere fluid and the bulk pressure. One sees that there is an excellent agreement between contact densities and pressures. For soft walls, the Gibbs theorem (5.5) can be used. The Gibbs adsorption theorem as a second sum–rule, connects the excess adsorption (excess density) with the derivative of the surface tension γ w.r.t. the chemical potential

$$\rho_s = \int_0^\infty [\rho(z) - \rho_b]\,\mathrm{d}z = -\left(\frac{\mathrm{d}\gamma}{\mathrm{d}\mu}\right)_{V,T}, \tag{5.4}$$

$$\eta_s = \frac{\pi}{6}\rho_s, \tag{5.5}$$

here η_s is the excess packing fraction. The surface tension γ is defined by

$$\gamma = \frac{\Omega + pV}{A}, \tag{5.6}$$

where Ω is the grand canonical free energy, V is the system volume, p denotes the pressure and A is the planar interface area. Figure 5.4 shows that there is about 3% discrepancy between the right and left hand sides of Equation (5.4). For the hard wall this difference is due to the numerical discretization and results converge for finer resolutions. Although the results get closer for better resolutions in the case of the soft wall, the residual discrepancies remain about 2% which is not very clear.

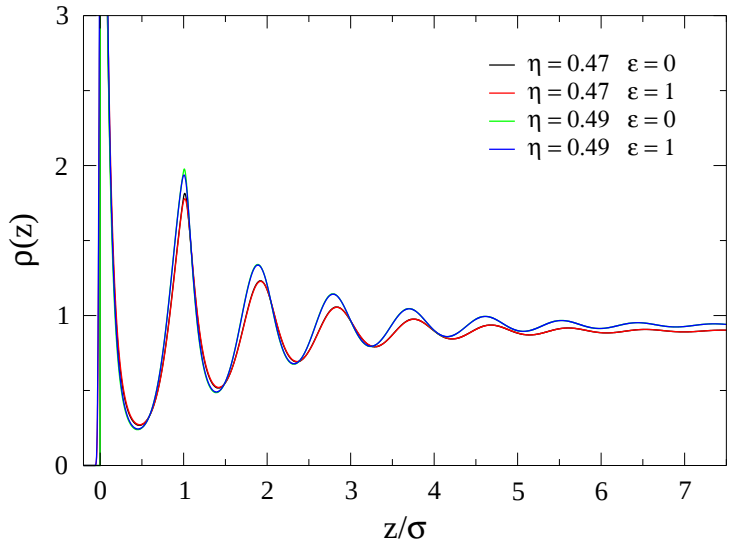

FIGURE 5.2: Density profile $\rho(z)$ of the hard sphere fluid vs. z against the wall for two different packing fractions η. Note that in both cases two choices of ϵ are shown, namely $\epsilon = 0$ (hard wall system) and $\epsilon = 1$, but on the scale of the plot these data coincide.

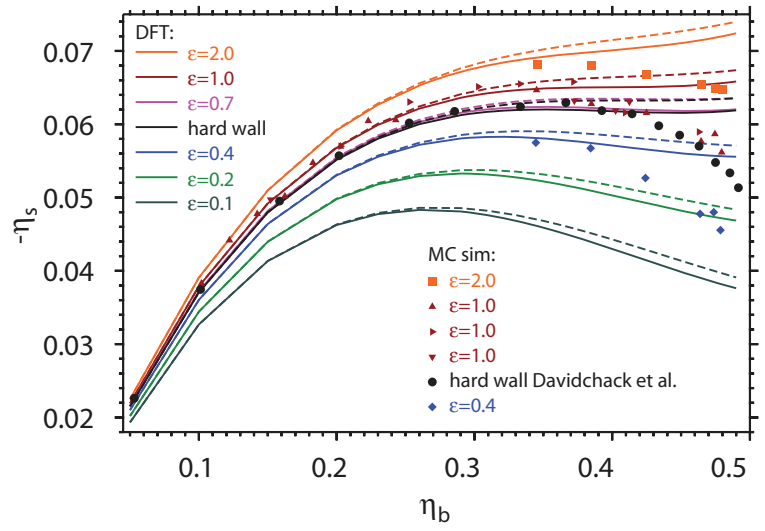

FIGURE 5.3: Plot of the surface excess packing fraction $(-\eta_s)$ vs. the packing fraction $\eta_b = \rho_b\pi/6$, in the bulk for several choices of the strength ϵ of the WCA potential due to the wall (Equation (5.2)) and for the hard wall boundaries (Equation (5.1)). Symbols are Monte Carlo data [119, 120, 123] and lines show the corresponding DFT results. Here, full curves correspond to the WBII functional and dashed curves correspond to the WBII Tensor functional.

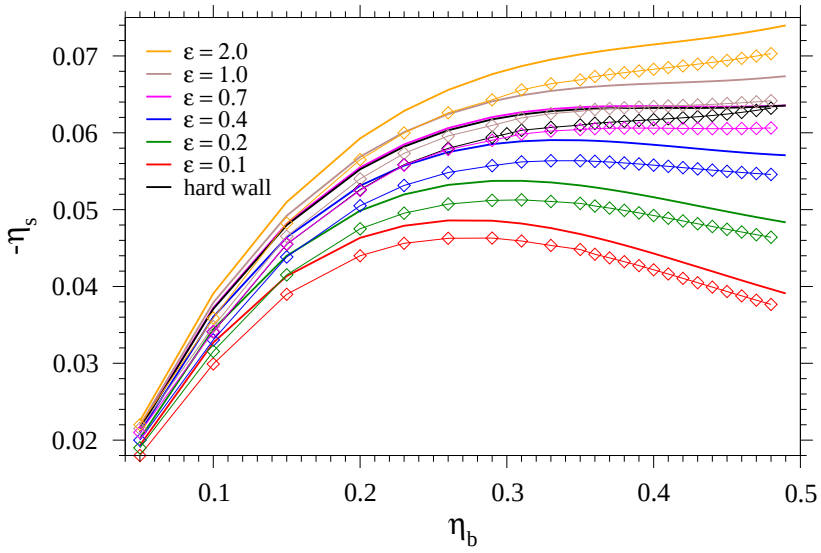

FIGURE 5.4: Same plot as Figure 5.3 to verify the Gibbs theorem (5.4). Solid lines show the data obtained form $\eta_s = \frac{\pi}{6}\int_0^\infty [\rho(z) - \rho_b]\,\mathrm{d}z$ and symbols present the data obtained from the r.h.s. of Equation (5.4), $\eta_s = -\frac{\pi}{6}\left(\frac{\mathrm{d}\gamma}{\mathrm{d}\mu}\right)_{V,T}$.

5.5 Hard Sphere Wall–Fluid Interface

As a test for our FMT functionals, it is useful to consider the hard wall case (Equation (5.1)) first. The case of hard wall has been extensively studied in the literature [112, 118–120]. Figure 5.5 shows that DFT results compare very well with simulation data over a wide range of packing fractions. Only close to the freezing transition small but systematic deviations appear. In the case of a WCA wall (Equation (5.2)), varying ϵ does have a pronounced effect on the density distribution of the HS fluid at the wall and it is clear that varying ϵ must lead to a change of wall–fluid surface tension $\gamma_{wf}(\epsilon)$ as well. The variation of $\gamma_{wf}(\epsilon)$ with the strength ϵ of the WCA potential (Figure 5.6) is plotted. As expected, by changing ϵ we can indeed obtain a variation of $\gamma_{wf}(\epsilon)$ over a wide range. Note that again the DFT results are very close to the MC data, particularly for $\eta_b \leq 0.45$ while closer to the freezing transition small but systematic discrepancies occur again. This very good agreement between DFT and simulations for γ_{wf} is expected from the fact that DFT describes the density very accurately close to the walls where V_{WCA} acts. More prominent deviations in the density profiles between simulation and DFT are seen near the second peak from the wall. DFT does not seem to account for its precise shape near freezing. This deficiency is also visible in the "hump" in the

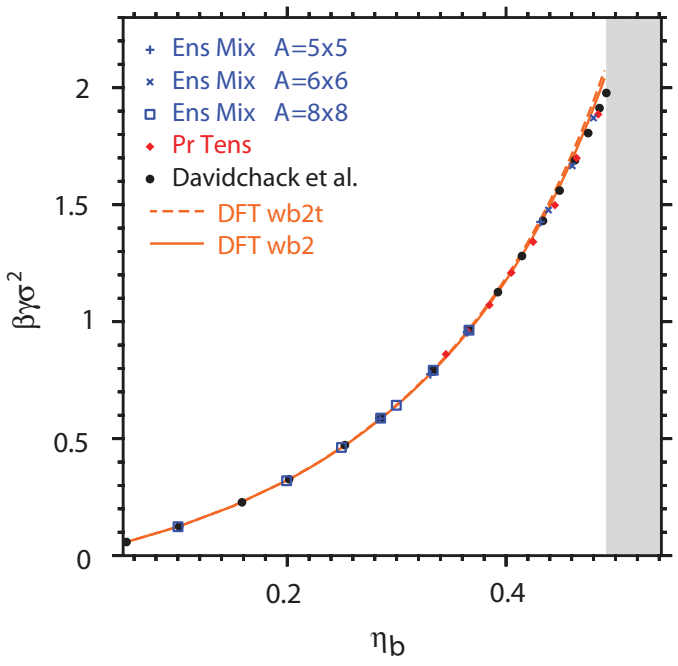

FIGURE 5.5: Wall–fluid surface tension γ_{wf} of the hard sphere fluid at the hard wall as a function of packing fraction η_b. Lines show the result of DFT calculation (full lines – White Bear II functional and dashed line – White Bear II Tensor functional). Symbols show simulation data [118–120, 123].

second peak of the pair correlation function near freezing which can be interpreted as a structural precursor to the freezing transition [128].

5.6 Conclusion

In this chapter, the effects of confining walls on a hard sphere fluid were studied over a wide range of packing fractions. The effect of the wall was described by using a WCA potential (5.2) acting on the fluid particles, but hard wall potential (5.1) was also studied. The main interest of this chapter was to verify the accuracy of FMT by means of a comparative study of FMT and simulation. For this purpose the surface excess free energy and the surface excess density are obtained. In the case of the hard–sphere fluid at a hard wall, FMT results satisfied the contact theorem for all packing fractions up to the freezing point ($\eta \leq 0.49$). For the latter case, FMT data could also satisfy the Gibbs theorem by finer discretization but 2% residual discrepancies remains for the soft wall case.

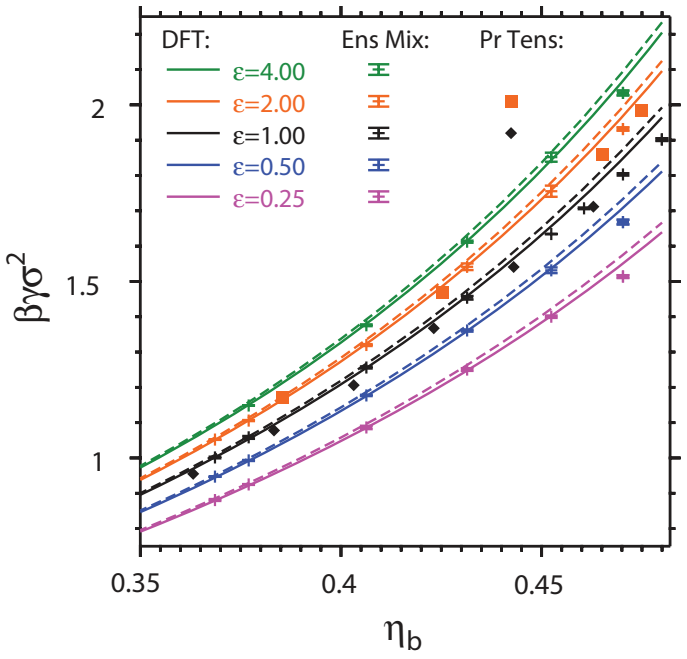

FIGURE 5.6: Wall–fluid surface tension γ_{wf} plotted vs. packing fraction η_b for the WCA wall potential (Equation (5.2)), varying its strength from $\epsilon = 0.25$ to $\epsilon = 4$. Lines show the result of DFT calculation (full lines – White Bear II functional and dashed line – White Bear II Tensor functional). Symbols show simulation data [123].

There was also a very good agreement between DFT and simulation in the fluid phase for not too large packing fractions ($\eta < 0.4$), irrespective of the choice of the wall–fluid potential that was used. For $\eta > 0.35$, systematic discrepancies between DFT and MC results for the surface excess density were found, which presumably should be attributed to the fact that for high densities in the fluid nontrivial correlations between the fluid particles beyond the nearest neighbor shell develop, which are no longer described by DFT with very high accuracy. However, DFT describes the density distribution very close to the walls quite accurately, and since this controls the wall–fluid surface tension, the latter is very accurately predicted by DFT. The motivation of this work was to control the difference $\gamma_{wf} - \gamma_{wc}$ at the bulk fluid–solid transition by varying ϵ in order to possibly observe a nonzero contact angle. It is found that the variation of this difference with ϵ is rather weak and the system is in the complete wetting region.

Chapter 6

Dynamical Density Functional Theory: From Bulk to Interface

Dynamical density functional theory is a time dependent extension of the basic static density functional theory. The time evolution of the density of Brownian particles is given as an integro-differential equation (3.72) in terms of the equilibrium Helmholtz free energy functional

$$\frac{\partial \rho(\mathbf{r},t)}{\partial t} = D\nabla\left(\rho(\mathbf{r},t)\nabla\frac{\delta\beta\mathcal{F}[\rho]}{\delta\rho(\mathbf{r},t)}\right). \tag{6.1}$$

DDFT is a relatively new technique and a lot of effort is going into the application of DDFT to the heterogeneous nucleation and crystal growth as well as micro-fluidic and biological systems. DDFT can be used to describe the out of equilibrium systems. It can also be implemented for equilibration which is rather modest task of DDFT. Hard–sphere crystals have been extensively studied using DFT and simulations and recently, the equilibrium hard sphere crystal–liquid interface has been investigated using DFT [82]. If a crystal is not in its equilibrium, according to conditions it may melt or grow. In the case of non–equilibrium crystal–liquid interface also two possible phenomena will occur, the HS crystal grows and the crystal–liquid interface moves toward the liquid phase, or the crystal partially or completely melts. We have lots of interests to study these two nonequilibrium problems in DDFT scheme and lots of efforts have been put in investigating their behaviors.

6.1 fcc Hard Sphere Crystal

As a warm up and to check our method and the accuracy of DDFT, fcc HS crystal is studied. The initial density $\rho(\mathbf{r})$ is approximated by a Gaussian profile (4.3)

$$\rho_{\mathrm{cr}}(\mathbf{r}) = \sum_{\text{lattice sites } i} (1 - n_{\mathrm{vac}}) \left(\frac{\alpha}{\pi}\right)^{3/2} \exp\left(-\alpha(\mathbf{r} - \mathbf{r}_i)^2\right), \tag{6.2}$$

with width parameter α and vacancy concentration n_{vac}. The density is discretized on a three dimensional grid with $64 \times 64 \times 64$ points in the x, y and z directions. We use White Bear II tensorial functional. Iterations are done in Euler scheme (Section C.3) and the constant step size $h = 10^{-4}$ is used for the time evolution of the system. Resulting density profile compares very well with DFT data and the free energy which comes out from DDFT, $\beta F_{\mathrm{DDFT}}/N = 4.967574$, is exact up to 5 digits after point ($\beta F_{\mathrm{DFT}}/N = 4.967573$) at density $\rho = 1.04$ and for vacancy concentration $n_{\mathrm{vac}} = 10^{-4}$. Numerical details are presented in detail in Section 6.3.

6.2 Crystal–Liquid Interface

The HS crystal–liquid phase transition occurs at the coexistence pressure $\beta p_{\mathrm{coex}} = 11.8676/\sigma^3$ and at the coexistence chemical potential $\beta\mu_{\mathrm{coex}} = 16.3787$. The coexistence packing fractions in the liquid and crystals sides are $\Phi_l = 0.495$ and $\Phi_{\mathrm{cr}} = 0.544$ respectively. These DFT results are from Ref. [66] which are in close agreement with computer simulation data [16]. DDFT equation is a conserved equation and keeps the number of the particles constant. Chemical potential as an external constraint is fixed to the coexistence chemical potential μ_{coex}. The density is discretized over the cuboid box of lengths L_x, L_y and L_z with periodic boundary conditions in all three directions. The surface normal vector points the z–direction. The length of the box in the z–direction, L_z, is chosen large enough to ensure a large part of crystal and liquid phases at coexistence which are separated by two interfaces. Usually grids for interface problem are chosen with $64 \times 64 \times 2048$ points in x, y and z directions. White Bear II tensorial functional is used and the density profile is minimized by using the Euler iteration scheme[1]

[1] See Section C.3.

with a very small time step. The time step is adjusted constantly during the iteration to ensure the convergence (Section C.4).

The initial profile contains two phases of crystals and a liquid phase which are separated by two interfaces. Figure 6.1 shows a typical crystal–liquid interface density profile. To

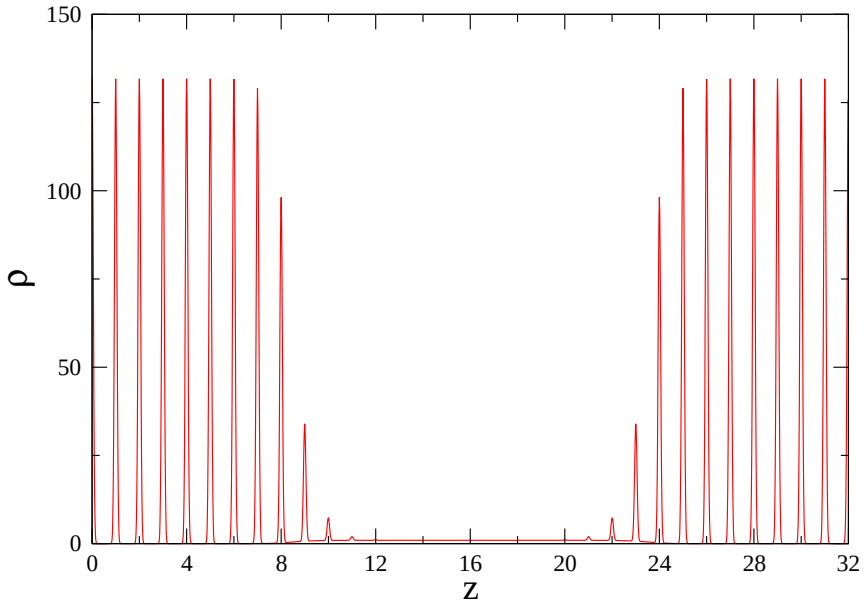

FIGURE 6.1: Schematic plot of crystal–liquid interface in z direction. z–axis is normalized by the length of the box in the x–direction, L_x.

constitute an initial crossover between the bulk and crystal phases, a variation $f(z)$ is introduced which is zero in the liquid phase and one in the crystalline phase [129–133]. We define $f(z)$ as follows

$$f(z) = \frac{1}{2}\left(-\tanh\left(\frac{z - z_0}{w}\right) + 1\right), \tag{6.3}$$

here z_0 is the location of the interface and the sharpness of the interface is determined through w. The mean bulk variation of the density, $\bar{\rho}(z)$, and the spatial resolved version $\rho(\mathbf{r})$ between the fcc crystal and the fluid bulk phases are defined as

$$\bar{\rho}(z) = (\rho_{\mathrm{cr}}(\mathbf{r}) - \rho_l) f(z) + \rho_l, \tag{6.4}$$

$$\rho(\mathbf{r}) = (\rho_{\mathrm{cr}}(\mathbf{r}) - \bar{\rho}(z)) f(z) + \bar{\rho}(z), \tag{6.5}$$

where ρ_{cr} is the density profile of the fcc crystal which is approximated by the Gaussian function (6.2) and ρ_l is the mean bulk density of the liquid.

Having established the initial density profile for the interface, the DDFT equation should be solved iteratively. Although DDFT equation in FMT scheme is very unstable and we could not fully converge the solution we got close to the fully minimize DFT solution. The surface tension (5.6) obtained from DDFT just before divergence is $\gamma_{\text{cl}} = 0.704$ in k_BT/σ^2 unit in [**001**] orientation which is not very far form DFT ($\gamma_{\text{cl,DFT}}$=0.678) and simulation ($\gamma_{\text{cl,Sim}}$=0.639) results [82].

In the following section numerical techniques on implementing DDFT are briefly discussed.

6.3 Numerical Methodology

In order to equilibrate crystals and interfaces in DDFT scheme we attempted various methods and tried many ways. Our attempts, experiences and findings are documented in this section.

Weight function $n_3(\mathbf{r})$: $n_3(\mathbf{r})$ is the packing fraction and it can not be larger that one. FMT type functionals are the only functionals that contain this physical restriction in their functional forms. In the free energy density functional, $1/(1-n_3)$ term in the second (3.39) and third (3.43) components imports this physical constraints in the functional. The divergence of DFT and DDFT equations is due to the $(1-n_3)$ term in the denominators. The maximum value of the starting $n_3(\mathbf{r})$ at its peak is $n_{3,max} = 1 - n_{\text{vc}}$. $n_{3,max}$ is very close to one (see Fig. 6.2), therefore the iteration should be performed very carefully to avoid n_3 exceeding one. During the iteration process, oscillations appear in n_3 peaks and these oscillations are amplified and at some point they become larger than one and the iteration diverges.

Time step: DDFT in FMT scheme is very stiff and has a small stability region in the Euler method which leads to a very small time step. The largest stable step size is estimated using the power method during the iterations (Section C.4). Usually after about 30 . . . 100 Euler iterations, the power method is used to find the

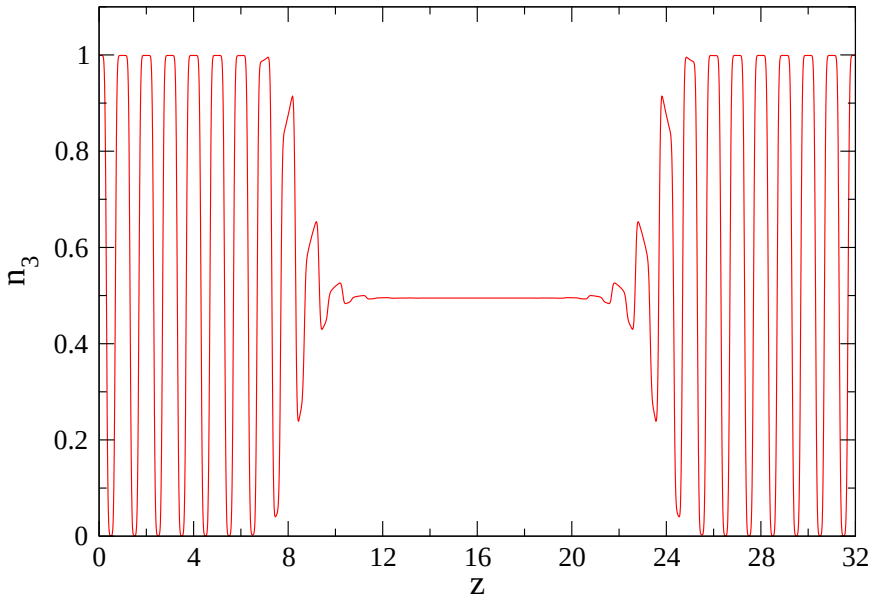

FIGURE 6.2: Initial weighted density $n_3(z)$ vs. z for hard sphere crystal–liquid interface. $n_3(z)$ is calculated by convolution of the initial density profile obtained form Equation (6.5) and weight function ω_3. z–axis is normalized by the length of the box in the x–direction, L_x.

stable region. The convergence rate is also constantly monitored. When divergence is observed the time step decreased immediately. The combination of these two methods provides the fastest convergence rate. If we do not concern with the computational time, we may choose a very small time step and avoid these methods.

Vacancy: The equilibrium vacancy concentration for the fcc crystal at coexistence density is $n_{\text{vac}} \sim 10^{-5}$ (FMT). The free energy shift compared to the vacancy free crystal ($n_{\text{vac}} \to 0$) is $\Delta F/N \sim 10^{-5}\, k_B T$. DDFT equation for $n_{\text{vac}} \sim 10^{-5}$ is very unstable and it is found that by increasing the vacancy concentration, the equation becomes more stable without loosing much accuracy in the free energy. $n_{vac} \sim 10^{-4}$ could be a good choice.

Differentiations: In DDFT approach we need to calculate lots of derivatives numerically. In our program we use finite difference method to calculate derivatives. The centered difference for the first and second order derivatives in one dimension are

given by

$$f'_m(x) = \frac{f(x+mh) - f(x-mh)}{2mh}, \tag{6.6}$$

$$f''_m(x) = \frac{f(x+mh) - 2f(x) + f(x-mh)}{(mh)^2}, \tag{6.7}$$

where h is the time step and m defines the roughness of the derivations. $m = 1$ is related to the familiar centered finite difference method which calculates the derivatives at point x with respect to the points just before and after x. By choosing $m > 1$, Equations (6.6) and (6.7) give rough approximations of derivatives and some details in the function are neglected during the differentiations. It is found that $m = 2$ in some problems makes the iteration process more stable.

Discretization: Discretizing a crystal profile over a box with $32 \times 32 \times 32$ grid points in x, y and z directions is not stable and after a while it diverges. The usual choice for a crystal unit cell has $64 \times 64 \times 64$ grid points in three directions. Although for high densities or low vacancies a finer discretization is useful for crystals, it is observed that in the crystal–liquid interface problem increasing the resolution does not help for having more stable iterations and it leads to a kind of instability.

Numerical solution schemes: Explicit and implicit methods are approaches used in numerical analysis for obtaining numerical solutions of time–dependent ordinary and partial differential equations. Explicit methods calculate the state of a system at a later time from the state of the system at the current time, while implicit methods find a solution by solving an equation involving both the current state of the system and the later one. Mathematically, if $X(t)$ is the current system state and $X(t+h)$ is the state at the later time (h is a small time step), then, for an explicit method

$$X(t+h) = F(X(t)), \tag{6.8}$$

while for an implicit method one solves an equation

$$Y(X(t), X(t+h)) = 0, \tag{6.9}$$

to find $X(t+h)$. It is clear that implicit methods require an extra computation (solving the above equation), and they can be much harder to implement. Implicit

methods are used because many problems arising in practice are stiff, for which the use of an explicit method requires impractically small time steps h to keep the error in the result bounded [134]. Since solving the DDFT equation implicitly is impossible we used two explicit schemes and one semi–implicit scheme which are explained below.

1. **Explicit scheme I:** Equation (6.1) can be discretized conveniently as follows

$$\rho_{j+1} = \rho_j + h\nabla\left(\rho_j \nabla \frac{\delta\beta\mathcal{F}}{\delta\rho_j}\right), \tag{6.10}$$

where $h = t_{j+1} - t_j$. The gradient operator is discretized using the mid–point centered difference method (6.6).

2. **Explicit scheme II:** The free energy functional $\mathcal{F}$ can be split into ideal and excess parts

$$\begin{aligned} \frac{\partial\rho}{\partial t} &= \nabla\left(\rho\nabla\left(\frac{\delta\beta\mathcal{F}_{id}}{\delta\rho} + \frac{\delta\beta\mathcal{F}_{\text{ex}}}{\delta\rho}\right)\right) \\ &= \nabla^2\rho + \nabla\left(\rho\nabla\frac{\delta\beta\mathcal{F}_{\text{ex}}}{\delta\rho}\right), \end{aligned} \tag{6.11}$$

here $\nabla^2\rho$ is the diffusion term. Laplace operator in the diffusion term is discretized using the second order central difference method (6.7) while gradients are calculated using (6.6) numerically. Now the equation can be solved explicitly

$$\rho_{j+1} = \rho_j + h\left(\nabla^2\rho_j + \nabla\left(\rho_j\nabla\frac{\delta\beta\mathcal{F}_{\text{ex}}}{\delta\rho_j}\right)\right). \tag{6.12}$$

The reason we use this method is that it was found that the stiffness of DDFT equation is due to the diffusion term while the divergence is due to the term $1/(1-n_3)$ in the excess term. We may control these two different issues by separating the equation in to ideal and excess parts.

3. **Semi–implicit scheme:** In this scheme the free energy functional is split into ideal and excess parts like before but the difference is that the derivatives are evaluated in Fourier space instead of real space. The gradient operator in Fourier space equals $\widetilde{\nabla} = -i\mathbf{k}$. Note that here $i = \sqrt{-1}$ is the imaginary

unit. Equation (6.11) in Fourier space takes the form

$$\frac{\widetilde{\rho}_{j+1}-\widetilde{\rho}_j}{h} = \underbrace{-k^2\widetilde{\rho}_{j+1}}_{\text{implicit}} \underbrace{-i\mathbf{k}\cdot\left(\rho_j\widetilde{\nabla\frac{\delta\beta\mathcal{F}_{\text{ex}}}{\delta\rho_j}}\right)}_{\text{explicit}}. \tag{6.13}$$

Note that the second term of the r.h.s of Equation (6.13) is evaluated at t_j while the first term is evaluated at the later time t_{j+1}. Now we can solve the equation for ρ_{j+1}

$$\widetilde{\rho}_{j+1} = \frac{\widetilde{\rho}_j - ih\mathbf{k}\cdot\left(\rho_j\widetilde{\nabla\frac{\delta\beta\mathcal{F}_{\text{ex}}}{\delta\rho_j}}\right)}{1+hk^2}. \tag{6.14}$$

In order to solve the DDFT equation in the semi–implicit scheme, we need to calculate $\widetilde{\rho}_{j+1}$ in Fourier space and back transform it into real space in each iteration step in the Euler method. The first order derivative in Fourier space is obtained by

$$\begin{aligned}\widetilde{\nabla} &= \sum_{j=1}^{3}\widetilde{\nabla}_j\,\hat{q}_j \\ &= \sum_{j=1}^{3}\frac{-i\,\sin(k_j\mathrm{d}x_j)}{\mathrm{d}x_j}\,\hat{q}_j,\end{aligned} \tag{6.15}$$

where in the limit of a very fine discretization, $\mathrm{d}r=(\mathrm{d}x,\mathrm{d}y,\mathrm{d}z)\to 0$, it takes the familiar form

$$\begin{aligned}\widetilde{\nabla} &= \lim_{\mathrm{d}r\to 0}\sum_{j=1}^{3}\frac{-i\,\sin(k_j\mathrm{d}x_j)}{\mathrm{d}x_j}\,\hat{q}_j \\ &= -i\,\mathbf{k}\,.\end{aligned} \tag{6.16}$$

By taking the non–perfect numerical discretization into account, we may use relations

$$\widetilde{\nabla} = \sum_{j=1}^{3}\frac{-i\,\sin(k_j\mathrm{d}x_j)}{\mathrm{d}x_j}\,\hat{q}_j, \tag{6.17}$$

$$\widetilde{\nabla}^2 = \sum_{j=1}^{3}\frac{-\sin^2(k_j\mathrm{d}x_j)}{\mathrm{d}x_j^2}, \tag{6.18}$$

for the gradient and Laplace operators in our numerical calculations as well.

If we consider $\mathcal{F}_{\text{ex}} = 0$, Equation (6.1) reduces to the heat or diffusion equation. For this problem explicit method I provides the most exact results (exact up to the order of 10^{-5} in the free energy) for the fcc crystal structure. Figure 6.3 shows the time evolutions of the free energy and maximum value of n_3 for a fcc crystal.

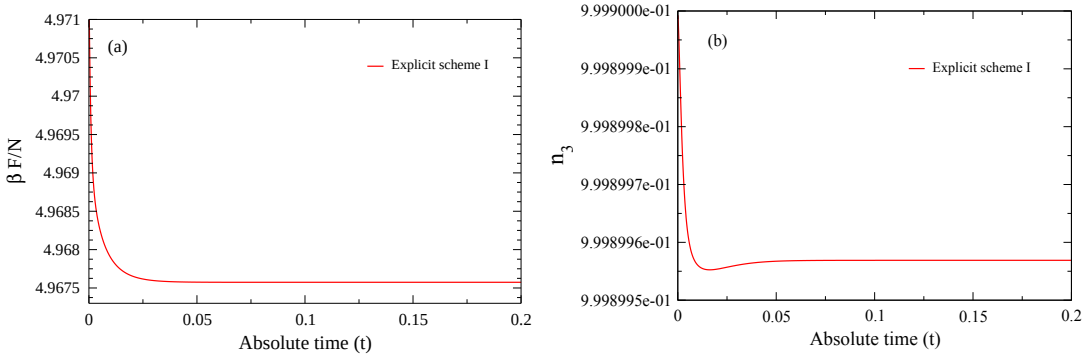

FIGURE 6.3: (a) shows the convergence of the free energy as a function of absolute time for the fcc crystal for bulk density $\rho_b = 1.04$ and vacancy concentration $n_{\text{vac}} = 10^{-4}$. Free energy converged to $F_{\text{DDFT}}/N = 4.967574$ while the free energy obtained from DFT equals $F_{\text{DFT}}/N = 4.967573$. (b) shows the evolution of the maximum value of n_3 vs. absolute time.

The semi–implicit method is more stable for larger time steps ($h < 0.01$). The maximum time steps for explicit methods I and II are $h \sim 10^{-3}$ and $h \sim 2 \times 10^{-4}$ respectively. Explicit methods II also shows an stable behavior but its accuracy is of the order of 10^{-4} in the free energy. For the full functional, $\mathcal{F} = \mathcal{F}_{\text{id}} + \mathcal{F}_{\text{ex}}$, the semi–implicit method becomes unstable while the other two methods are still stable for not too big time steps ($h < 10^{-4}$).

In the case of crystal–liquid interface problem the explicit method II works much better than the other two methods and we can iterate the interface for a while but the full convergence is not reached. All the three numerical schemes show a same instability behavior. The n_3 oscillates at its peaks and the last peak in the crystal side (the peak close to the interface) exceeds one and the iteration diverges.

Appendix A

Mathematical Proof of DFT: Existence of the Energy Functional

The density functional approach focuses on functionals of $\rho(\mathbf{r})$ rather than V_{ext}. Although it is cleat that $\rho(\mathbf{r})$ is a functional of V_{ext}, one can prove [4, 6, 135, 136] the less obvious result that for given V_N, T and μ the probability density is uniquely determined by $\rho(\mathbf{r})$–the latter fixes V_{ext}. In the following the Hohenberg–Kohn–Mermin theorems will be proved which are the two key results of density functional theorem which explain the one–to–one relationship between density and external potential[1].

Consider a hamiltonian function of N–particle system

$$\begin{aligned} \mathcal{H}_N &= K_N + V_N + V_{\text{ext}} \\ &= \sum_{i=1}^{N} \frac{\mathbf{p}_i^2}{2m} + V_N(\mathbf{r}_1, \ldots, \mathbf{r}_n) + \sum_{i=1}^{N} V_{\text{ext}}\,, \end{aligned} \tag{A.1}$$

where K_N is the kinetic energy and V_N and V_{ext} are internal and external potentials respectively. We use a simplified notation in which

$$\text{Tr}_{\text{cl}} \ldots \equiv \sum_{N=0}^{\infty} \frac{1}{h^{3N} N!} \int \int \ldots \mathrm{d}\mathbf{r}^N \mathrm{d}\mathbf{p}^N. \tag{A.2}$$

[1] This appendix is based on Appendix B of Ref [22].

This operation is called the "classical trace", by analogy with the corresponding operation in quantum statistical mechanics. The definition of the grand partition function Ξ and the normalization of the equilibrium phase–space probability density f_0 can be expressed in the compact form

$$\Xi = \mathrm{Tr}_{\mathrm{cl}} \exp\left(-\beta(\mathcal{H}_N - \mu N)\right), \tag{A.3}$$

$$\mathrm{Tr}_{\mathrm{cl}} f_0 = 1. \tag{A.4}$$

Lemma. *Let f be a normalized phase–space probability density and let $\Omega[\rho]$ be the trial functional for the grand free energy defined as*

$$\Omega[f_N] = \mathrm{Tr}_{\mathrm{cl}}[f_N(\mathcal{H}_N - \mu N + \beta^{-1}\log(f_N))]. \tag{A.5}$$

Then this functional has two important properties

1. $\Omega[f_0] = \Omega$: *grand free energy of a system in the equilibrium distribution f_0 is just the grand potential of the system.*

2. $\Omega[f_N \neq f_0] > \Omega$: *for other distributions the functional reduces to a number larger than the grand potential.*

PROOF

1. For the equilibrium distribution the grand free energy functional takes the form

$$\Omega[f_0] = \mathrm{Tr}_{\mathrm{cl}}[f_0(\mathcal{H}_N - \mu N + \beta^{-1}\log(f_0))], \tag{A.6}$$

using Equation (2.34) we know $\log f_0 = -\log(\Xi) - \beta(\mathcal{H} - \mu N)$. By inserting $\log(f_0)$ into (A.6) we obtain

$$\begin{aligned} \Omega[f_0] &= \mathrm{Tr}_{\mathrm{cl}}[f_0(\mathcal{H}_N - \mu N - \beta^{-1}\log(\Xi) - (\mathcal{H} - N\mu N))] \\ &= \mathrm{Tr}_{\mathrm{cl}}[f_0(-\beta^{-1}\log(\Xi))]. \end{aligned} \tag{A.7}$$

Since the partitions sum Ξ is just a number, we can take it out of the classical trace, so

$$\Omega[f_0] \quad = \quad -\beta^{-1}\log(\Xi)\,\mathrm{Tr_{cl}}[f_0]. \tag{A.8}$$

f_0 is a normalized distribution function, therefore

$$\Omega[f_0] \quad = \quad -\beta^{-1}\log(\Xi) = \Omega, \tag{A.9}$$

which is equal to the grand potential of the system.

2. In the second part of the proof we want to show that for other distributions than equilibrium distribution the free energy functional is larger that the grand potential. suppose $f \neq f_0$, then the grand free energy functional reads

$$\Omega[f] = \mathrm{Tr_{cl}}[f(\mathcal{H}_N - \mu N + \beta^{-1}\log(f))]. \tag{A.10}$$

From the first part of the proof we know

$$\log(f_0) = -\log(\Xi) - \beta(\mathcal{H}_N - \mu N), \tag{A.11}$$

$$\longrightarrow \quad \mathcal{H}_N - \mu N = -\beta^{-1}\log(f_0) + \Omega. \tag{A.12}$$

By substituting (A.12) into the Equation (A.10) we obtain

$$\begin{aligned}\Omega[f] &= \mathrm{Tr_{cl}}[f(-\beta^{-1}\log(f_0) + \Omega + \beta^{-1}\log(f))] \\ &= \Omega + \beta^{-1}\mathrm{Tr_{cl}}[f(\log(f) - \log(f_0))].\end{aligned} \tag{A.13}$$

$\beta^{-1}\mathrm{Tr_{cl}}[f(\log(f)-\log(f_0))]$ is always larger that zero and the inequality is thereby verified

$$\Omega[f_N \neq f_0] > \Omega. \tag{A.14}$$

Theorem 1. *For the system with given temperature T, volume V and chemical potential μ, the intrinsic free energy functional*

$$\mathcal{F}[\rho^{(1)}] = \mathrm{Tr_{cl}}[f_0(K_N + V_N + k_B T\log f_0)], \tag{A.15}$$

is a unique functional of the equilibrium one–body density $\rho^{(1)}(\mathbf{r})$.

PROOF. The equilibrium probability distribution f_0 is a functional of external potential V_{ext}. Therefore the single–particle density $\rho^{(1)}(\mathbf{r}) = \text{Tr}_{\text{cl}}(f_0\rho(\mathbf{r}))$ also depends on V_{ext}, where $\rho(\mathbf{r})$ is the microscopic density. Consider two different external potentials $V_{\text{ext}} \neq V'_{\text{ext}}$ give rise to the same density $\rho^{(1)}(\mathbf{r})$. With the hamiltonian $\mathcal{H}' = K_N + V_N + V'_{\text{ext}}$ we may associate probability distribution $f'_0 (\neq f_0)$ and grand potential Ω'. The Inequality (A.14) implies that

$$\begin{aligned} \Omega' &= \text{Tr}_{\text{cl}}[f'_0(\mathcal{H}' - \mu N + k_B T \log f'_0)] \\ &< \text{Tr}_{\text{cl}}[f_0(\mathcal{H}' - \mu N + k_B T \log f_0)] \\ &= \Omega + \text{Tr}_{\text{cl}}[f_0(V'_{\text{ext}} - V_{\text{ext}})], \end{aligned} \tag{A.16}$$

or

$$\Omega' < \Omega + \int \rho^{(1)}(\mathbf{r})[V'_{\text{ext}} - V_{\text{ext}}]\,\mathrm{d}\mathbf{r}. \tag{A.17}$$

If the same argument is carried through with primed and unprimed quantities interchanged, we find that

$$\Omega < \Omega' + \int \rho^{(1)}(\mathbf{r})[V_{\text{ext}} - V'_{\text{ext}}]\,\mathrm{d}\mathbf{r}. \tag{A.18}$$

Addition of the inequalities (A.17) and (A.18) term by term leads to a contradiction

$$\Omega + \Omega' < \Omega' + \Omega, \tag{A.19}$$

showing that the assumption concerning $\rho^{(1)}(\mathbf{r})$ must be false. We therefore conclude that there is only one external potential gives rise to a particular single–particle density. Since f_0 is a functional of V_{ext}, it follows that it is also a unique functional of $\rho^{(1)}(\mathbf{r})$. This in turn implies that the intrinsic free energy (A.15) is a unique functional of $\rho^{(1)}(\mathbf{r})$ and that its functional form is the same for all external potentials.

Theorem 2. *Let* $n(\mathbf{r})$ *be some average of the microscopic density* $\rho(\mathbf{r})$. *Then the functional*

$$\Omega''[n] = \mathcal{F}[n] + \int n(\mathbf{r}) V_{\text{ext}}\,\mathrm{d}\mathbf{r} - \mu \int n(\mathbf{r})\,\mathrm{d}\mathbf{r}, \tag{A.20}$$

has its minimum value when $n(\mathbf{r})$ *is equal to the equilibrium single–particle density* $\rho^{(1)}(\mathbf{r})$.

PROOF. Consider $n(\mathbf{r})$ is the single–particle density associated with a distribution function f'. Therefore the corresponding grand potential takes the form

$$\begin{aligned} \Omega[f'] &= \mathrm{Tr}_{\mathrm{cl}}[f'(\mathcal{H} - \mu N + \beta^{-1}\log(f'))] \\ &= \mathcal{F}[n] + \int n(\mathbf{r}) V_{\mathrm{ext}}\, \mathrm{d}\mathbf{r} - \mu \int n(\mathbf{r})\, \mathrm{d}(r) = \Omega''[n]. \end{aligned} \tag{A.21}$$

According to the inequality (A.14), $\Omega[f_0] \leq \Omega[f']$. It is also clear that $\Omega''[\rho^{(1)}] = \Omega[f_0] = \Omega$. Therefore $\Omega''[\rho^{(1)}] \leq \Omega''[n]$, this means the functional $\Omega''[n]$ is minimized when $n(\mathbf{r}) = \rho^{(1)}(\mathbf{r})$ and its minimum value is equal to the grand potential.

Appendix B

Numerical Approach for FMT Formalism

In this appendix the numerical approach for solving the density functional theory of FMT for liquids and crystals is introduced in detail. According to the basic theorem of DFT, the equilibrium density profile $\rho_{\mathrm{eq}}(\mathbf{r})$ is determined via minimizing the grand canonical free energy functional (3.2) which leads to the following equation

$$\frac{\delta \mathcal{F}_{\mathrm{ex}}[\rho]}{\delta \rho} + \beta^{-1} \log(\Lambda^3 \rho(\mathbf{r})) + V_{\mathrm{ext}}(\mathbf{r}) - \mu = 0, \tag{B.1}$$

where the excess free energy functional has the form (3.30)

$$\beta \mathcal{F}_{\mathrm{ex}}[\rho] = \int \mathrm{d}\mathbf{r}\, \Phi(\{n_\alpha(\mathbf{r})\}). \tag{B.2}$$

Here $\Phi(\{n_\alpha(\mathbf{r})\})$ is the excess free energy density and has different functional forms related to different approximations (see Section 3.3). The free energy density Φ is itself a function of weighted densities $\{\mathbf{n}_\alpha(\mathbf{r})\} = \{n_0, n_1, n_2, n_3, \mathbf{n}_1, \mathbf{n}_2, n^t\}$. These weighted densities are determined from the density profile $\rho(\mathbf{r})$ as follows

$$n_\alpha = \int \mathrm{d}\mathbf{r}'\, \rho(\mathbf{r}') \omega^\alpha(\mathbf{r} - \mathbf{r}') = \rho \otimes \omega^\alpha, \tag{B.3}$$

and here ω^α are specific weight functions ((3.28) and (3.42))

$$\begin{aligned}
\omega^3(\mathbf{r}) &= \Theta(R-r)\ , \\
\omega^2(\mathbf{r}) &= \delta(R-r)\ , \\
\omega^1(\mathbf{r}) &= \omega^2(\mathbf{r})/(4\pi R)\ , \\
\omega^0(\mathbf{r}) &= \omega^2(\mathbf{r})/(4\pi R^2)\ , \\
\boldsymbol{\omega}^2(\mathbf{r}) &= \mathbf{r}/r\ \delta(R-r)\ , \\
\boldsymbol{\omega}^1(\mathbf{r}) &= \boldsymbol{\omega}^2/(4\pi R) \\
\omega^t_{ij}(\mathbf{r}) &= r_i r_j/\mathbf{r}^2\ \delta(R-r)\ .
\end{aligned} \tag{B.4}$$

Having known the weighted densities, we are able to calculate the free energy density function Φ and respectively the free energy functional. If we calculate the derivative of free energy with respect to density, $\partial\mathcal{F}_{\text{ex}}/\partial\rho$, we have all ingredients to solve the Equation (B.1) iteratively.

In the program, the density profile ρ and 11 weighted densities (two scalar densities n_3, n_2, three vector densities, $\mathbf{n}_{2,i}$, $i = x, y, z$, and six tensor densities, n^t_{ij}) need to be discretized on a three dimensional grid covering the cuboid boxes. Section B.1 explains in detail how to calculate the weighted densities. Convolutions in real space are multiplications in Fourier space. The necessary convolutions are computed using Fast Fourier Transformations. We use the FFTW 3.3 library for parallelized Fast Fourier Transforms. The other parts of the code are parallelized through OpenMP. To have a more efficient algorithm, the iteration of Eq. (B.1) is done using a combination of Picard steps and DIIS steps (Discrete Inversion in Iterative Subspace) [137]. See Appendix C to find more details on the iteration methods used in this thesis.

B.1 Weighted Densities

The first step for solving the Euler–Lagrange equation (B.1) is to evaluate the weighted densities. Weighted densities, n_α, are just convolutions of the density $\rho(\mathbf{r})$ and weight functions ω^α. Convolutions in real space are normal multiplication in Fourier space. To evaluate the weighted densities in real space, one may calculate the product of the Fourier transformed density and weight functions and then Fourier transform it back

into real space

$$n_\alpha = \mathrm{FT}^{-1}\left(\mathrm{FT}(\rho(\mathbf{r})) \times \mathrm{FT}(\omega^\alpha(\mathbf{r}))\right), \tag{B.5}$$

which FT denotes forward Fourier transformation and FT^{-1} denotes the inverse (backward) Fourier transformation. Fourier transform of the density, $\tilde{\rho}(\mathbf{k})$, is calculated numerically using FFTW library[1] and Fourier transforms of the weight functions are calculated analytically. The explicit form of the weight functions in Fourier space are

$$\begin{aligned}
\tilde{\omega}^3(\mathbf{k}) &= \frac{4\pi}{k^3(2\pi)^{3/2}}\left(\sin(kR) - kR\cos(kR)\right), \\
\tilde{\omega}^2(\mathbf{k}) &= \frac{4\pi R}{k(2\pi)^{3/2}}\sin(kR), \\
\tilde{\omega}^1(\mathbf{k}) &= \frac{\tilde{\omega}^2(\mathbf{k})}{4\pi R}, \\
\tilde{\omega}^0(\mathbf{k}) &= \frac{\tilde{\omega}^2(\mathbf{k})}{4\pi R^2}, \\
\tilde{\boldsymbol{\omega}}^2(\mathbf{k}) &= -i\mathbf{k}\tilde{\omega}^3(\mathbf{k}), \\
\tilde{\boldsymbol{\omega}}^1(\mathbf{k}) &= \frac{\tilde{\boldsymbol{\omega}}^1(\mathbf{k})}{4\pi R}, \\
\tilde{\omega}^t(\mathbf{k}) &= \left(\tilde{\omega}^2(\mathbf{k}) - \frac{3}{R}\tilde{\omega}^3(\mathbf{k})\right)\left(\frac{\mathbf{k}\cdot\mathbf{k}^{\mathrm{T}}}{k^2} - \frac{\mathbb{I}}{3}\right),
\end{aligned} \tag{B.6}$$

where $\mathbf{k} = (k_x, k_y, k_z)$ is the reciprocal lattice vector, R is the diameter of hard spheres and $\mathbf{k}^{\mathrm{T}}$ denotes the transpose of the vector $\mathbf{k}$. Explicit calculations of Fourier transformations of weight functions are presented in the following subsections. In the limit of $k \to 0$ the Fourier transforms of weight functions take the form

$$\begin{aligned}
\tilde{\omega}^3(\mathbf{k}) &= \frac{1}{(2\pi)^{3/2}}\frac{4\pi R^3}{3}, \\
\tilde{\omega}^2(\mathbf{k}) &= \frac{4\pi R^2}{(2\pi)^{3/2}}, \\
\tilde{\omega}^1(\mathbf{k}) &= \frac{R}{(2\pi)^{3/2}}, \\
\tilde{\omega}^0(\mathbf{k}) &= \frac{1}{(2\pi)^{3/2}}, \\
\tilde{\boldsymbol{\omega}}^2(\mathbf{k}) &= 0, \\
\tilde{\boldsymbol{\omega}}^1(\mathbf{k}) &= 0, \\
\tilde{\omega}^t(\mathbf{k}) &= 0\mathbb{I}.
\end{aligned} \tag{B.7}$$

[1]The Fastest Fourier Transform in the West (FFTW) is a software library for computing discrete Fourier transforms which has been developed at the Massachusetts Institute of Technology (MIT) [138, 139].

B.1.1 Fourier Transform of the Scalar Weight Function ω^3

The problem of calculating the Fourier transform of ω^3 is nothing than finding the Fourier transform of the Heaviside step function

$$\omega^3(\mathbf{r}) = \Theta(R - |\mathbf{r}|). \tag{B.8}$$

Applying the Fourier transformation on ω^3 yield

$$\tilde{\omega}^3(\mathbf{k}) = \frac{1}{(2\pi)^{3/2}} \int \Theta(R - |\mathbf{r}|) e^{-i\mathbf{k}\cdot\mathbf{r}} \, \mathrm{d}\mathbf{r}. \tag{B.9}$$

It is more convenient to perform the integration in the spherical coordinates, therefore

$$\begin{aligned}
\tilde{\omega}^3(\mathbf{k}) &= \frac{1}{(2\pi)^{3/2}} \int_0^R \int_0^\pi \int_0^{2\pi} r^2 \sin(\theta) e^{-i\mathbf{k}\cdot\mathbf{r}} \, \mathrm{d}\mathbf{r} \, \mathrm{d}\theta \, \mathrm{d}\phi \\
&= \frac{2\pi}{(2\pi)^{3/2}} \int_0^R \int_0^\pi r^2 \sin(\theta) e^{-ikr\cos(\theta)} \, \mathrm{d}\mathbf{r} \, \mathrm{d}\theta \\
&= \frac{2\pi}{(2\pi)^{3/2}} \int_0^R \frac{r}{ik} \left(e^{ikr} - e^{-ikr} \right) \, \mathrm{d}\mathbf{r} \\
&= \frac{2\pi}{(2\pi)^{3/2}} \int_0^R \frac{2r}{k} \sin(kr) \, \mathrm{d}\mathbf{r},
\end{aligned} \tag{B.10}$$

and the integral can be evaluated using the relation $\partial/\partial x[\sin(kx) - kx\cos(kx)] = k^2 x \sin(kx)$

$$\tilde{\omega}^3(\mathbf{k}) = \frac{4\pi}{k^3(2\pi)^{3/2}} \left(\sin(kR) - kR\cos(kR) \right). \tag{B.11}$$

B.1.2 Fourier Transform of the Scalar Weight Function ω^2

Similar to the transformation of ω^3 in the latter subsection we use the spherical coordinates as well for calculating $\tilde{\omega}^2$

$$\begin{aligned}
\tilde{\omega}^2(\mathbf{k}) &= \frac{1}{(2\pi)^{3/2}} \int \delta(R - |\mathbf{r}|) e^{-i\mathbf{k}\cdot\mathbf{r}} \, \mathrm{d}\mathbf{r} \\
&= \frac{1}{(2\pi)^{3/2}} \int_0^\pi \int_0^{2\pi} R^2 \sin(\theta) e^{-i\mathbf{k}\cdot\mathbf{R}} \, \mathrm{d}\theta \, \mathrm{d}\phi \\
&= \frac{2\pi}{(2\pi)^{3/2}} \int_0^\pi R^2 \sin(\theta) e^{-ikR\cos(\theta)} \, \mathrm{d}\theta \\
&= \frac{4\pi R}{k(2\pi)^{3/2}} \sin(kR).
\end{aligned} \tag{B.12}$$

B.1.3 Fourier Transform of the Vectorial Weight Function $\boldsymbol{\omega}^2$

In this subsection the Fourier transform of $\tilde{\boldsymbol{\omega}}^2 = \frac{\mathbf{r}}{r}\delta(R - |\mathbf{r}|)$ is calculated. The transformation reads

$$\tilde{\boldsymbol{\omega}}^2(\mathbf{k}) = \frac{1}{(2\pi)^{3/2}} \int \frac{\mathbf{r}}{r}\delta(R - |\mathbf{r}|)e^{-i\mathbf{k}\cdot\mathbf{r}}\,\mathrm{d}\mathbf{r}, \tag{B.13}$$

where $\mathbf{r}$ in the spherical coordinate system is

$$\mathbf{r} = \begin{pmatrix} r_x \\ r_y \\ r_z \end{pmatrix} = r \begin{pmatrix} \cos(\phi)\sin(\theta) \\ \sin(\phi)\sin(\theta) \\ \cos(\theta) \end{pmatrix}. \tag{B.14}$$

For simplicity the coordinate system is rotated in such a way that $\mathbf{k}$ lies on the z–axis, therefore $\tilde{\boldsymbol{\omega}}^2$ takes the form

$$\begin{aligned} \tilde{\boldsymbol{\omega}}^2(\mathbf{k}) &= \frac{1}{(2\pi)^{3/2}} \int_0^\infty \int_0^\pi \int_0^{2\pi} r^2 \sin(\theta)\, \frac{\mathbf{r}}{r}\delta(R - \mathbf{r}|)e^{-i\mathbf{k}\cdot\mathbf{r}}\,\mathrm{d}\mathbf{r}\,\mathrm{d}\theta\,\mathrm{d}\phi \\ &= \frac{1}{(2\pi)^{3/2}} \int_0^\pi \int_0^{2\pi} R^2 \sin(\theta) \begin{pmatrix} \cos(\phi)\sin(\theta) \\ \sin(\phi)\sin(\theta) \\ \cos(\theta) \end{pmatrix} e^{-ikR\cos(\theta)}\,\mathrm{d}\theta\,\mathrm{d}\phi. \end{aligned} \tag{B.15}$$

Integrals of $\cos(\phi)$ and $\sin(\phi)$ over a complete period are zero, so the only remaining term is $\hat{e}_z$ component and the integral reduces to[2]

$$\begin{aligned} \tilde{\boldsymbol{\omega}}^2(\mathbf{k}) &= \frac{2\pi R^2}{(2\pi)^{3/2}} \int_0^\pi \sin(\theta)\cos(\theta) e^{-ikR\cos(\theta)}\,\mathrm{d}\theta \\ &= -i\mathbf{k}\frac{4\pi}{k^3(2\pi)^{3/2}} \left(\sin(kR) - kR\cos(kR)\right) \\ &= -i\mathbf{k}\tilde{\boldsymbol{\omega}}^3(\mathbf{k}). \end{aligned} \tag{B.16}$$

[2] In the last step of integration we use the relation $\int_0^\pi \sin(\alpha)\cos(\alpha)e^{-ix\cos(\alpha)}\,\mathrm{d}\alpha = \frac{2i}{x^2}(x\cos(x) - \sin(x))$.

B.1.4 Fourier Transform of the Tensorial Weight Function $\boldsymbol{\omega}^t$

The Fourier transform of the tensorial weight function is obtained by

$$\tilde{\omega}^t(\mathbf{k}) = \frac{1}{(2\pi)^{3/2}} \int \left(\frac{\mathbf{r}.\mathbf{r}^T}{r^2} - \frac{\mathbb{I}}{3} \right) \delta(R - |\mathbf{r}|) e^{-i\mathbf{k}\cdot\mathbf{r}} \, \mathrm{d}\mathbf{r}. \tag{B.17}$$

The integral is evaluated in the spherical coordinates which the z–axis is aligned with the vector $\mathbf{k}$. Equation (B.17) can be split into two terms

$$\tilde{\omega}^t(\mathbf{k}) = \underbrace{\frac{1}{(2\pi)^{3/2}} \int \frac{\mathbf{r}.\mathbf{r}^T}{r^2} \delta(R - |\mathbf{r}|) e^{-i\mathbf{k}\cdot\mathbf{r}} \, \mathrm{d}\mathbf{r}}_{\mathrm{I}} - \underbrace{\frac{1}{(2\pi)^{3/2}} \int \frac{\mathbb{I}}{3} \delta(R - |\mathbf{r}|) e^{-i\mathbf{k}\cdot\mathbf{r}} \, \mathrm{d}\mathbf{r}}_{\mathrm{II}}. \tag{B.18}$$

The Fourier transform of the term II is already known form Section B.1.2

$$\mathrm{II} = \frac{\mathbb{I}}{3} \tilde{\omega}^2(\mathbf{k}), \tag{B.19}$$

and part I can be calculated as following

$$\begin{aligned}
\mathrm{I} &= \frac{1}{(2\pi)^{3/2}} \int \frac{\mathbf{r}.\mathbf{r}^T}{r^2} \delta(R - |\mathbf{r}|) e^{-i\mathbf{k}\cdot\mathbf{r}} \, \mathrm{d}\mathbf{r} \\
&= \frac{1}{(2\pi)^{3/2}} \int_\infty^R \int_0^\pi \int_0^{2\pi} r^2 \sin(\theta) \frac{\mathbf{r}.\mathbf{r}^T}{r^2} \delta(R - |\mathbf{r}|) e^{-i\mathbf{k}\cdot\mathbf{r}} \, \mathrm{d}\mathbf{r} \, \mathrm{d}\theta \, \mathrm{d}\phi \\
&= \frac{R^2}{(2\pi)^{3/2}} \int_0^\pi \int_0^{2\pi} \sin(\theta) \frac{\mathbf{r}.\mathbf{r}^T}{r^2} e^{-ikR\cos(\theta)} \, \mathrm{d}\theta \, \mathrm{d}\phi \, .
\end{aligned} \tag{B.20}$$

The only term in the integrand which depends on variable ϕ is $\mathbf{r} \cdot \mathbf{r}^T$, thus

$$\begin{aligned}
&\int_0^{2\pi} \sin(\theta) \frac{\mathbf{r}.\mathbf{r}^T}{r^2} \, \mathrm{d}\phi \\
&= \int_0^{2\pi} \sin(\theta) \begin{pmatrix} \cos(\phi)\sin(\theta) \\ \sin(\phi)\sin(\theta) \\ \cos(\theta) \end{pmatrix} \cdot \begin{pmatrix} \cos(\phi)\sin(\theta) \\ \sin(\phi)\sin(\theta) \\ \cos(\theta) \end{pmatrix}^T \mathrm{d}\phi \\
&= \begin{pmatrix} \pi\sin^3(\theta) & 0 & 0 \\ 0 & \pi\sin^3(\theta) & 0 \\ 0 & 0 & 2\pi\sin(\theta)\cos^2(\theta) \end{pmatrix} \\
&= 2\pi\sin(\theta)\hat{e}_z \cdot \hat{e}_z^T + \pi\sin^3(\theta)\left(\mathbb{I} - 3\hat{e}_z \cdot \hat{e}_z^T\right).
\end{aligned} \tag{B.21}$$

Therefore we have

$$\begin{aligned} \mathrm{I} &= \frac{R^2}{(2\pi)^{3/2}} \int_0^{\pi} \left(2\pi \sin(\theta)\hat{e}_z \cdot \hat{e}_z^T + \pi \sin^3(\theta)\left(\mathbb{I} - 3\hat{e}_z \cdot \hat{e}_z^T\right)\right) e^{-ikR\cos(\theta)}\, \mathrm{d}\theta \\ &= \tilde{\omega}^2(\mathbf{k})\frac{\mathbf{k}\cdot\mathbf{k}^T}{k^2} - \frac{\tilde{\omega}^3(\mathbf{k})}{R}\left(3\frac{\mathbf{k}\cdot\mathbf{k}^T}{k^2} - \mathbb{I}\right). \end{aligned} \tag{B.22}$$

By substituting (B.19) and (B.22) in to the Equation (B.18) $\tilde{\omega}^t$ is obtained

$$\tilde{\omega}^t(\mathbf{k}) = \left(\tilde{\omega}^2(\mathbf{k}) - \frac{3}{R}\tilde{\omega}^3(\mathbf{k})\right)\left(\frac{\mathbf{k}\cdot\mathbf{k}^{\mathrm{T}}}{k^2} - \frac{\mathbb{I}}{3}\right). \tag{B.23}$$

Appendix C

Numerical Iterations and their Stabilities

In general there are two methods to solve an equation; direct and iterative methods. Direct methods compute the solution to a problem in a finite number of steps. These methods will give the precise answer if they are performed in infinite precision arithmetic (examples include Gaussian elimination and the simple method of linear programming). In practice, a finite precision is used and the result is an approximation of the true solution (assuming stability). In contrast to direct methods, iterative methods are not expected to terminate in a finite number of steps. Starting from an initial guess, iterative methods form successive approximations that converge to the exact solution only in the limit. A convergence test, often involving the residual, is specified in order to decide when a sufficiently accurate solution has (hopefully) been found. Even using infinite precision arithmetic these methods would not reach the solution within a finite number of steps (in general). Examples include Picard's methods (or the method of successive approximations) and Newton's method and Jacobi iteration. In computational matrix algebra, iterative methods are more common than direct methods in numerical analysis and generally are needed for large problems.

C.1 Picard Iteration

The Picard iteration scheme which was introduced by Charles Émile Picard (1856–1941) provides a unique solution for a continuous function which satisfies the Lipschitz[1] continuity[140]. Lipschitz continuity is a strong form of uniform continuity for functions and intuitively, a Lipschitz continuous function is limited in how fast it can vary. According to the Picard's existence theorem[2] if f is a continuous function that satisfies the Lipschitz conditions

$$|f(x,t) - f(y,t)| \leq L|x-y|, \tag{C.1}$$

in a surrounding of $(x_0, t) \in \Omega \subset \mathbb{R}^n \times \mathbb{R} = \{(x,t) : |x - x_0| < b, |t - t_0| < a\}$, then the differential equation

$$\begin{aligned} \frac{dx}{dt} &= f(x,t), \\ x(t_0) &= x_0, \end{aligned} \tag{C.2}$$

has a unique solution $x(t)$ in the interval $|t - t_0| < d$, where $d = \min(a, b/B)$. min denotes the minimum and $B = \sup|f(x,t)|$ where sup denotes the supremum. An iterative problem may take the mathematical form as follows

$$Af = f, \tag{C.3}$$

where f is a real function and A is a nonlinear operator in a functional space [141]. One can use the simple Picard iteration method to solve Equation (C.2) starting with an initial guess f_1

$$f_{n+1} = Af_n, \qquad n = 1, 2 \ldots. \tag{C.4}$$

Equation (C.4) generates a sequence of functions $f_1, f_2, \ldots$. If the sequence converges uniformly, the limiting element is the unique solution of Equation (C.2). Practically, sometimes the iterative procedure (C.4) is unstable and oscillates or even diverges. This problem can be treated by mixing the new function f_{n+1} with the previous one, f_n, in

[1] Rudolf Lipschitz (1832–1903).
[2] It is also called the Picard–Lindelöf theorem or Cauchy–Lipschitz theorem.

order to decrease the amount of the change of f_n in each iteration

$$f_{n+1} = \alpha\, A f_n + (1-\alpha) f_n, \tag{C.5}$$

where $\alpha \in [0,1]$ is the mixing parameter and must be determined empirically. The α should be choose large enough for fast convergence but not too large to leads any instability in the iteration procedure. One may also change the value of mixing parameter during the iteration by monitoring the behavior of the convergence parameter. If the iteration is converging, the mixing parameter can be slowly increased. One may also profit mathematical approaches to approximate the upper limit of the mixing parameter to speed up the convergence (see Appendix C.4).

The Picard iteration usually converges very slowly and the enormous speed up can be obtained by using the Direct Inversion in the Iterative Subspace (DIIS) method, which is introduced in Appendix C.2.

C.2 Direct Inversion in the Iterative Subspace

Direct Inversion in the Iterative Subspace (DIIS), also known as Pulay mixing was developed by Peter Pulay in the field of computational quantum chemistry with the intent to accelerate and stabilize the iteration of the self–consistent field (SCF) method [142, 143]. DIIS applies direct methods to a linear algebra problem in a subspace formed by taking a set of trial vectors from the full–dimensional space. At a given iteration, the approach constructs a linear combination of approximate error vectors from previous iterations. The coefficients of the linear combination are determined so to best approximate, in a least squares[3] sense, the null vector. The newly determined coefficients are then used to extrapolate the function variable for the next iteration. It is found that DIIS could be useful for accelerating the convergence of SCF procedures and, to a lesser extent, geometry optimizations.

Suppose that we have a set of trial functions f_i which have been generated during the (Picard) iterative solution of a problem. Now let us form a set of *residual* vectors defined

[3]The method of least squares assumes that the best–fit curve of a given type is the curve that has the minimal sum of the deviations squared (least square error) from a given set of data. In other word, "Least squares" means that the overall solution minimizes the sum of the squares of the errors made in the results of every single equation.

as

$$\Delta f_i = f_{i+1} - f_i \,. \tag{C.6}$$

The DIIS method assumes that a good approximation to the final solution f_{final} can be obtained as a linear combination of the previous guess vectors

$$f = \sum_i^m c_i f_i \,, \tag{C.7}$$

where m is the number of previous vectors (in practice, only the most recent few vectors are used). The coefficients c_i are obtained by requiring that the associated residual vector

$$\Delta f = \sum_i^m c_i \, \Delta f_i \,, \tag{C.8}$$

approximates the zero vector in a least–squares sense. Furthermore, the coefficients are required to add to one,

$$\sum_i^m c_i = 1 \,. \tag{C.9}$$

The motivation for the latter requirement can be seen as follows. Each of our trial solutions f_i can be written as the exact solution plus an error term, $f_{\text{final}} + e_i$. Then, the DIIS approximate solution is given by

$$\begin{aligned} f &= \sum_i^m c_i (f_{\text{final}} + e_i) \\ &= f_{\text{final}} \sum_i^m c_i + \sum_i^m c_i e_i \,. \end{aligned} \tag{C.10}$$

Hence, we wish to minimize the actual error, which is the second term in the equation above (of course, in practice, we don't know e_i, only Δf_i); doing so would make the second term vanish, leaving only the first term. For $f = f_{\text{final}}$, we must have $\sum_i^m c_i = 1$.

Thus, we wish to minimize the norm of the residuum vector

$$\langle \Delta f | \Delta f \rangle = \sum_{ij}^m c_i^* c_j \langle \Delta f_i | \Delta f_j \rangle, \tag{C.11}$$

subject to the constraint (C.9). These requirements can be satisfied by minimizing the following function with Lagrangian multiplier λ

$$\mathcal{L} = \mathbf{c}^{\dagger}\mathbf{S}\mathbf{c} - \lambda\left(1 - \sum_{i}^{m} c_i\right), \tag{C.12}$$

where $\mathbf{S}$ is the matrix of overlaps

$$S_{ij} = \langle \Delta f_i | \Delta f_j \rangle. \tag{C.13}$$

We can minimize $\mathcal{L}$ with respect to a coefficient c_k to obtain (assuming real quantities)

$$\frac{\partial \mathcal{L}}{\partial c_k} = 0 \tag{C.14}$$

$$\Rightarrow \sum_{j}^{m} c_j S_{kj} + \sum_{i}^{m} c_i S_{ik} - \lambda = 2\sum_{i}^{m} c_i S_{ki} - \lambda = 0. \tag{C.15}$$

Now we absorb the factor of 2 into λ to obtain the following matrix equation

$$\begin{pmatrix} S_{11} & S_{12} & \dots & S_{1m} & -1 \\ S_{21} & S_{22} & \dots & S_{2m} & -1 \\ \vdots & \vdots & & \vdots & \vdots \\ S_{m1} & S_{m2} & \dots & S_{mm} & -1 \\ -1 & -1 & \dots & -1 & 0 \end{pmatrix} \begin{pmatrix} c_1 \\ c_2 \\ \vdots \\ c_m \\ \lambda \end{pmatrix} = \begin{pmatrix} 0 \\ 0 \\ \vdots \\ 0 \\ -1 \end{pmatrix}. \tag{C.16}$$

On the DIIS minimization, further improvement is possible only after updating the iterative subspace f_i with new vectors introducing new dimensions, which cannot be reduced to a linear combination of the previous ones. They can be obtained by performing several (Picard) iteration from the point of the minimized residual and then repeating the DIIS procedure.

C.3 Euler Method

The Picard scheme is used to solve DFT problems and the DIIS method increases the stability and convergence rate. In the case of DDFT we have a time dependent equation with a given initial value. For this kind of equations one may use Euler method. The Euler method is a first–order numerical procedure for solving the initial value ordinary

differential equations (ODEs). Consider an initial value problem

$$y'(t) = f(y,t), \tag{C.17}$$

with initial condition

$$y(0) = y_0. \tag{C.18}$$

By discretizing the Equation (C.17) it takes the form

$$y_{n+1} = y_n + hf(y_n, t_n), \tag{C.19}$$

which advances a solution from t_n to $t_{n+1} = t_n + h$. Note that the method increments a solution through an interval h while using derivative information from only the beginning of the interval [144]. The accuracy of this method is not too bad and has a reasonable stability as long as the Courant–Friedrichs–Lewy condition is fulfilled [145]. This condition states that, given a space discretization, a time step bigger than some computable quantity should not be taken[4]. This simple method of solving initial value ODEs was called simply *the Euler method* by Press *et al.* in 1992 [146].

C.4 Stability of Iterations

DFT and DDFT problems are usually solved iteratively. For the self–consistent DFT equation we start with an initial guess ρ_0 and improve the guess ρ_i by iteratively applying the simple or more sophisticated version of Picard itteration [46]. The iteration can be optimized by DIIS scheme [147]. For DDFT case, we start with an initial condition $\rho_0 = \rho(0)$ at $t = 0$ and obtain the density profile $\rho_i = \rho(t_i)$ at later times by iteratively applying a suitable mapping like the Euler or Runge–Kutta methods. So structurally the numerical approach is very similar. Both DFT and DDFT ODEs in FMT scheme are quite stiff[5] and Euler and Picard methods have a finite and usually small stability

[4] The Courant–Friedrichs–Lewy condition can be viewed as a sort of discrete "light cone" condition, namely that the time step must be kept small enough so that information has enough time to propagate through the space discretization.

[5] A stiff equation is a differential equation for which certain numerical methods for solving the equation are numerically unstable, unless the stepsize is taken to be extremely small. Actually, Stiffness is an efficiency issue. If we were not concerned with how much time a computation takes, we would not be concerned about stiffness.

region which leads to very small step sizes. During the iteration, the step size should be chosen in such a way to stay in the stability region [148].

The Power Method

The power method is a simple way to find the dominant eigenvector and eigenvalue of a matrix (see e.g. [149]) and it allows us to estimate the spectral radius of the Jacobian of a nonlinear mapping. We can prove the convergence of the method for diagonalized matrices. When the stability region of the numerical method is not known we can estimate the stable step size and convergence rate.

If A is diagonalizable[6] then there exist n independent eigenvectors of A. Let $x_1, \ldots, x_n$ be these eigenvectors, then $x_1, \ldots, x_n$ form a basis of $\mathbb{R}^n$. Hence the initial vector q_0 can be written as

$$q_o = a_1 x_1 + a_2 x_2 + \ldots + a_n x_n, \tag{C.20}$$

where $a_1, \ldots, a_n$ are scalars. By multiplying both sides of the equation in A^k we have

$$\begin{aligned} A^k q_0 &= A^k(a_1 x_1 + a_2 x_2 + \ldots + a_n x_n) \\ &= a_1 A^k x_1 + a_2 A^k x_2 + \ldots + a_n A^k x_n \\ &= a_1 \lambda_1^k x_1 + a_2 \lambda_2^k x_2 + \ldots + a_n \lambda_n^k x_n \\ &= a_1 \lambda_1^k x_1 + a_1 \lambda_1^k \left(\sum_{i=2}^{n} \frac{a_i}{a_1} \left(\frac{\lambda_i}{\lambda_1} \right)^k x_i \right). \end{aligned} \tag{C.21}$$

If $|\lambda_1| > |\lambda_2| \geq \ldots \geq |\lambda_n|$, then $|\lambda_1|$ is the dominant eigenvalue. In the case $\left(\frac{\lambda_i}{\lambda_1}\right)^k \to 0$ and if $a_1 \neq 0$, therefore $A^k q_0 \to a_1 \lambda_1^k x_1$. The power method normalizes the products $Aq^{(k-1)}$ to avoid overflow/underflow, therefore it converges to the normalized x_1 and the *rate of convergence* is *linear* and equals $|\lambda_2|/|\lambda_1|$. One can show that this result also holds when A is not diagonalizable by writing q_0 as a linear combination of the vectors associated with the Schur decomposition of A [149].

Hence we have the dominant eigenvalue of a matrix, we can determine the stability region. To evaluate the spectral radius, we choose an initial guess $f_0 = f(\rho_0)$ and iterate

[6] A matrix $A \in \mathbb{R}^{n \times n}$ is diagonalizable if there exists an invertible matrix X such that $A = XDX^{-1}$ where D is a diagonal matrix

the equation k times as follows

$$\rho_{i+1} = \rho_i + \frac{f(\rho_i) - f(\rho_0)}{\sigma_i}, \tag{C.22}$$

where σ_i is

$$\sigma_i = ||(\rho_i) - f(\rho_0)||_2 \,. \tag{C.23}$$

The σ_i converges to the spectral radius σ. For stable iterations the dominant eigenvalue $|\lambda_1| = \sigma$ scaled with the step size must lie within the stability region

$$h\sigma < |\beta|, \tag{C.24}$$

where h is the step size and β is the minimum of the stability region on the real axis which is depends only on the iteration method. For Euler and Picard methods $\beta = -2$.

Appendix D

One–Particle Volumes for the fcc, hcp and bcc Hard–Sphere Crystals

D.1 fcc and hcp

The one–particle free volume is equal for fcc and hcp and has been given in Ref. [69]. We introduce the nearest neighbor distance $d = 2^{2/3}\rho_0^{-1/3}$. The hard sphere diameter is σ and the formula is valid for densities $\rho_0\sigma^3 \in [1/2, \sqrt{2}]$:

$$\begin{aligned} V_1 &= \frac{20}{3}c^3 - \frac{4}{3}c^2 s - 4c^2\sqrt{\sigma^2 - c^2} + \\ &\quad 2\sqrt{2}(c^3 - 6c\sigma^2)\left(\arcsin\frac{c}{q} + \arcsin m\right) + \\ &\quad 8\sigma^3\left(2\arcsin u + \frac{\pi}{2} - \arcsin w - \arcsin t\right) . \end{aligned} \tag{D.1}$$

with

$$\begin{aligned} c &= d/\sqrt{2} , \\ s &= \sqrt{3\sigma^2 - 2c^2} , \\ q &= \sqrt{2\sigma^2 - c^2} , \\ m &= (c - 2s)/(3q) , \end{aligned}$$

$$
\begin{aligned}
t &= (\sigma^2 + c\sigma - c^2)/(q\sigma) \;, \\
u &= [(2\sigma + c)(\sigma + [2c - s]/3) - (\sigma + c)^2]/[q(\sigma + [2c - s]/3)] \;, \\
w &= (\sigma^2 - c\sigma - c^2)/(q\sigma) \;.
\end{aligned}
$$

D.2 bcc

In case of bcc the free volume is given by an octahedral–like body (see Fig. 4.2) centered in the cubic unit cell. The faces are parts of the surfaces of the exclusion spheres (of radius σ) around the corners of the cubic unit cell. Let $a = (2/\rho_0)^{1/3}$ be the side length of the cubic unit cell. The free volume is then given by

$$
V_1 = 8 \int_0^{z_{\max}} dz \int_0^{x_{\max}} dx \left(\frac{a}{2} - \sqrt{\sigma^2 - \left(\frac{a}{2} - z\right)^2 - \left(\frac{a}{2} - x\right)^2} \right) \;, \tag{D.2}
$$

$$
\begin{aligned}
x_{\max} &= \frac{a}{2} - \sqrt{\sigma^2 - \left(\frac{a}{2} - z\right)^2 - \frac{a^2}{4}} \;, \\
z_{\max} &= \frac{a}{2} - \sqrt{\sigma^2 - \frac{a^2}{2}} \;.
\end{aligned}
$$

$$
\begin{aligned}
= \; & \frac{a^3}{8} + a \left(\frac{3}{2}\sigma^2 - \frac{1}{8}a^2 \right) \left(\arctan \frac{2c}{a} - \frac{\pi}{4} \right) - \\
& \frac{a^2}{4}c + \frac{2}{3}\sigma^3 \left(\arctan \frac{a^2}{4\sigma c} - \arctan \frac{c}{\sigma} \right) \;, \qquad \text{(D.3)} \\
& c = \sqrt{\sigma^2 - a^2/2} \;.
\end{aligned}
$$

Bibliography

[1] D. O'Grady. Introduction to crystallization and precipitation (January 2011). URL http://blog.autochem.mt.com/.

[2] A. Ivlev, H Löwen, G. Morfill and C. P. Royall. *Complex Plasmas and Colloidal Dispersions: Particle–resolved Studies of Classical Liquids and Solids*. World Scientific Singapore (2012).

[3] P. Hohenberg and W. Kohn. *Inhomogeneous electron gas*. Phys. Rev. **136**, B864 (1964).

[4] N. D. Mermin. *Thermal properties of the inhomogeneous electron gas*. Phys. Rev. **137**, A1441 (1965).

[5] C. Ebner, W. F. Saam and D. Stroud. *Density-functional theory of simple classical fluids. i. surfaces*. Phys. Rev. A **14**, 2264 (1976).

[6] R. Evans. *The nature of the liquid-vapour interface and other topics in the statistical mechanics of non-uniform, classical fluids*. Adv. Phys. **28**, 143 (1979).

[7] R. A. L. Jones. *Soft Condensed Matter*. Oxford University Press (2002).

[8] Wikipedia contributors. Phase diagram . URL http://en.wikipedia.org/w/index.php?title=Phase_diagram&oldid=606426630.

[9] G.J. Van Wylen and R.E. Sonntag. *Fundamentals of Classical Thermodynamics, 3rd edition*. John Wiley and Sons (1985).

[10] P. Perrot. *A to Z of Thermodynamics*. Oxford University Press (1998).

[11] J. O. E. Clark. *The Essential Dictionary of Science*. Barnes and Noble (2004).

[12] W. Greiner, L. Neise and H. Stöcker. *Thermodynamics and statistical mechanics.* Springer–Verlag (1995).

[13] B. J. Alder and T. E. Wainwright. *Phase transition for a hard sphere system.* J. Chem. Phys. **27**, 1208 (1957).

[14] W. W. Wood and J. D. Jacobson. *Preliminary results from a recalculation of the monte carlo equation of state of hard spheres.* J. Chem. Phys. **27**, 1207 (1957).

[15] W. G. Hoover and F. H. Ree. *Melting transition and communal entropy for hard spheres.* J. Chem. Phys. **49**, 3609 (1968).

[16] T. Zykova-Timan, J. Horbach and K. Binder. *Monte carlo simulations of the solid–liquid transition in hard spheres and colloid–polymer mixtures.* J. Chem. Phys. **133**, 014705 (2010).

[17] R. K. Pathria. *Statistical Mechanics - 2nd Edition.* Butterworth-Heinemann (1996).

[18] X. G. Wen. *Statistical Physics II, MIT Course Number 8.08.* MIT OpenCourseWare Website (2005).

[19] C. N. Likos. *Colloidal Interactions: From Effective Potentials to Structure.* IOS Press (2013).

[20] J. -L. Barrat and J. -P. Hansen. *Basic Concepts for Simple and Complex Liquids.* Cambridge University Press (2003).

[21] L. S. Ornstein and F. Zernike. *Accidental deviations of density and opalescence at the critical point of a single substance.* Proc. Acad. Sci. Amsterdam **17**, 793 (1914).

[22] J. -P. Hansen and I. R. McDonald. *Theory of Simple Liquids with Applications to Soft Matter - 4th Edition.* Academic Press (2013).

[23] R. Evans. Density functional theory for inhomogeneous fluids i: Simple fluids in equilibrium. In M. Napiórkowski B. Cichocki and J. Piasecki, editors, *3rd Warsaw School of Statistical Physics.* Warsaw University Press (2009).

[24] A.Mulero (Ed.). *Theory and Simulation of Hard-Sphere Fluids and Related Systems.* Springer (2008).

[25] R. Evans. *Fundamentals of Inhomogeneous Fluids: Density functionals on the theory of nonuniform fluids, ed by D. Henderson.* Marcel Dekker New York (1992).

[26] H. Löwen. *Density functional theory of inhomogeneous classical fluids: recent developments and new perspectives.* J. Phys.: Condens. Matter **14**, 11897 (2002).

[27] J. K. Percus. *Equilibrium state of a classical fluid of hard rods in an external field.* J. Stat. Phys. **15**, 505 (1976).

[28] Y. Rosenfeld. *Free-energy model for the inhomogeneous hard-sphere fluid mixture and density-functional theory of freezing.* Phys. Rev. Lett. **63**, 980 (1989).

[29] T. K. Vanderlick, H. T. Davis and J. K. Percus. *The statistical mechanics of inhomogeneous hard rod mixtures.* J. Chem. Phys. **91**, 7136 (1989).

[30] P. Tarazona and R. Evans. *Long ranged correlations at a solid-fluid interface a signature of the approach to complete wetting.* Mol. Phys. **47**, 1033 (1982).

[31] J. S. Rowlinson and B. Widom. *Molecular Theory of Capillarity.* Dover New York (2003).

[32] A. A. Louis, P. G. Bolhuis, and J. P. Hansen. *Mean-eld uid behavior of the gaussian core model.* Phys. Rev. E **62**, 7961 (2000).

[33] P. Hopkins, A. Fortini, A. J. Archer and M. Schmidt. *The van hove distribution function for brownian hard spheres: Dynamical test particle theory and computer simulations for bulk dynamics.* J. Chem. Phys. **133**, 224505 (2010).

[34] S. L. Singh, A. S. Bharadwaj and Y. Singh. *Free-energy functional for freezing transitions: Hard-sphere systems freezing into crystalline and amorphous structures.* Phys. Rev. E **83**, 051506 (2011).

[35] M. Oettel, S. Dorosz, M. Berghoff, B. Nestler and T. Schilling. *Description of hard–sphere crystals and crystal–fluid interfaces: A comparison between density functional approaches and a phase–field crystal model.* Phys. Rev. E **86**, 021404 (2012).

[36] K. R. Elder and M. Grant. *Modeling elastic and plastic deformations in nonequilibrium processing using phase field crystals.* Phys. Rev. E **70**, 051605 (2004).

[37] J. Swift and P. C. Hohenberg. *Hydrodynamic fluctuations at the convective instability.* Phys. Rev. A **15**, 319 (1977).

[38] S. A. Brazovskiĭ. *Phase transition of an isotropic system to a nonuniform state.* Zh. Eksp. Teor. Fiz. **68**, 175 (1975).

[39] G. Gompper and S. Zschocke. *Ginzburg-landau theory of oil-water-surfactant mixtures.* Phys. Rev. A **46**, 4836 (1992).

[40] A. Jaatinen and T. Ala–Nissila. *Extended phase diagram of the three-dimensional phase field crystal model.* J. Phys.: Condens. Matter **22**, 205402 (2010).

[41] S. Nordholm, M. Johnson and B. C. Freasier. *Generalized van der waals theory. iii. the prediction of hard sphere structure.* Aust. J. Chem. **33**, 2139 (1980).

[42] O. Gunnarsson, M. Johnson and B.I. Lundqvist. *Descriptions of exchange and correlation effects in inhomogeneous electron systems.* Phys. Rev. B **20**, 3136 (1979).

[43] P. Tarazona. *A density functional theory of melting.* Mol. Phys. **52**(1), 81 (1984).

[44] Y. Rosenfeld. *Scaled field particle theory of the structure and the thermodynamics of isotropic hard particle fluids.* J. Chem. Phys. **89**, 4272 (1988).

[45] E. Kierlik and M. L. Rosinberg. *Free-energy density functional for the inhomogeneous hard-sphere fluid: Application to interfacial adsorption.* Phys. Rev. A **42**, 3382 (1990).

[46] R. Roth. *Fundamental measure theory for hard-sphere mixtures: a review.* J. Phys.: Condens. Matter **22**, 063102 (2010).

[47] P. Tarazona, U. Marini Bettolo Marconi and R. Evans. *Phase equilibria of fluid interfaces and confined fluids: Non-local versus local density functionals.* Mol. Phys. **60**, 573 (1987).

[48] P. Tarazona and Y. Rosenfeld. *From zero-dimension cavities to free-energy functionals for hard disks and hard spheres.* Phys. Rev. E **55**, R4873 (1997).

[49] Y. Rosenfeld, M. Schmidt, H. Löwen, and P. Tarazona. *Fundamental-measure free-energy density functional for hard spheres: Dimensional crossover and freezing.* Phys. Rev. E **55**, 4245–4263 (1997).

[50] P. Tarazona. *Density functional for hard sphere crystals: A fundamental measure approach.* Phys. Rev. Lett. **84**, 694 (2000).

[51] R. Roth, R. Evans, A. Lang and G. Kahl. *Fundamental measure theory for hard-sphere mixtures revisited: the white bear version.* J. Phys.: Condens. Matter **14**, 12063–12078 (2002).

[52] H. Hansen-Goos and R. Roth. *Density functional theory for hard-sphere mixtures: the white bear version mark ii.* J. Phys.: Condens. Matter **18**, 8413 (2006).

[53] P.-M. König, R. Roth, and K. R. Mecke. *Morphological thermodynamics of fluids: Shape dependence of free energies.* Phys. Rev. Lett. **63**, 160601 (2004).

[54] F. H. Stillinger, Z. W. Salsburg and R. L. Kornegay. *Rigid disks at high density.* J. Chem. Phys. **43**, 932 (1965).

[55] L. V. Woodcock. *Entropy difference between the face-centred cubic and hexagonal close-packed crystal structures.* Nature **385**, 141 (1997).

[56] U. Marini Bettolo Marconi and P. Tarazona. *Dynamic density functional theory of fluids.* J. Chem. Phys. **110**, 8032 (1999).

[57] U. Marini Bettolo Marconi and P. Tarazona. *Dynamic density functional theory of fluids.* J. Phys.:Condens. Matter **12**, A413 (2000).

[58] R. L. Davidchack and B. B. Laird. *Crystal structure and interaction dependence of the crystal-melt interfacial free energy.* Phys. Rev. Lett. **94**, 086102 (2005).

[59] E. J. Meijer and D. Frenkel. *Melting line of yukawa system by computer simulation.* J. Chem. Phys. **94**, 2269 (1991).

[60] V. Heinonen, A. Mijailovic, C. V. Achim, T. Ala-Nissila, R. E. Rozas, J. Horbach, and H. Löwen. *Bcc crystal-fluid interfacial free energy in yukawa systems.* J. Chem. Phys. **138**, 044705 (2013).

[61] W. G. Hoover, D. A. Young, and R. Grover. *Melting line of yukawa system by computer simulation.* J. Chem. Phys. **56**, 2207 (1972).

[62] F. H. Stillinger, Z. W. Salsburg, and R. L. Kornegay. *Rigid disks at high densities.* J. Chem. Phys. **43**, 932 (1965).

[63] Z. W. Salsburg, W. G. Rudd, and F. H. Stillinger. *Rigid disks at high densities. ii.* J. Chem. Phys. **47**, 4534 (1967).

[64] W. G. Rudd, Z. W. Salsburg, A. P. Yu, and F. H. Stillinger. *Rigid disks and spheres at high densities. iii.* J. Chem. Phys. **49**, 4857 (1968).

[65] A. D. Bruce, N. B. Wilding, and G. J. Ackland. *Free energy of crystalline solids: A lattice–switch monte carlo method.* Phys. Rev. Lett. **79**, 3002 (1997).

[66] M. Oettel, S. Görig, A. Härtel, H. Löwen, M. Radu, and T. Schilling. *Free energies, vacancy concentrations, and density distribution anisotropies in hard-sphere crystals: A combined density functional and simulation study.* Phys. Rev. E **82**, 051404 (2010).

[67] M. Oettel, S. Dorosz, M. Berghoff, B. Nestler, and T. Schilling. *Description of hard-sphere crystals and crystal-fluid interfaces: A comparison between density functional approaches and a phase-field crystal model.* Phys. Rev. E **86**, 021404 (2012).

[68] C. H. Bennett and B. J. Alder. *Studies in molecular dynamics. ix. vacancies in hard sphere crystals.* J. Chem. Phys. **54**, 4796 (1971).

[69] R. J. Buehler, R. H. Wentorf, J. O. Hirschfelder, and C. F. Curtiss. *The free volume for rigid sphere molecules.* J. Chem. Phys. **19**, 61 (1951).

[70] C. Vega and E. Noya. *Revisiting the frenkel-ladd method to compute the free energy of solids: The einstein molecule approach.* J. Chem. Phys. **127**, 154113 (2007).

[71] W. A. Curtin and K. Runge. *Weighted-density-functional and simulation studies of the bcc hard-sphere solid.* Phys. Rev. A **35**, 4755 (1987).

[72] J. F. Lutsko. *Properties of non-fcc hard-sphere solids predicted by density functional theory.* Phys. Rev. E **74**, 021121 (2006).

[73] S. Belli, M. Dijkstra, and R. van Roij. *Free minimization of the fundamental measure theory functional: Freezing of parallel hard squares and cubes.* J. Chem. Phys. **137**, 124506 (2012).

[74] H. Koch, C. Radin, and L. Sadun. *Most stable structure for hard spheres.* Phys. Rev. E **72**, 016708 (2005).

[75] L. V. Woodcock. *Entropy difference between the fcc and hcp crystal structures.* Nature **384**, 141 (1997).

[76] F. von der Lage and H. A. Bethe. *A method for obtaining electronic eigenfunctions and eigenvalues in solids with an application to sodium.* Phys. Rev. **71**, 612 (1947).

[77] F. Nizzoli. *Bragg reflections in hcp crystals.* J. Phys. C: Solid State Phys. **9**, 2977 (1976).

[78] F. H. Stillinger. *Lattice sums and their phase diagram implications for the classical lennard-jones model.* J. Chem. Phys. **115**, 5208 (2001).

[79] B. J. Alder, W. G. Hoover and D. A. Young. *Studies in molecular dynamics. v. high–density equation of state and entropy for hard disks and spheres.* J. Chem. Phys. **49**, 3688 (1968).

[80] D. A. Young and B. J. Alder. *Studies in molecular dynamics. xiii. singlet and pair distribution functions for hard–disk and hardsphere solids.* J. Chem. Phys. **60**, 1254 (1974).

[81] M. H. Yamani and M. Oettel. *Stable and metastable hard-sphere crystals in fundamental measure theory.* Phys. Rev. E **88**, 022301 (2013).

[82] A. Härtel, M. Oettel, R. E. Rozas, S. U. Egelhaaf, J. Horbach and H. Löwen. *Tension and stiffness of the hard sphere crystal-fluid interface.* Phys. Rev. Lett. **108**, 226101 (2012).

[83] R. L. Davidchack and B. B. Laird. *Simulation of the hard–sphere crystal–melt interface.* J. Chem. Phys. **108**, 9452 (1998).

[84] M. Amini and B. B. Laird. *Kinetic coefficient for hard–sphere crystal growth from the melt.* Phys. Rev. Lett. **97**, 216102 (2006).

[85] Y. Mu, A. Houk and X. Song. *Anisotropic interfacial free energies of the hard-sphere crystal–melt interface.* J. Phys. Chem. B **109**, 6500 (2005).

[86] R. L. Davidchack and B. B. Laird. *Direct calculation of the hard–sphere crystal/melt interfacial free energy.* Phys. Rev. Lett. **85**, 4751 (2000).

[87] R. L. Davidchack, J. R. Morris and B. B. Laird. *The anisotropic hard–sphere crystal–melt interfacial free energy from fluctuations.* J. Chem. Phys. **125**, 094710 (2006).

[88] R. L. Davidchack. *Hard spheres revisited: Accurate calculation of the solidliquid interfacial free energy.* J. Chem. Phys. **133**, 234701 (2010).

[89] H. J. Schöpe and P. Wette. *Seed– and wall–induced heterogeneous nucleation in charged colloidal model systems under microgravity.* Phys. Rev. E **83**, 051405 (2011).

[90] V. W. A. de Villeneuve, D. Verboekend, R. P. A. Dullens, D. G. A. L. Aarts, W. K. Kegel and H. N. W. Lekkerkerker. *Hard sphere crystal nucleation and growth near large spherical impurities.* J. Phys.: Condens. Matter **17**, S3371 (2005).

[91] A. Cacciuto, S. Auer and D. Frenkel. *Onset of heterogeneous crystal nucleation in colloidal suspensions.* Nature **428**, 404–406 (2004).

[92] S. Jungblut and C. Dellago. *Crystallization on prestructured seeds.* Phys. Rev. E **87**, 012305 (2013).

[93] J. P. Hoogenboom, P. Vergeer and A. van Blaaderen. *A real–space analysis of colloidal crystallization in a gravitational field at a flat bottom wall.* J. Chem. Phys. **119**, 3371 (2003).

[94] K. Sandomirski, E. Allahyarov, H. Löwen and S. U. Egelhaaf . *Heterogeneous crystallization of hard-sphere colloids near a wall.* Soft Matter **7**, 8050 (2011).

[95] M. Dijkstra. *Capillary freezing or complete wetting of hard spheres in a planar hard slit?* Phys. Rev. Lett. **93**, 108303 (2004).

[96] I. Volkov, M. Cieplak, J. Koplik and J. R. Banavar. *Molecular dynamics simulations of crystallization of hard spheres.* Phys. Rev. E **66**, 061401 (2002).

[97] A. Heymann, A. Stipp, C. Sinn and T. Palberg. *Observation of oriented close–packed lattice planes in polycrystalline hard–sphere solids.* J. Coll. Interface Science **207**, 119 (1998).

[98] L. Antl, J. W. Goodwin, R. D. Hill, R. H. Ottewill, S.M. Owens and S. Papworth. *The preparation of poly(methyl methacrylate) latices in non-aqueous media.* Colloids Surf. **17**, 67 (1986).

[99] A. van Blaaderen and A. Vrij. *Synthesis and characterization of colloidal dispersions of fluorescent, monodisperse silica spheres.* Langmuir **8**, 2921 (1992).

[100] A. Yethiraj and A. van Blaaderen. *A colloidal model system with an interaction tunable from hard sphere to soft and dipolar.* Nature **421**, 513 (2003).

[101] S. M. Ilett, A. Orrock, W. C. K. Poon and P. N. Pusey. *Phase behavior of a model colloid-polymer mixture.* Phys. Rev. E **51**(2), 1344 (1995).

[102] K. N. Pham, A. M. Puertas, J. Bergenholtz, S. U. Egelhaaf, A. Moussaïd, P. N. Pusey, A. B. Schofield, M. E. Cates, M. Fuchs, and W. C. K. Poon. *Multiple glassy states in a simple model system.* Science **296**, 104 (2002).

[103] U. Gasser, E. R. Weeks, Andrew Schofield, P. N. Pusey and D. A. Weitz. *Real-space imaging of nucleation and growth in colloidal crystallization.* Science **292**, 258 (2001).

[104] R. P. A. Dullens, D. G. A. L. Aarts, and W. K. Kegel. *Dynamic broadening of the crystal-fluid interface of colloidal hard spheres.* Phys. Rev. Lett **97**, 228301 (2006).

[105] S. Egelhaaf. private communication (December 2010).

[106] J. Hernández-Guzmán and E. R. Weeks. *The equilibrium intrinsic crystal–liquid interface of colloids.* PNAS **106**, 15198 (2009).

[107] W. Lechner, C. Dellago and P. G. Bolhuis. *Role of the prestructured surface cloud in crystal nucleation.* Phys. Rev. Lett. **106**, 085701 (2011).

[108] D. J. Courtemanche and F. van Swol. *Wetting state of a crystal-fluid system of hard spheres.* Phys. Rev. Lett. **69**, 2078 (1992).

[109] D. J. Courtemanche and F. van Swol. *A molecular dynamics study of prefreezing hard spheres at a smooth hard wall.* Mol. Phys. **80**, 861 (1993).

[110] M. Schmidt and H. Löwen. *Freezing between two and three dimensions.* Phys. Rev. Lett. **76**, 4552 (1966).

[111] M. Schmidt and H. Löwen. *Phase diagram of hard spheres confined between two parallel plates.* Phys. Rev. E **55**, 7228 (1997).

[112] M. Heni and H. Löwen. *Interfacial free energy of hard-sphere fluids and solids near a hard wall.* Phys. Rev. E **60**, 7057 (1999).

[113] R. Zangi and S. A. Rice. *Nature of the transition from two- to three-dimensional ordering in a confined colloidal suspension.* Phys. Rev. E **61**, 660 (2000).

[114] W. K. Kegel. *Freezing of hard spheres in confinement.* J. Chem. Phys. **115**, 6538 (2001).

[115] R. Messina and H. Löwen. *Reentrant transitions in colloidal or dusty plasma bilayers.* Phys. Rev. Lett. **91**, 146101 (2003).

[116] S. Auer and D. Frenkel. *Line tension controls wall–induced crystal nucleation in hard–sphere colloids.* Phys. Rev. Lett. **91**, 015703 (2003).

[117] A. Fortini and M. Dijkstra. *Phase behaviour of hard spheres confined between parallel hard plates: manipulation of colloidal crystal structures by confinement.* J. Phys.: Condens. Matter **18**, L371 (2006).

[118] E. De Miguel and G. Jackson. *Detailed examination of the calculation of the pressure in simulations of systems with discontinuous interactions from the mechanical and thermodynamic perspectives.* Mol. Phys. **104**, 3717 (2006).

[119] B. B. Laird and R. L. Davidchack. *Wall–induced prefreezing in hard spheres: a thermodynamic perspective.* J. Phys. Chem. C **111**, 15952 (2007).

[120] B. B. Laird and R. L. Davidchack. *Calculation of the interfacial free energy of a fluid at a static wall by gibbs–cahn integration.* J. Chem. Phys. **132**, 204101 (2010).

[121] D. H. Napper. *Polymeric stabilization of colloidal dispersions.* Academic Press London (1984).

[122] In B. Vincent E. D. Goddard, editor, *Polymer Adsorption and Dispersion Stability.* American Chemical Society Washington (1984).

[123] D. Deb, A. Winkler, M. H. Yamani, M. Oettel, P. Virnau and K. Binder. *Hard sphere fluids at a soft repulsive wall: A comparative study using monte carlo and density functional methods.* J. Chem. Phys. **134**, 214706 (2011).

[124] J. D. Weeks, D. Chandler and H. C. Andersen. *Role of repulsive forces in determining the equilibrium structure of simple liquids.* J. Chem. Phys. **54**, 5237 (1971).

[125] N. F. Carnahan and K. E. Starling. *Equation of state for nonattracting rigid spheres.* J. Chem. Phys. **51**, 635 (1969).

[126] T. Boublík. *Hardsphere equation of state.* J. Chem. Phys. **53**, 471 (1970).

[127] D. P. Landau and K. Binder. *A Guide to Monte Carlo Simulation in Statistical Physics, 3rd ed.* Cambridge University Press Cambridge (2009).

[128] T. M. Truskett, S. Torquato, S. Sastry, P. G. Debenedetti and F. H. Stillinger. *Structural precursor to freezing in the hard-disk and hard-sphere systems.* Phys. Rev. E **58**, 3083 (1998).

[129] W. A. Curtin. *Density–functional theory of the solid–liquid interface.* Phys. Rev. Lett. **59**, 1228 (1987).

[130] W. A. Curtin. *Density–functional theory of crystal–melt interfaces.* Phys. Rev. B page 6775 (1989).

[131] D. W. Marr and A. P. Gast. *Planar density–functional approach to the solid–fluid interface of simple liquids.* Phys. Rev. E **47**, 1212 (1993).

[132] A. D. J. Haymet and David W. Oxtoby. *A molecular theory for the solid–liquid interface.* J. Chem. Phys. **74**, 2559 (1981).

[133] David W. Oxtoby and A. D. J. Haymet. *A molecular theory of the solid–liquid interface. ii. study of bcc crystal–melt interfaces.* J. Chem. Phys. **76**, 6262 (1982).

[134] Wikipedia contributors. Explicit and implicit methods . URL http://en.wikipedia.org/w/index.php?title=Explicit_and_implicit_methods&oldid=603271183.

[135] J. T. Chayes, L. Chayes and E. H. Lieb. *The inverse problem in classical statistical mechanics.* Commun. Math. Phys. **93**(1), 57 (1984).

[136] J. T. Chayes and L. Chayes. *On the validity of the inverse conjecture in classical density functional theory.* J. Stat. Phys. **36**, 471 (1984).

[137] A. Kovalenko, S. Ten-No and F. Hirata. *Solution of three-dimensional refrence interaction site model and hypernetted chain equation for simple point charge water by modified diis.* J. Comput. Chem **20**, 928 (1999).

[138] M. Frigo and S. G. Johnson. *Fftw: an adaptive software architecture for the fft.* Proc. IEEE **3**, 1381 (1998).

[139] M. Frigo and S. G. Johnson. *The design and implementation of fftw3.* Proc. IEEE **93**, 216 (2005).

[140] H. Jeffreys and B. S. Jeffreys. *Methods of Mathematical Physics, 3rd ed.* Cambridge University Press Cambridge, England (1988).

[141] L. Collatz. *Functional analysis and numerical mathematics.* Academic Press New York (1966).

[142] P. Pulay. *Convergence acceleration of iterative sequences. the case of scf iteration.* Chem. Phys. Lett. **73**, 393 (1980).

[143] P. Pulay. *Improved scf convergence acceleration.* J. Comput. Chem. **3**, 556 (1982).

[144] E. W. Weisstein. *Euler Forward Method.* From MathWorld–A Wolfram Web Resource.

[145] R. Courant, K. Friedrichs and H. Lewy. *On the partial difference equations of mathematical physics.* IBM J. **11**, 215 (1967).

[146] W. H. Press, B. P. Flannery, S. A. Teukolsky and W. T. Vetterling. *Numerical Recipes in FORTRAN: The Art of Scientific Computing, 2nd ed.* Cambridge University Press Cambridge, England (1992).

[147] A. Kovalenko, S. Ten-no and F. Hirata. *Solution of three-dimensional reference interaction site model and hypernetted chain equations for simple point charge water by modified method of direct inversion in iterative subspace.* J. Comput. Chem. **20**, 928 (1999).

[148] J. Reinhardt. Stiffness and iteration methods for dft and ddft calculations. Technical report (July).

[149] Å .Björck. *Numerical Methods in Scientic Computing, Volume II.* siam (2009).